COLLIDING LASER PRODUCED PLASMA PHYSICS AND APPLICATIONS IN INERTIAL FUSION AND NANOLITHOGRAPHY

by

John P. Oliver

A Dissertation

Submitted to the Faculty of Purdue University

In Partial Fulfillment of the Requirements for the degree of

Doctor of Philosophy

School of Nuclear Engineering

West Lafayette, Indiana

December 2018

THE PURDUE UNIVERSITY GRADUATE SCHOOL

STATEMENT OF COMMITTEE APPROVAL

Dr. Tatyana S. Sizyuk, Chair
Department of Nuclear Engineering
Dr. Ahmed Hassanein
Department of Nuclear Engineering
Dr. Tomas J. Diaz de la Rubia
Department of Materials Engineering
Dr. Zinetula Z. Insepov
Moscow Engineering Physics Institute
Dr. Valeryi A. Sizyuk
Department of Nuclear Engineering

Approved by:

Dr. Shripad Revankar
Head of the Graduate Program

This Dissertation is dedicated to
my father who inspired my passion and curiosity for science,
my mother who supported me with love throughout this endeavor, and
my advisor, Tatyana, whose erudition and patience were essential to my success.

ACKNOWLEDGEMENTS

I would like to thank my advising professors, Dr. Tatyana Sizyuk for providing the experimental and intellectual tools essential for conducting impactful research. I would further extend my appreciation to the Committee members, Dr. Ahmed Hassanein, Dr. Tomas J. Diaz de la Rubia, Dr. Zinetula Z. Insepov, and Dr. Valeryi Sizyuk for helpful comments and advice. I would also like to appreciate my research colleagues at CMUXE whose support and assistance helped foster my success. Lastly, I would like to express gratitude to the College of Engineering (for bestowing the Ross Fellowship) and to the National Science Foundation's Partnerships for International Research and Education (PIRE) project for supporting my graduate research and education.

TABLE OF CONTENTS

LIST OF TABLES

LIST OF FIGURES

ABSTRACT

Author: Oliver, John P. PhD
Institution: Purdue University
Degree Received: December 2018
Title: Colliding Laser Produced Plasma Physics and Applications in Inertial Fusion and Nanolithography
Major Professor: Tatyana Sizyuk

Laser-produced plasmas (LPP) have been used in a wide range of applications such as in pulsed laser deposition (PLD), extreme ultraviolet lithography (EUVL), laser-induced breakdown spectroscopy (LIBS), and many more. In the collision of two laser-produced plasmas, the two counter-streaming plasmas may face a degree of stagnation which influences the subsequent development of the compound plasma plume. The plume development of the stagnation layer can deviate quite noticeably from typical laser-plasma behavior. For instance, an enhanced degree of collisionality is expected, especially when the plasma collision transpires in a low pressure ambient. Colliding plasma can be intentionally implemented or conversely may occur naturally. In EUV lithography colliding plasma could service as an efficient EUV source with inherent debris mitigation. Conversely, colliding plasma could manifest in an inertial fusion energy (IFE) chamber leading to contamination, disrupting successful device operation.

Various techniques such as optical emission spectroscopy (OES), CCD plume imaging, laser-induced fluorescence (LIF), laser-induced incandescence (LII), and scanning electron microscopy (SEM) may be used to study laser-produced plasmas and their associated byproducts. These techniques will be used extensively throughout this work to aid in developing an understanding of the various physical and chemical phenomena occurring in these plasmas.

Chapter 1 provides introductory knowledge regarding LPPs with a specific exploration into colliding plasma and its relevance to a broad body of scientific knowledge. Additionally, the principles behind the various experimental techniques are capitulated.

Chapter 2 presents the laboratory facilities available at our Center for Materials Under eXtreme Environment (CMUXE) which can be used to study LPP. The various equipment (chambers, lasers, spectrograph, etc.) are discussed in detail.

Chapter 3 begins the series of substantive chapters which comprise the original research of this thesis. Here, the early formation (< 1 μs) of colliding carbon plasmas produced from the ablation of graphite is explored. The influence of plume hydrodynamics on the temporary lateral confinement of the stagnation layer is discussed with attention to the three different laser intensities studied. Additionally, species in the plasma were identified using OES and monochromatic plume imaging. A large increase in Swan emission from C_2 dimers is observed in the stagnation layer, suggesting formation of C_2 and/or re-excitation of C_2 produced ab initio during laser ablation. Results were compared with HEIGHTS computational modeling to verify observations and to validate the code package for a new plasma regime.

Chapter 4 functions as a continuation from Chapter 3, looking into the intermediate time (1-10 μs) dynamics of colliding carbon plasma. To observe transient molecular species of carbon, C_2 and C_3, LIF was employed. By acquiring plume images through LIF, the various mechanisms by which C_2 and C_3 appear at different times in the plasma lifetime may be discerned. Using optical time-of-flight (OTOF), more information of carbon species populations may be determined to construct space-time contours which offer corroborative information regarding the spatiotemporal development of the stagnation layer.

Chapter 5 presents work on colliding Sn plasma for application as a EUV light source. The accumulation of material along the stagnation layer makes colliding plasmas a suitable preplasma in a dual pulse laser scheme. Dual-pulse EUV concepts call for the formation of a preplasma from the stagnation of two Sn plasmas. This preformed plasma is then subject to a second, pumping laser purposed to optimize the conversion efficiency (CE) of laser energy into EUV output. Characterization of the stagnation layer was obtained through optical emission spectroscopy while CE data is obtained using an absolutely calibrated EUV photodiode. HEIGHTS computational modeling then provides prediction of EUV emission upon using a CO_2 laser for preplasma reheat

Chapter 6 explores the collision between two dissimilar plasmas. Laser-produced plasma of Si and C are created in a manner which enables the two plasmas to collide. The ensuing development of the colliding plasma regime is then discussed in terms of relevant plume hydrodynamics. Analysis of the colliding regime is accomplished using fast-gated plume imaging and optical time-of-flight.

The final chapter, Chapter 7, provides a concise summary of the results presented in the preceding chapters. Additionally, recommended research directives are presented which are designed with consideration for the current facilities and capabilities at CMUXE.

1. INTRODUCTION

1.1 Pulsed Laser Technology

With the advent of laser technology in the 1960, a new field of physics arose in optics. In its early years, the laser was commonly thought of as a technological solution looking for a problem, but its utility would soon become apparent. The word "laser" was initially an acronym for "light amplification by stimulated emission of radiation" but has since lost status as an acronym in the current lexicon. The name arises from the manner by which a laser optical cavity (oscillator) generates an intense beam of monochromatic light.

In a laser cavity, light circulates (e.g. between two mirrors), making multiple passes through a gain medium. The gain medium is pumped (e.g. via flash lamps or another laser) such that a higher population of atoms exist in an excited, high-energy state than in the ground state. This is known as a population inversion. Stimulated emission occurs when an incident photon interacting with the excited atom is prompted to descend to a lower energy state, emitting a photon with a prescribed energy determined from the discrete orbital transition. Light amplification of the beam occurs during multiple passes through the gain medium, generating a monochromatic beam from stimulated emission.

The unique character of a laser light arises from its monochromatic nature. The narrow optical bandwidth gives rise to excellent spatial and temporal coherence of the beam. This allows the beam to propagate through space with minimal divergence and to be focused to incredibly small spots. Moreover, the output beam from the laser cavity usually bears small etendue, and thus the emitted laser pulse is capable delivering intense electromagnetic energy pulses across relatively large distances. The monochromatic nature of laser light also suppresses

group dispersion of the pulse which enables laser pulses to retain their short pulse duration while passing through multiple optics.

Different technologies may be additionally implemented to alter the character of the output laser pulse. Using harmonic crystals, the wavelength of the output pulse can be halved, quartered, etc. (e.g. an Nd:YAG laser emitting at 1064 nm at its fundamental mode may emit at 532 nm or 264 nm alternatively using harmonic crystals). An optical parametric oscillator (OPO) may be used to produce a wide tunable range of output wavelengths using a nonlinear crystal by procuring two phase-matched signal and idler beams from an inputted pump beam.

In the course of the research conducted in this dissertation, certain laser parameters recur throughout. The pulse energy of the laser corresponds to the total energy possessed by the photons released during one optical pulse of the laser. The temporal intensity signal of the laser pulse can adequately be characterized by a Gaussian profile. The time spanning the full width at half maximum (FWHM) of the pulse is known as the pulse width. The two-dimensional spatial profile of the laser pulse may be also be characterized as Gaussian. Here, the FWHM is referred to as the spot diameter or spot size. With these parameters known, a simple calculation can be made to determine the laser intensity. Before commencing discussion of laser-plasma, let's entreat a more generalized overview of plasma, the fourth state of matter.

1.2 Plasma Fundamentals

Plasma is known to be the fourth fundamental state of matter. Precisely, plasma is the state of matter attributed to an ionized gas which possesses high conductivity due the enhanced mobility of electrons throughout the gaseous system. Partial ionization of the gas must be achieved in order for this to be accomplished which is typically done through heating the plasma

to temperatures approaching the first ionization energy of the valence electron. Typically, plasma is created by some means of externally imposing an intense electric field. This could be an electric discharge or (for particular interest to this work) by means of optical breakdown using a laser.

Plasma has the kinematic behavior of a gas. However, plasmas exhibit metal-like behavior due to their having a plethora of free electrons available to flow unimpeded within the plasma. For this reason, plasmas are susceptible to long-range interactions with externally applied electric and magnetic fields. A few of the most important properties and characteristics of plasma are presented below.

1.2.1 Temperature

Since plasma is created by heating a gas to the point of ionization, it should be pretty straight-forward that the plasma temperature is an important property which establishes the degree of ionization of the plasma. In academic discourse of plasmas, it is often the case that the temperature of the plasma is given in units of electron-volts [eV]. This offers a convenient means to discuss important quantities (e.g. ionization energy and emitted photon energy) with relation to the plasma temperature.

Plasma may be divided into an ion subsystem and an electron subsystem. What this implies is that the energy distributions for ions and electrons may differ. This is particularly appropriate during highly transient moments of plasma development (e.g. laser-plasma interaction) during which time electrons and ions haven't equilibrated. For the ensuing discussion in this work, electron temperature and plasma temperature are used rather

interchangeably, and it is further assumed that the electron and ion subsystems are in equilibrium unless otherwise stated.

1.2.2 Density

As was discussed with plasma temperature, the density of plasma may be divided into subsystems. The density of varies species (i.e. ions, neutrals, molecules) refers to the number density of such species within the plasma. In such cases, the word density will be preceded by the particular species being ascribed. However, when we mention density, we are most often referring to the density of electrons. The electron density is related to the ion density by multiplying it by the effective (average) charge of the plasma:

$$n_e = \langle Z \rangle n_i = \sum_{j=0}^{Z_{atomic}} j * n_j$$

1.2.3 Degree of Ionization and Saha Equation

While the first ionization of most elements is in excess of 5 eV, it is not necessary for plasmas to reach this temperature to possess singly-ionized species. The degree of ionization follows an Arrhenius type relationship, so a small portion of the plasma will be ionized even while bulk plasma is much below the ionization threshold energy. Precisely, the degree of ionization is the ratio between number densities of ion species and that of the overall density of the plasma:

$$\alpha = \frac{n_{ion}}{\sum_j n_j}$$

Plasmas are usually described as either *weakly* or *fully* ionized loosely predicated upon their respective degree of ionization. This distinction may be made in a more technical manner by comparing the collision frequencies of ions and neutrals with electrons. Generally, the electron-ion collision is more prevalent than the electron-neutral collision, so even at a low degree of ionization, the electron-ion collision frequency (ν_{ei}) exceeds the electron-neutral collision frequency (ν_{en}). A plasma transitions from weakly ionized to fully ionized upon satisfying $\nu_{ei} > \nu_{en}$ at which point the plasma enters a regime dominated by Coulomb collisions [1]. Such "fully ionized" plasmas may still feature a low degree of ionization, bearing temperatures below the first ionization energy.

Assuming that a low-temperature, weakly ionized plasma follows a Maxwell-Boltzmann distribution, it is possible to predict the degree of ionization of the plasma given certain parameters. The Saha equation describes this by balancing collision-induced ionization with recombination while also accounting for quantum mechanical aspects:

$$\frac{n_{i+1}n_e}{n_i} = \frac{2}{\lambda_{th}^3}\frac{g_{i+1}}{g_i}\exp\left[-\frac{\epsilon_{i+1}-\epsilon_i}{k_B T}\right] \qquad \lambda_{th} \equiv \sqrt{\frac{2\pi\hbar^2}{m_e k_B T}}$$

where n_i is the density of the i-th ionization stage, g is the degeneracy of states, ϵ is the ionization energy, n_e is the electron density, λ_{th} is the thermal de Broglie wavelength of an electron, m_e is the electron mass, T is the gas temperature, k_B is the Boltzmann constant, and $\hbar$ is the reduced Planck's constant [2].

1.2.4 Quasineutrality

While plasmas feature a degree of ionization, the macroscopic plasma collectively remains electrically neutral. On the atomic level, electrons stream amongst the more slowly

moving ion and neutral species. Being unbound, they may attempt to leave the boundary of the ionic plasma. In so doing, they manifest a charge separation from the ions, producing a restoring electric field. The electrons are promptly pulled back to the plasma. This process repeats, and the electron population develops harmonic oscillations about the kinetically inert ion population. The high frequency of these plasma oscillations amounts to a global charge neutrality of the plasma on a time-averaged basis. Locally, however, the plasma is a collection of positive and negative point charges on a scale where electrical neutrality is not observed. *Quasineutrality* is the term used to describe this paradoxical behavior. The plasma is neutral but only as observed on the macroscopic scale.

1.2.5 Plasma Frequency and Critical Density

It was briefly stated that plasma experiences a characteristic oscillation of the electron subsystem following a perturbation. This oscillation occurs at what is known as the *plasma frequency* (specifically electron plasma frequency), ω_p:

$$\omega_p = \sqrt{\frac{n_e q_e^2}{\varepsilon_0 m_e}}$$

where n_e is the electron density, q_e is the electron charge, ε_0 is the free-space permittivity, and m_e is the electron mass, respectively. These oscillations are damped by thermal collisions but may be sustained if the plasma is continually perturbed by an external driver. A quantum of plasma oscillation is sometimes referred as a *plasmon*. This is analogous to how a *phonon* is a quantization of mechanical vibrations.

An interesting phenomenon happens when light with optical frequency below the plasma frequency impinges the oscillating electron subsystem [plasma]. Light with frequency below this cutoff value undergoes total reflection, unable to penetrate farther into the overdense plasma.

1.2.6 Debye Shielding

When an electric field is present in plasma, charge carriers within the plasma tend to arrange themselves in a manner which achieves electrical neutrality. This is analogous to how a metal responds when subjected to an external electric field. Free electrons within the lattice quickly redistribute to nullify any internal electric field from being established. For this reason, metals are incapable of sustaining electric fields on the macroscopic scale. Identically, free electrons in plasma automatically distribute in a manner which shields internal electric fields.

To properly appreciate this property of plasma, we should investigate how a charge embedded within the plasma invokes an electrostatic field. Normally a test charge in free space will have an electric potential described as

$$\phi(r) = \frac{1}{4\pi\epsilon_0}\frac{Q}{r}$$

However, in close proximity to the positive test charge, electron and ion densities of the plasma will not be equal. Electrons will be pulled inward whereas other ions will be repulsed farther away. It becomes appropriate to determine a more suitable electrical potential by evoking Poisson's equation:

$$\nabla^2\phi(r) = -\frac{\rho}{\epsilon_0} = -\frac{q_e(n_e - n_i)}{\epsilon_0}$$

Equipped with knowledge of the non-uniform equilibrium distribution of electrons around an electric potential,

$$n_e(r) = n_{e,0} e^{-\frac{q_e \phi(r)}{k_b T_e}},$$

The Poisson equation may be solved to determine the potential function. This is solved relative ease if we assume $|q_e\phi| << k_B T$ and perform a simple power series, only retaining the first two terms. We obtain the following equation form

$$\frac{1}{r^2}\frac{d}{dr}\left(r^2 \frac{d\phi}{dr}\right) \cong \left[\frac{n_{e,0} q_e^2}{\epsilon_0 k_B T_e}\right] \phi(r) = \frac{1}{\lambda_D^2}\phi(r)$$

where λ_D is known as the *Debye length*:

$$\lambda_D = \sqrt{\frac{\epsilon_0 k_B T_e}{n_{e,0} q_e^2}} = \frac{1}{\omega_p}\sqrt{\frac{k_B T_e}{m_e}}$$

The Debye length is essentially an intrinsic parameter to a specific plasma which describes the degree of self-shielding across a particular scale length. For most laboratory plasmas, the Debye length is on the order of micrometers though this length could be much larger in low electron density plasmas such as in the ionosphere. We can deduce from the equation that the Debye length shortens as electron density increases. This is quite intuitive since we can imagine that a greater number of free charge carriers would assist in accommodating field neutralization as more electrons become available to populate the shield cloud. Conversely, an increase in electron temperature lengthens the Debye length parameter. Electrons with greater kinetic energy more readily overcome Coulomb interactions and therefore are less responsive to an imposed electric field. Sometimes, the term *Debye sphere* may be used which is simply a volumetric sphere with radius equal to the Debye length. The test charge potential after correcting for Debye shielding is as follows

$$\phi(r) = \left[\frac{1}{4\pi\epsilon_0}\frac{Q}{r}\right] e^{-\frac{r}{\lambda_D}}$$

In discussion, the Debye length of a plasma is often used to determine the scale for which quasineutrality may be assumed appropriate. When describing a plasma on the scale of several millimeters, it is usually acceptable to neglect long-range electrostatic forces. However, when discussing physics occurring on a scale smaller than the Debye length, the quasineutrality assumption is invalid and we must incorporate local electric field effects to properly describe the plasma in full.

1.3 Laser-plasma Fundamentals

1.3.1 Laser-matter Interaction and Nascent Plasma

The interaction of a laser pulse is governed by the multitude of mechanisms by which high intensity electromagnetic radiation may interact with the material interface. Commonly, lasers emit in the near-infrared region (e.g. Nd:YAG at 1064 nm) or deeply from within the infrared (TEA CO_2 at 10.6 μm). Light of these wavelengths bear insufficient energy on a per-photon basis to effectively cause direct photoionization. Rather, laser energy is imparted to the electrons via inverse bremsstrahlung absorption whereupon bound electrons in the lattice may populate the conduction band. The principle mechanisms by which ionized plasma is created include electron impact, multiphoton, and field ionization. Electron-atom and electron-ion impact ionization processes are prevalent in ablation schemes with sub-terawatt EM field intensities (such is typically the case when using nanosecond pulse lasers). In these processes, a bound electron is liberated through the collision of the atom with a free electron possessing energy exceeding the ionization potential. The result is two freed electrons with a loss of

thermodynamic free energy. The collisional process can be described by the following equation (where α is the absorption coefficient per single electron):

$$\frac{dE_e}{dt} = n\sigma\left(\frac{8}{\pi}\frac{k_B T_e}{m}\right)^{\frac{1}{2}}\frac{e^2}{m\varepsilon_0 c\omega^2}I = \alpha I$$

As the mean electron energy increases, it follows that excitation and ionization cross sections also grow. An avalanche ensues if energy losses (i.e. via hot electron diffusion, ion and atom excitation, radiation losses, recombination, and electron gas expansion) don't exceed electron energy gains from impact ionization. This holds until a significant electron density has formed.

In laser ablation, electrons are first to absorb electromagnetic radiation via inverse bremsstrahlung. Hot electrons promptly escape from the bulk, within picoseconds establishing a static electric field from the resultant charge separation. As further electrons attempt to escape, they are withheld by space-charge limitation. A buildup of electron density ensues at the near-surface. At some point, the electron density reaches the so-called critical density at which point incident light below a cutoff frequency reflects from the plasma (more on critical density later). It follows, then, that the deposition location of laser energy shifts outward from the surface as the electron density increases over time and the plasma expands.

1.3.2 Laser-plasma Interaction

An important property of nanosecond pulse lasers is the phenomena of laser-plasma interaction. For high intensity laser irradiation, the laser-plasma has already established a nascent form, having evaporated target material from the surface during the laser pulse duration. Due to the plasma having reached the so-called plasma critical density or cutoff density, laser

light is reflected along this boundary. The target is shielded from further direct laser irradiation with the majority of laser energy being imparted to the peripheral region of the nascent plasma. Energy from the plasma region is reradiated to the target surface causing continued erosion. Following the termination of the laser pulse, cold, dense plasma (relatively speaking) remains above the target surface.

1.4 Colliding Plasma

1.4.1 Theory

A recurring topic in this dissertation is that of colliding plasma. Colliding plasma can be expressed as the plasma regime that manifests at the collision of expansion fronts from two counter-propagating laser-produced plasmas. Simply put, it is the resultant plasma formed from two individual plasmas which collide. To generate colliding plasma, two distinct "seed" plasmas are simultaneously created at stand-off locations by standard laser ablation and then meet along the mutually formed collision midplane. The plume dynamics of colliding plasmas have been studied [3][4][5][6]. Depending on various parameters, the two plasmas may either (i) interpenetrate (barely experiencing each other as they pass through) or (ii) stagnate (forming a composite plasma with a large degree of intermixing). Interpenetration is sometimes referred to as soft stagnation whereas "stagnation" (as is used more ubiquitously in later chapters) is conversely coined hard stagnation. In this work, greater interest will be placed on plasmas which exhibit (hard) stagnation.

The degree of stagnation intrinsic to a particular colliding plasma is primarily determined from two key parameters. The first parameter is a characteristic length, L, particular to the setup

geometry. This is standardly the distance between where the two seed plasmas form. The second parameter is the ion-ion mean free path, λ_{ii}, or, more precisely, the ion-ion mean free path associated to an ion injected at the ion sound speed [7]. While L is easily ascribed, understanding λ_{ii} and how it varies with situation is more complicated. λ_{ii} is given by

$$\lambda_{ii} = \frac{4\pi\varepsilon_0^2 m_i^2 v_{12}^4}{e^4 z^4 N_i ln\Lambda_{12}}$$

where ε_0 is the free space permittivity, m_i is the ion mass, v_{12} is the relative velocity of the ions, e is the electric charge, z is the average charge state of the plasma, N_i is the ion density, and $ln\Lambda_{12}$ is the Coulomb logarithm. It can be seen that the relative velocity and charge state strongly determine λ_{ii} thus seed plume energetics and composition play a significant role. The collisionality parameter is defined as the ratio of these two parameters:

$$\zeta = \frac{L}{\lambda_{ii}}$$

In essence, ζ is the inverse of the dimensionless Knudsen number. Low values of ζ indicate interpenetration while large ζ is indicative of stagnation. It should be intuitively evident why ζ is known as the collisionality parameter. For an ion transiting a plasma of some arbitrary thickness, the number of mean free paths it must travel scales directly with ζ (and therefore number of collisions it experiences). In high ζ colliding plasmas, ion kinetic energy is efficiently converted into thermal energy through high local collisionality. The stagnation layer attains local thermodynamic equilibrium conditions while sustaining plasma temperatures on the order of 1000s to 10,000s in Kelvin. The persistence of a colliding plasma is on the order a microsecond or longer, a relatively long timeframe for typical laser-produced plasmas.

While colliding plasma is instigated by the collision of two distinct laser-produced plasmas (LPP), the plume growth and development can be notably different from the growth of

one individual plume. The development of a LPP is characterized initially by isothermal heating followed by adiabatic expansion upon the termination of the laser pulse (when under vacuum). In a colliding plasma regime, this occurs for the seed plasmas before they meet and form stagnant plasma.

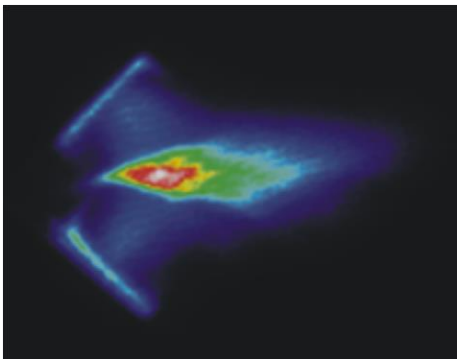

Figure 1.1 Representation of colliding plasma forming a 90° wedge.

It is understood that laser-produced plasmas expand principally in the direction of the target normal. This is true even when the laser enters at some off-normal incidence angle. The expansion peaks along the target normal but is also accompanied by slower expansion in radial transverse directions. By positioning two material surfaces at an angle (a wedge), laser-produced plasmas formed on each surface may be permitted to expand into one another. Depending on the wedge angle, some subtended portion of the peak plume velocity will be directly counter-streaming through a similar component of the mirror plasma birthed from the opposing surface. At this point, the characteristic length L is a minimum. All along the collision mid-plane, plasma collision will occur with varying degrees of stagnation depending on local values of previously discussed variables. Therefore, collisionality may be expressed using a distribution function in space and should be understood as a local, not global, value in time. When the wedge angle θ takes on unique values, we may prescribe a different coinage for the geometry. When $\theta = 180°$,

the setup is said to be planar. When $\theta = 0°$ (and the two plates are separated some distance), the setup is said to have a parallel plate configuration.

The stagnation region formed from colliding plasmas is naturally predisposed to high collisionality, but single laser-ablation plumes can exhibit high collisionality as well. This is most notably true when they form in an ambient environment [8]. The ambient fluid provides the necessary confinement to retard the leading edge of the plume. Turbulent mixing along the plume front creates a region of high collisionality. This effect can be observed at ambient pressures as low as 1 Torr. Increasing pressure has the additive effect of even greater confinement of the plume, increasing the number density of the plasma interior and therefore the number of collisions.

1.4.2 Applications of Colliding Plasma Research

1.4.2.1 Laboratory-scale Astrophysics

Colliding plasmas occur across many domains of nature. In space, the most abundant state of matter is plasma since it is to be expected that colliding plasmas frequently occur. Laboratory-scale astrophysics offers an experimental means to recreate some of these physical processes in a controlled setting with a host of diagnostic tools and equipment to advance further understanding. In astrophysics, colliding plasma regimes arise in the collision of interstellar objects such as with stars and in the formation of supernovae (SNe). Some experiments using colliding plasmas entail experimentally investigating the physics of collisionless magnetized shocks produced at the interface of a supernova remnant (SNR) and the interstellar medium (ISM) [9]. Additionally, colliding plasmas have been proposed for lab-scale nuclear astrophysics

studies to predict nuclear reaction rates while accounting for electron screening [10]. Developing a further understanding of colliding plasmas would also improve astrophysics models. An example of this is identifying low pressure transitions where the Rayleigh-Taylor (RT) instability develops [11]. The controlled recreation of these conditions is the principal objective in laboratory-scale astrophysics. Collisions of laser-produced plasmas have been used to accomplish this aim.

1.4.2.2 Inertial Fusion

In the field of controlled inertial confinement fusion (ICF), colliding plasma regimes naturally present in indirect drive ignition methods. In indirect drive, an array of high-energy drive lasers irradiates the interior wall of a gold cavity. Shaped as an annular cylinder, this so-called *hohlraum* encompasses a small fuel pellet composed of a frozen DT center encapsulated by a plastic ablator [12][13]. Laser energy impinging the hohlraum interior is designedly converted into x-rays which ablate the plastic exterior of the pellet. As the carbonaceous material violently explodes radially outward, the DT pellet undergoes super-compression via a "rocket effect" in accordance with Newton's third law of motion. The DT fuel density jumps three orders of magnitude, promptly instigating fusion of deuterium and tritium. The result is a brief small-scale thermonuclear detonation which releases tremendous energy while simultaneously vaporizing all remaining pellet and hohlraum material.

In the early stages of indirect drive, Au plasma is produced during the ablation of the hohlraum interior by the drive lasers. X-rays produced in this process subsequently cause ablation of plastic ablator with plasma blowoff erupting outwards to meet the Au plasma. The natural consequence is counter-streaming plasmas which could affect laser-plasma coupling

inside the hohlraum. Such scattering instabilities as stimulated Brillouin (SBS) and filamentation may arise, making fusion ignition even more difficult to attain [7].

ICF is a means to achieve inertial fusion energy (IFE) for the commercial generation of on-demand energy. IFE systems still require significant research and development overhaul before they become commercially viable, but such design concepts as LIFE (Laser Inertial Fusion Energy), HYLIFE-II [14], SOMBRERO and Osiris [15] have been explored. One of the issues faced by these designs is dealing with the miniature fallout associated with each fuel pellet injection and detonation. In each fusion event, the interior walls of the fusion target chamber is subjected to short pulses of high-energy x-rays, unburned DT-fuel particles, He-ash, and particle debris [16]. Ablation of the wall is expected to occur from the bombardment of energetic ions. In addition to the concern of long-time wall erosion [17], the ablation of wall material presents a chamber contamination concern [18]. The introduction of aerosols into the fusion chamber could disrupt the implosion performance of the DT fuel if significant laser scattering occurs [19][20]. IFE reactors are proposed to operate at a 10 Hz repetition rate. In order for this to be realized, chamber clearing of any contaminants must by satisfied in the short allotted time window between successive shots.

1.5 Experimental Techniques

1.5.1 Fast-gated Plume Imaging

During the early development of LPP, the plasma is composed of many different constituent species. To varying degrees, the ablation process expels energetic ions, neutrals, molecules, and clusters. An atomic or molecular species typically bear some excitation energy

which may be gained or lost through collisional exchange or alternatively released radiatively as an emitted photon. Using photoemissions, the species in the plume are imaged onto an ICCD through an objective focusing lens. The ICCD collects the full integrated spectrum (within design specifications), and from this is able to produce an image showing the overall shape of the plasma plume.

Typically, plume images are taken with exposure times significantly shorter than overall timeframe of the particular development trying to be observed. For instance, in colliding plasma, the onset of formation of the stagnation layer typically occurs on the order of tens of nanoseconds (depending on seed plume hydrodynamics and separation). To be able to observe the early formation of the stagnation layer, one could use a 5 ns exposure time which is much less than 75 ns (a typical onset time of plasma stagnation in this work). Twenty frames could be taken from 5 to 100 ns showing the formation of the stagnation layer. The exposure time is determined by the ICCD gate-width, the time the ICCD remains open for collection.

Timing settings of the ICCD include adjusting the gate-delay and gate-width. Adjusting the gate-delay changes the time at which the first collection (when taking multiple frames) is taken which is selected to observe different developmental stages in the plume development. Both gate-delay and gate-width can be set to increase incrementally with successive exposures. This can be either an arithmetic increase (additive) or geometric increase (multiplicative). Alternatively, no increase need be used.

Due to the limitations of the electronics, only one exposure can be taken per firing of the laser (triggering of the ICCD). Therefore, successive frames belong to entirely distinct plasmas (though they should be effectively identical). However, shot-to-shot deviations are inevitable due to (i) laser shot variability and (ii) surface modification of the target. The most notable

surface modification would be cratering due to many successive shots. This may be avoided by continually translating the surface or by minimizing the number of shot exposures to each target site. Shot-to-shot variability can be further reduced by implementing several accumulations for each successive frame. This effectively averages out experimental variance.

1.5.2 Monochromatic Plume Imaging

In this technique, a bandpass filter is placed in front of the objective focusing lens attached to the ICCD. It is otherwise identical to conventional plume imaging. Light from the plasma is directed (within some solid angle) towards the ICCD. Light residing within the transmittance bandwidth of the bandpass filter (BPF) is permitted to reach the ICCD while all other light is blocked. By shrewdly selecting the appropriate BPF, certain spectral features can be discriminately imaged in the manner described in the above section. Such features could include strong bound-bound transition lines of ions and neutrals or rovibronic molecular emissions. In this fashion, monochromatic imaging can be used to map various excited atomic and molecular species in the plasma. Careful selection of the BPF should be exercised to minimize the effect of multiple conflating emission sources residing within the BPF bandwidth. Using *laser-induced fluorescence*, species still present in the plasma can be re-excited and observed at later times in the plasma plume development.

1.5.3 Optical Emission Spectroscopy (OES)

In plasma diagnostics, acquiring the emission spectrum of a plasma is often an indispensable tool in understanding the makeup of the plasma. Spectral features can be used to

identify the various charge states of constituent elemental species as well as to identify the existence of transient molecules. *Optical emission spectroscopy* (OES) is a passive technique used to acquire such a plasma emission spectrum. In this technique, the luminous emission passes into the spectrograph through a slit located some stand-off distance from the plasma source. Within the spectrograph, the "white light" emission is spectrally dispersed with a grooved grating. The dispersed light is illuminated onto a detection matrix (e.g. CCD) which has been calibrated to provide an accurate emission spectrum. A more complete description of a Czerny-Turner type spectrograph is provided in Section 2.3.

A common practice with OES is to select a short gate width in reference to the plasma lifetime during which light is collected. Using a short gate-width provides for excellent time resolution. By doing this at different delays from plasma-formation, an understanding of how plume species emerge and diminish during the lifetime of the plasma can be understood. Alternatively, using a very long gate-width is used when greater interest is placed in maximizing the signal. This is often the case when conducting forensic spectroscopy (e.g. LIBS, LAMIS). In this case, there is little interest for discerning temporal onset of individual spectral features.

Many different processes may simultaneously occur in a plasma at any given time, giving rise to different spectral features. Hot plasma is likely to exhibit Bremsstrahlung emission from decelerating ions in the plasma. This appears as a high baseline continuum emission. Bound-bound atomic transitions from excited ions give rise to strong line emission. As the plasma cools, the population of ionized atoms recedes and plasma free energy becomes conducive for the formation of molecules (provided the plasma is still adequately collisional, dense). Atomic line emissions and molecular band emissions may be observed as well. Condensation occurs at much later times on the millisecond time-scale.

1.5.3.1 Electron Temperature Determination from Boltzmann Plots

In laser-produced plasma research, optical emission spectroscopy (OES) of the developing plasma offers an abundance of information about key plasma parameters. Electron temperature may be determined via the Boltzmann plot technique by comparing line intensities from multiple transitions belonging to a single plasma species. Per Boltzmann statistics, plotting $\ln(I\lambda/Ag)$ against E will produce a plot which may be fitted with a linear regression, $-1/kT$ being the slope to that linear fit (I, emission line intensity; λ, emission wavelength; A, atomic transition probability; g, statistical weight of the upper level of transition; E, excitation energy; kT, plasma temperature in eV). When determining temperature using the Boltzmann plot technique, it is important to select lines which span a range of values for the upper energy level. This allows greater coverage of the Boltzmann plot space, reducing potential method application error when implementing the linear regression. A typical Boltzmann plot procured from a spectrum bearing our five emission lines of interest is also shown in Figure 1.2.

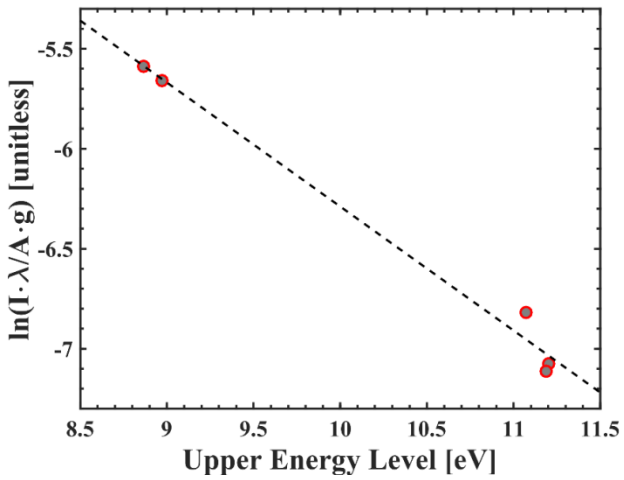

Figure 1.2 Typical Boltzmann plot: electron temperature may be determined from the slope ($-1/kT$) of the fitted linear regression.

1.5.3.2 Electron Density Determination by Measuring Stark Broadening

The electron density of the plasma may be ascertained from the spectral line width of a prominent bound-bound transition selected from the emission spectrum. High electron density within the plasma instigates Stark broadening of the line. This is caused by perturbations of atomic energy levels arising from a high local electric field enhancement. Literature provides temperature-dependent Stark broadening parameters which we may interpolate across different temperatures to determine approximate electron density [21]. Multiple unique mechanisms concurrently contribute to line broadening (e.g. Doppler, pressure, instrumental) which should be subtracted from the empirically measured width to accurately determine Stark broadening and electron density. Ideally, we seek a prominent, well-isolated emission line with suitable invariance of its Stark broadening parameter to plasma temperature. The electron temperature (e.g. determined via Boltzmann method) is used to provide the Stark broadening parameter by performing linear interpolation with literature values. The line is captured using the grating with the greatest groove density (spectral resolution) and is then fitted with a Lorentz fit (e.g. using Origen© software). The electron density is finally calculated using the relation: $\Delta\lambda_{½} = 2*w(T_e)$ $(n_e \times 10^{-16})$ ($\Delta\lambda_{½}$, Stark broadening FWHM [Å]; $w(T_e)$, temperature-dependent Stark broadening parameter [Å]; n_e, electron density [cm^{-3}]) [22]. This formulation does not include the ion correction which is permissible since ion contribution to Stark broadening is marginal in the current treatment.

1.5.4 Local Thermodynamic Equilibrium

The plasma must be in local thermodynamic equilibrium (LTE) to properly exhibit Boltzmann statistical behavior. The Boltzmann plot method for determining electron temperature is invalid if the plasma is not in LTE such as during transient heating by the laser pulse. It can be predicted whether the LTE condition is met by invoking the McWhirter criterion, mathematically expressed as n_e [cm^{-3}] > 1.6×10^{12} $T^{½}$ ΔE (n_e, electron density; T, plasma temperature in K; ΔE, difference between upper and lower energy level of transition in eV) [22].

1.5.4.1 Line Broadening

Line broadening is a natural phenomenon whereby any particular line transition will attain some finite spectral bandwidth. The discrete nature of the bound-bound transition might suggest that the line width is precisely zero, but this is in fact specious. A line possesses inherent broadening attributed due to the uncertainty of the transition's natural lifetime, τ (decay time). To satisfy Heisenberg uncertainty ($\Delta E \Delta t > \hbar/2$), energy levels assume this uncertainty which bestows the transition with a finite, nonzero spectral width. In a real plasma encountered in nature, other forms of line broadening significantly contribute thus the empirically measured line width is many times greater than the inherent line width.

Some of the more poignant forms of line broadening include Doppler broadening, pressure broadening, instrumental broadening, and Stark broadening. Stark broadening, introduced earlier, is the line broadening which occurs when the energy levels involved in the atomic transition become perturbed by an external electromagnetic field. This is principally caused by the electron population and may therefore be used to approximate the electron density of the plasma. Doppler broadening occurs in a plasma which exhibits a velocity distribution of

particle motion. Due to the eponymous Doppler effect, the light received from particles with different velocity will experience either slight redshift or blueshift, resulting in spectral broadening of all transitions. Doppler broadening may be estimated using the equation $\Delta\lambda_D(1/2) = 2\sqrt{ln2}\sqrt{2kT_r\lambda_0^2/M_Rc^2}$ ($\Delta\lambda_D$, Doppler FWHM line width; T_r, plasma temperature; λ_0, emission wavelength; M_R, atomic mass; c, speed of light in vacuum) which is typically on the order of 0.01-0.1 Å [23].

The plasmas generated here are sufficiently low density for us to neglect pressure broadening. In this effect, the collision frequency is sufficiently high such as to alter the population distribution surrounding the upper energy level. Atoms become more broadly distributed around the nominal energy level due to collisional energy transfer. Since the laser-produced plasmas considered here are created in vacuum conditions (~10^{-6} Torr), pressure broadening is neglected. Pressure broadening increases from a low ionization fraction but the plasmas are sufficiently low-density for this to matter in the developed laser-plasma plume.

Instrumental broadening is a form of line broadening which arises [chiefly] from the width of the slit aperture to the spectrometer. When deciding the slit width, there is an inherent tradeoff between spectral resolution and signal intensity. By opening the slit wider, more light is allowed in for greater signal. Reducing the slit width improves spectral resolution but at the expense of a diminished signal collected from the observed plasma. When collecting spectra for purposes of determining electron density (viz. measuring Stark broadening), we optimize the slit width parameter by considering other limiters to spectral resolution. When using an intensified charge-coupled device (ICCD, Section 2.3.2), each pixel corresponds to a finite spectral width. There is no point in having an instrumental spectral resolution much less than this since the accuracy of electron density measurements inherently suffers when spectral width need be

measured to such precision. Instrumental broadening is certainly significant in the line broadening of empirically acquired spectra, but it can be empirically approximated using a pen ray lamp such as from an HgAr fluorescent discharge. The emission spectrum exhibits very narrow lines, making the measured line widths from the spectrometer commensurate to the instrumental broadening.

2. CMUXE FACILITIES AND CAPABILITIES

Purdue Nuclear Engineering's *Center for Materials Under eXtreme Environment* (CMUXE) boasts a suite of pulsed laser systems and plasma diagnostic equipment which make this facility especially well-equipped for experimental study laser-produced plasma fundamentals. Two laser laboratories were used in these studies: the Laser-Produced Plasma (LPP) Laboratory which emphasizes the laser plasma generated from nanosecond pulse lasers (Nd:YAG and CO_2) and additionally the High Energy Density Physics (HEDP) Laboratory which hosts an ultrafast Ti:sapphire femtosecond laser. Additional spectroscopy, plume imaging, and plasma diagnostic equipment were present in both facilities.

2.1 Vacuum Chamber Systems

Either one of two different vacuum chambers (one for each laser lab) was used during the course of each individual experiment though the designs are fundamentally the same (stainless steel, 20" inner radius). Both house an optical breadboard secured to the base which secures a XYZ translation stage equipped with motorized actuators (Thorlabs, Inc.) in addition to any focal optics. Material targets would be affixed to the translation stage where they are subjected to pulsed laser irradiation along the optical beam path. High-vacuum experiments were usually conducted at 10^{-5} Torr, but chamber pressure could reach 10^{-7} Torr if allowed to pump down for several days.

The vacuum chamber in the LPP lab was manufactured by Nor-Cal Products, Inc. (Figure 2.1) and is fitted with an Alcatel rotary van pump, Model 2021SD (400 l/m, 14.6 CFM, UV <1e-

4 Torr) for rough pumping and a Leybold TURBOVAC 361 (C) ClassicLine turbomolecular pump (345 l/s, <1e-10 mBar ultimate pressure) to achieve high vacuum upon opening a gate valve to the chamber. The Alcatel Model 2021SD was also used to remove back pressure from the turbomolecular pump. Chamber pressure was determined using a miniature ionization vacuum gauge with dual convection gauges (IntruTech, IGM-402 module).

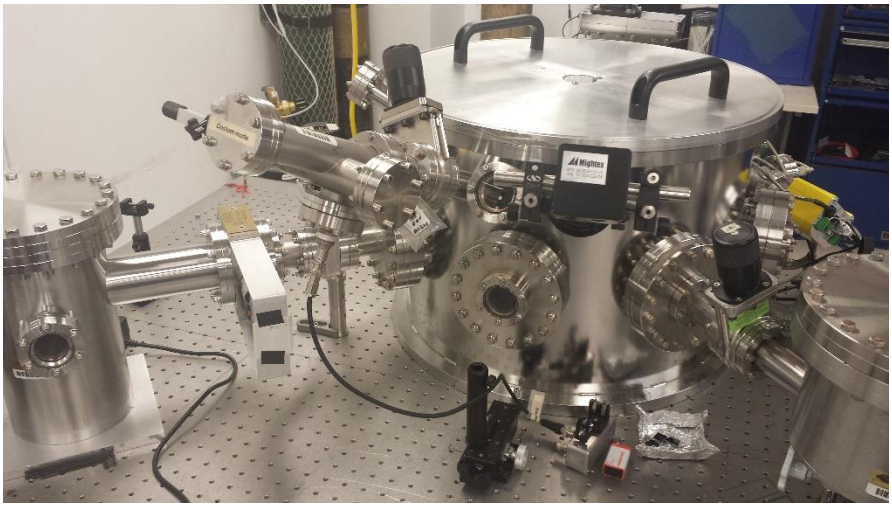

Figure 2.1 Vacuum Chamber (Nor-Cal Products, Inc.) in LPP lab. The vacuum chamber in the HEDP lab is essentially the same. At any given time, various diagnostic equipment is attached or detached from different access ports of the chamber.

In the HEDP lab, the vacuum chamber was manufactured by MDC Vacuum Products Corp. High vacuum was reached using an Adixen ATH-500M (400 l/s) turbomolecular pump similarly through opening a gate valve. High vacuum pressure readings were provided using a Pfeiffer vacuum PKR 261 full range gauge and a Pfeiffer single gauge TPG 261 single channel measurement control unit while pressures approaching atmospheric were again read using IntruTech IGM-402 module vacuum gauges.

2.2 Lasers

CMUXE is in ownership of multiple Class 4 lasers including Nd:YAG, TEA CO_2, Ti:sapphire, and tunable OPO models. A brief description of each and their operational capabilities will be provided. All lasers were operated while using laser safety goggles appropriate for the wavelengths being used.

2.2.1 Nd:YAG Models

CMUXE is in possession of three nanosecond pulse capable Nd:YAG (neodymium-doped yttrium aluminum garnet; Nd:$Y_3Al_5O_{12}$) which lase at 1064 nm. These standard research lasers are easy to operate and maintain. Two were used in the experiments comprising this body of work to generate laser plasma: the Continuum Surelite III and the Continuum Surelite I-10. These will be discussed in terms of output laser parameters (beam profile, pulse duration, max energy). The pulse energy was regulated using a combination of a polarizing cube and waveplate. The waveplate allows one to adjust the beam polarity while the polarizing cube splits the beam through a birefringent interface into s- and p- polarizations. The preferred polarization is relayed into the chamber while the rejected polarization is safely delivered to a beam dump. The alternative method of prolonging the Q-switch delay was not practiced since it has the deleterious consequence of also lengthening the pulse width. These lasers deliver a (mostly) Gaussian pulse, spatially and temporally.

2.2.1.1 Continuum Surelite III

This Continuum Surelite III is a Q-switched flash-lamp-pumped Nd:YAG laser capable of delivering 800 mJ pulses at a peak repletion rate of 10 Hz. To ensure good beam quality, the flash-lamps continually scintillate at 10 Hz repetition which serves to maintain a steady cavity environment. The pulse width can be modified by changing the Q-switch delay triggered after each flash-lamp strobe. The shortest pulse width (6 ns) is attained under an optimal Q-switch delay of 230 μs. The output beam possesses a beam diameter of about 10 mm which can be reduced using focusing optics.

2.2.1.2 Continuum Surelite I-10

The Continuum Surelite I-10 is an almost identical design to its newer cousin, the Continuum Surelite III, except for a few differences. Both are Q-switched, flash-lamp-pumped Nd:YAG lasers with 6 ns pulse width (180 μs Q-switch delay). However, the Surelite I-10 outputs a narrower unfocused beam with 6 mm diameter and has a lower maximum pulse energy of 400 mJ.

2.2.2 TEA CO_2 laser, SP 7000

The TEA CO_2 laser SP 7000 model is a standard pulsed CO_2 laser which operates on principles pertaining to gas lasers. The CO_2 laser invokes a gas discharge as its active laser medium. The gas mixture contains CO_2, N_2, and He with an approximate ratio of 1:2:8. CO_2 is the lasing species (λ = 10.6 μm), N_2 assists in enabling CO_2 population inversion, and He helps

depopulate lower energy levels of CO_2 and additionally serves as a coolant. The SP 7000 is a Transversely Excited Atmospheric (TEA) laser and thus operates its gas discharge in this manner: transverse electric discharge of the gas mixture. Due to the molecular nature of the lasing species, the emission wavelength is in the long-wavelength infrared (LWIR) at 10.6 μm.

The SP 7000 is rated for a 1 J pulse energy at a maximum repetition rate of 10 Hz. The beam waist dimension is 15 mm. The temporal profile of the CO_2 laser consists of a high intensity initial spike followed by a long tail due to the N_2 admixture. The initial pulse has a 40 ns pulse width whereas the nitrogen tail extends for approximately 1 μs. A plasma shutter may be used to clip the nitrogen tail, leaving only the leading pulse. In this configuration, a ZnSe lens is used to focus the beam through a small pinhole. The wings of the pulse are used to excite electrons from a metallic material composing the aperture's rim. These seed electrons induce atmospheric breakdown, forming a plasma which shields the trailing portion of the pulse. The transmitted portion of the plasma is then collimated through a second ZnSe lens. Pulse clipping may be implemented to prevent the deleterious deposition of extraneous energy from the nitrogen tail to the plasma.

2.2.3 Tunable OPO laser, Radiant HE 355 LD

The Radiant HE 355 LD tunable laser system operates by means of the optical parametric oscillator concept. In this system, light from a third harmonic Nd:YAG laser (λ = 355 nm) supplies energy into a resonant cavity which achieves optical gain through parametric amplification in a nonlinear crystal rather than from stimulated emission in a traditional gain medium. The appeal of this design concept is its continuous access to a spectrum of wavelengths ranging in the visible to mid-infrared (λ = 410-2400 nm). All wavelengths in this range are

realizable so long as the phase matching criterion is met. Historically, the shorter wavelength is referred to as the signal whereas the longer wavelength is the idler. The immediate appeal of such a laser is apparent in its utility in laser spectroscopy applications [24].

A consequence of the phase-matching criterion for determining accessible wavelengths is that the maximum pulse energy is wavelength dependent. Figure 2.2 shows the range of accessible wavelengths and the respective maximum energy of each. It can be seen that the signal operates within 410-710 nm while the idler can access wavelengths 710-2400 nm. It can be seen that a maximum pulse energy of 70 mJ can be produced using a 425 nm signal beam. All other wavelengths can be produced at only a fraction of this energy. In addition to the OPO cavity, the Radiant HE 355 LD includes access ports for its 1064 nm Nd:YAG pump laser and additional ports which enable access to second and third harmonics (512 nm and 355 nm) of the Nd:YAG laser.

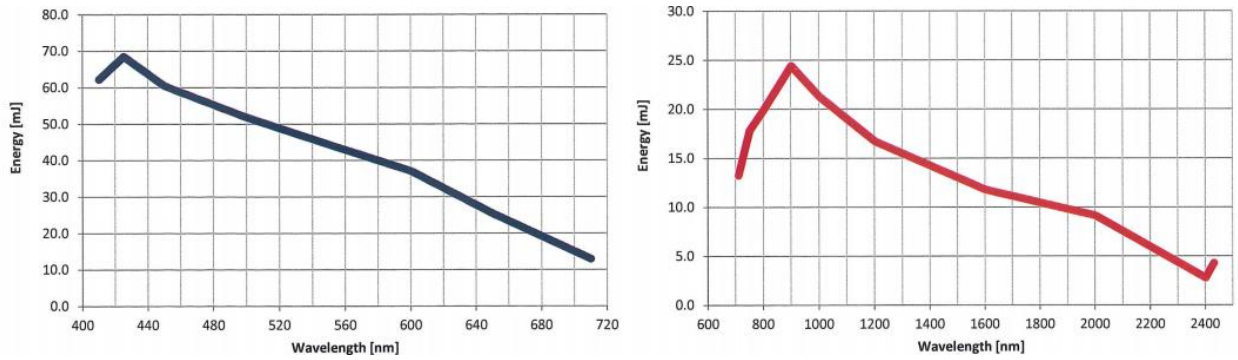

Figure 2.2 Maximum pulse energy for signal (blue) and idler (red) of the Radiant HE 355 LD tunable OPO laser across the full range of accessible wavelengths.

2.3 Spectrograph/Monochromator

2.3.1 Czerny-Turner style monochromator/spectrograph, Acton SP-2500i

An Acton SP-2500i Czerny-Turner style monochromator/spectrograph (500 mm focal length) equipped with a triple grating turret was used for plume spectroscopy. Three diffraction gratings are accessible: 150 grooves/mm, 600 grooves/mm, or 1800 grooves/mm, corresponding to effective dispersions of 13 nm/mm, 3.1 nm/mm, and 0.8 nm/mm and resolutions of 0.335 nm, 0.082 nm, and 0.023 nm respectively. A 32-bit microprocessor controlled direct digital scanning (DDS) system is used for the grating drive system.

The spectral window of effective operation resides in the UV-VIS range 250-800 nm. Using the 150 g/mm grating, a spectral window spanning 175 nm may be observed, making it excellent for identifying and comparing various emission features or for excitation temperature calculation. Using the 1800 g/mm grating, the spectral window compresses to a 12.6 nm span but with much higher resolution. For this reason, this grating is most effectively used for discerning line broadening for plasma density determination. The 600 g/mm grating offers a balanced medium between the two (42.9 nm spacing) and may be used to obtain good spectra of molecular bands or closely spaced lines.

2.3.2 Intensified Charge-Coupled Device (ICCD), PI-MAX2

Dispersed light from the spectrograph may be cast onto an intensified charge-coupled device (ICCD) camera through an exit port. A Princeton Instruments PI-MAX2 uses a proximity-focused microchannel plate (MCP) image intensifier fiber-optically coupled to a CCD array was used to optically capture transient plasma phenomena. The CCD array itself consists

of 1024 × 1024 pixels, each 13 μm × 13 μm. The PI-MAX2 may operate in either shutter mode or gate mode depending on what measure of gating is preferred. In gated mode, a fast-pulse option with a 2 ns gate-width permits capture of the brightest plasma emissions during the earliest stages of the LPP process. For dim plasmas, a gain could be applied to multiply the signal. Alternatively, the exposure gate-width could be increased (though at a loss of temporal resolution for time-resolved studies). External triggering of the PI-MAX2 could be achieved (e.g. using a programmable timing generator) to sync the various laboratory equipment with precision timing accuracy. For best performance, the detector was cooled to -20°C during operation.

2.3.3 Photomultiplier tube (PMT), Hamamatsu R298

With controlled exit port selection of the Acton 2500i monochromator, the dispersed spectra could be diverted from the ICCD and instead sent through an exit slit. Attached to the exit port is a photomultiplier tube (PMT, Hamamatsu R298) which is sensitive to light in the 185-900 nm window (which exceeds the bounds of the spectral range of the Acton SP-2500i). Peak quantum efficiency of 25.4% occurs at peak wavelength of 260 nm. The PMT also features a 10^7 gain with 2.2 ns rise time. In operating the PMT, a bias voltage of ~1150 V is applied via a dedicated high voltage DC power supply (Acton PHV-400). The PMT can be interfaced with an oscilloscope to produce optical time-of-flight (OTOF) plots. In doing this, the 1800 grooves/mm grating is used to ensure optimal spectral selection.

2.4 Fast-gated Imaging

Imaging of the developing plasma plumes was accomplished using the same PI-MAX2 ICCD used with the spectrograph for taking emission spectra. However, the ICCD is liberated from the spectrograph housing and fitted with a Nikon objective focusing lens attachment. Shutter and gate exposure modes are similarly available for plume imaging though shutter mode operation is generally only used during alignment. In performing monochromatic imaging, bandpass filters (BPF) would be placed in front of the focusing objective. The transmission curve of a BPF typically has a 10 nm FWHM bandwidth with peak transmittance of about 60% at the center wavelength (CWL). Beyond the wings of the transmittance window, an optical density (OD) of 4 is typical (10^4 factor reduction).

2.5 HEIGHTS Computational Modeling

HEIGHTS computer package [25][26] includes detailed models of all main processes for the description of laser produced plasma (LPP) development, dynamics, and collision. The solution of the general equation set detailing a full description of the LPP system is split to solve five major components separately: laser energy deposition, target heating and erosion, vapor/plasma hydrodynamics, thermal conduction in plasmas, and radiation transport. Various numerical methods are employed for the description of each of the above processes. The package self-consistently integrates Monte Carlo models for laser beam interactions with the solid target, vapor, and plasma; Monte Carlo modeling of plasma radiation and photon transport; explicit high order schemes for target evolution and vapor/plasma dynamics; and implicit solution of thermal transport in vapor/plasma. Atomic properties and optical coefficients are

calculated using the self-consistent Hartree-Fock-Slater (HFS) method and the collisional-radiative equilibrium (CRE) model. HFS calculations determine the structure of atomic energy levels, wave functions, transition probabilities, ionization potentials, oscillator strengths, broadening constants, photoionization cross-sections, and other atomic characteristics [27]. The CRE model is used to calculate the populations of atomic levels and the ion and electron plasma concentrations. Ion and electron concentrations found from the CRE model are used in the equations of state to calculate the pressure and internal energy. A detailed description of all the methods integrated in the HEIGHTS computer package can be found elsewhere [28] The package had been benchmarked and used for the optimization of LPPs for EUV and soft x-ray sources [25].

The self-consistent and integrated models implemented in the HEIGHTS package allow the accurate simulation of the entire process of LPP evolution. All laser photon interactions with target/media are described using Monte Carlo techniques. Initially, the laser beam propagates through the optically transparent chamber environment interacting with the solid target only. Laser photon absorption/reflection from the target surface is determined based on experimental optical constants. Subsequent material heating and evaporation lead to target surface recession and vapor expansion described by fluid dynamics. This leads to laser photon interactions with vapor based on the collision-induced absorption mechanism and initiates photon absorption in an evolving plasma by inverse bremsstrahlung. The macrocharacteristics of the evolved plasma are determined from the precalculated and tabulated optical and thermodynamic data using HFS/CRE approaches. The energy distribution in the vapor/plasma domain is determined by five processes: evaporated particle kinetics, laser energy deposition, fluid dynamics of the vapor/plasma, electron thermal conduction, and plasma radiation and transport. A suitably small

time-step allows consequent simulation and integration of all processes without any oscillations and with the accurate prediction of laser energy deposition in the target and vapor/plasma.

3. PLUME HYDRODYNAMICS AND SPECTROCHEMISTRY IN COLLIDING CARBON LASER-PRODUCED PLASMAS[1]

In this chapter, the hydrodynamic processes giving rise to the formation of stagnation layer in colliding carbon plasmas was investigated. Carbon species (i.e. C_2, C(I), C(II), and higher charge states of C) were assessed for their spatiotemporal occurrence in colliding carbon plasma produced from the laser ablation of planar graphite targets. The purpose of this was to obtain a better understanding of the stagnation plume creation and evolution and to acquire a fuller understanding of the processes occurring within. The fundamental physics governing colliding plasma was introduced in Section 1.4 and is being applied here for two colliding carbon plasmas.

3.1 Introduction

Colliding plasmas warrant interest due to a higher degree of collisionality than those of individual LPPs. This disparity should be expected to be more pronounced for LPPs placed within a low-pressure environment ($< 10^{-1}$ Torr) or in vacuum. High induced collisionality is an important characteristic of plasmas since it increases the plasma temperature and enhances reaction rates, such as recombination, within the plasma. This property is particularly consequential in carbon plasmas since carbon is well-suited to chain together, forming large compound structures. In an inertial fusion device, this presents a concern since the large macromolecules following each fusion event could pose as a detriment to successive shots.

[1]T. Sizyuk, J. Oliver, and P.K. Diwakar, "Mechanisms of carbon dimer formation in colliding laser-produced carbon plasmas," J. Appl. Phys., vol. 122, p. 023303, 2017.

The most intriguing products formed in the carbon plasma would certainly be fullerene structures. A fullerene is a particular molecule of carbon which exhibits the closed form of a hollow sphere, ellipsoid, or tube. In 1985, the first buckminsterfullerene (hence coined "buckyball") was discovered in the laser ablation of graphite in a helium gas buffer [29]. Since then, other large carbon fullerene structures (i.e. single-walled nanotubes, multi-walled nanotubes, and fullerite) have also been identified.

Colliding plasmas also incur collisional re-excitation of species in the plasma which can amplify their spectral signature. In colliding carbon plasma, Swan band emission from C_2 dimers is greatly enhanced [6]. Laser-Induced Breakdown Spectroscopy (LIBS) is an atomic emission spectrometry technique used in forensic composition analysis [30][31][32]. An offshoot of LIBS, LAMIS (Laser Ablation Molecular Isotopic Spectrometry), is a similar optical technique used for isotopic analysis [33]. Colliding plasmas could potentially offer a means to increase the effectiveness of LAMIS in low pressure or vacuum environments.

The preexisting collection of work on carbon laser-produced plasmas had been directed mostly towards non-colliding plasmas. Similar inquiries into mapping the various carbon species produced in the colliding plasma have been explored at the time this is being written though not with sophisticated modeling [34]. Their findings elucidate the various mechanisms by which C_2 is manifests during the laser ablation and collision processes, many of which apply to the work presented here. Extending this body of knowledge to the colliding plasma regime is important because it explores the early conditions for the synthesis of large carbon compounds under plasma conditions which haven't been much explored.

3.2 Experimental Setup

A schematic of the experimental setup is shown in Figure 3.1. Seed plasmas were produced using a single laser pulse (1064 nm, 6 ns Nd:YAG) which was split into two arms bearing equal pulse energy (150 mJ). The laser pulse was split using an ensemble of two waveplates and two cube polarizers which allowed for fine tuning of pulse energy. The energy was measured at each respective chamber entrance using an Ophir NOVA II laser power-energy monitor to rectify for energy loss along the beam path.

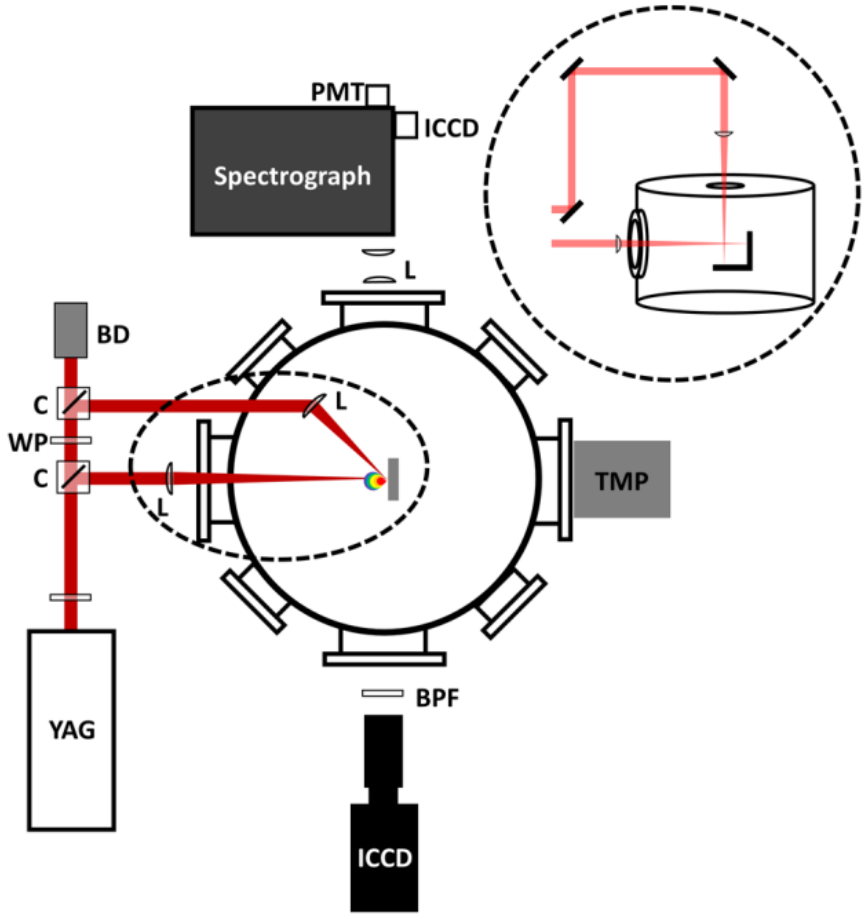

Figure 3.1 Experimental setup used in the study of colliding laser-produced carbon plasmas. Instrumentation used: Nd:YAG laser (YAG), Czerny-Turner spectrograph (spectrograph), intensified charge-coupled device (ICCD), turbomolecular pump (TMP), photomultiplier tube (PMT), bandpass filter (BPF), waveplate (WP), cube polarizer (C), beam dump (BD), and lenses (L).

The target assembly consisted of two planar graphite foils positioned at 90° to form a wedge and was propped as is seen in the inset in Figure 3.2. Each of the graphite faces was subject to an Nd:YAG laser pencil along the respective target-normal. The two individual beams entered the chamber and were individually focused using two 40 cm planoconvex lenses. The ablation sites were positioned such that the two plasmas were created each 5mm from the wedge corner. The target normals extruded from the two sites intersected such that skew collisions could be avoided. Three different laser intensities (5.1×10^{10}, 1.3×10^{10}, and 3.2×10^{9} W/cm^2) were investigated corresponding to three different focal spot sizes (250, 500, and 1000 μm). Laser beam parameters are summarized in Table 3.1. The pressure during data collection was maintained at 0.1 Torr of air ambient.

Table 3.1 Laser Parameters for Colliding Plasma Study

Intensity [W/cm^2]	**Spot size [μm]**	**Energy [mJ]**
5.1×10^{10}	250	150
1.3×10^{10}	500	150
3.2×10^{9}	1000	150

A combination of plume imaging and spectroscopy diagnostics was used to provide empirical insights into the collision of carbon plasmas. Fast photography was done using an integrated charged couple device (ICCD) camera (PI-Max, Princeton Instruments) which provided detailed time-resolved observations of the colliding plasma within the time domain of plume expansion and collision. A focusing objective (Nikon) was used to obtain the focused view of the plasma plume. These observations provide a useful qualitative tool to understand

plume dynamics (i.e., plume stagnation and interpenetration). Further imaging involved selective placement of one of two different bandpass filters in front of the camera to perform monochromatic imaging (see Table 3.2). This permitted discriminatory observation of carbon C^{1+} ions and molecular C_2 dimers (viz., Swan band emission) from integrated spectral images. For each imaging series, a fixed (non-incremental) gate width of 20 ns was used to facilitate the absolute comparative assessment of emission intensities across the whole-time domain in the observed spectral window. Optical emission spectroscopy (OES) was performed using a 0.5m Czerny-Turner type spectrograph (Acton SP-2500, Princeton Instruments) with 150 grooves/mm grating at a fixed 30 μm slit width. OES spectra likewise used a constant gate width (25 ns) for collection. OES was used in tandem with monochromatic imaging to present complementary time- and space-resolved indication of carbon species emission. Triggering of the ICCD was accomplished using spectroscopy software delay settings and a 1 GHz digital oscilloscope.

Table 3.2 Observed Species Emissions with Appropriate Bandpass Filter

SPECIES	EMISSION	FILTER CWL
C^{1+}	656.7 nm	656 nm
C_2	510 - 516 nm	510 nm
C_3	390 - 430 nm	430 nm

*All filters have a 10 nm bandwidth

3.3 Plume Imaging

Plume imaging results were used to observe spontaneous photoemissions from the evolving plasma leading to the formation onset of the stagnation layer and soon thereafter. This method is most appropriate at early times in the plume development process (< 1μs) when large populations of plasma species are excited. By selectively placing bandpass filters in front of the

objective focusing lens, two particular carbon species (i.e. C^{1+} and C_2) were discriminately observed. In the following chapter, plume imaging will be conducted at later times exceeding 1 μs using laser-induced fluorescence (LIF) which further enabled C_3 to be observed.

3.3.1 Spectrally-Integrated Optical Emission Plume Imaging

Optical emission fast-gated plume imaging was used in this study to assess the dynamics of the colliding plume fronts of the two seed plasmas from the graphite targets and the subsequent development of the stagnation layer. Plume images were collected over the visible (VIS) spectrum for the three different explored laser intensities. Plume imaging during the first 250 ns of plume developments shows the onset of formation of the stagnation layer at around 100 ns (Figure 3.2). It is seen that the carbon plasma produces stagnation along the collision midplane of the two seed plumes. As time progresses, the stagnated plasma plume expands outward while being confined along its lateral dimension. This could be explained by continual pressure being supplied by the seed plumes. With the gradual abatement of seed plume expansion, lateral confinement of the stagnated plasma is effectively lost after 500 ns for all studied explored laser intensities.

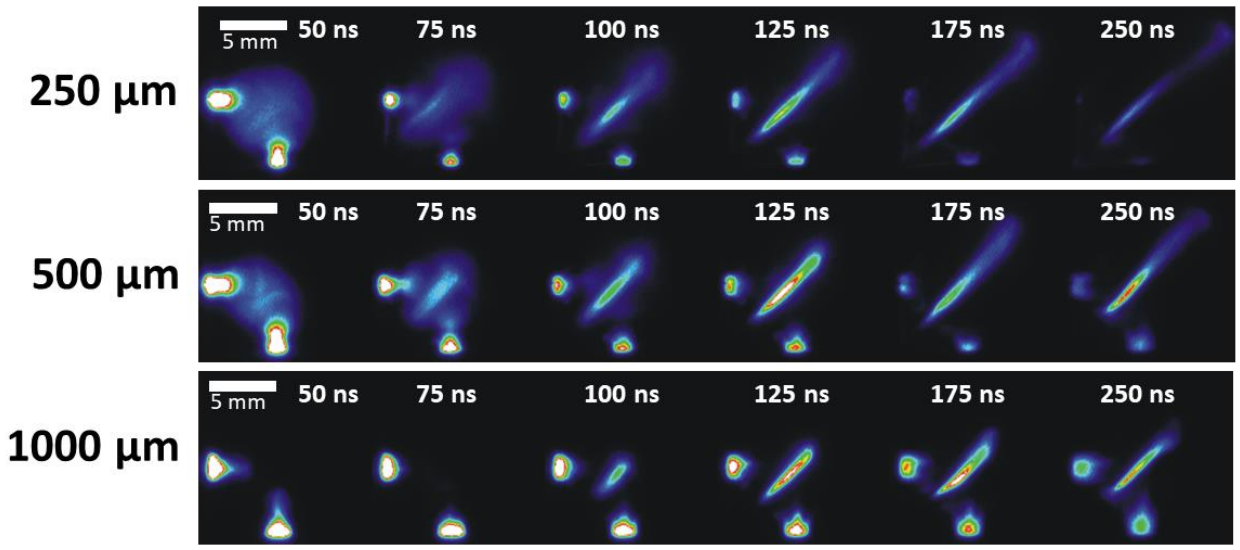

Figure 3.2 Plume imaging showing onset of formation of the stagnation layer in colliding carbon plasma during the first 300 ns using laser intensity (a) 5.1×10^{10}, (b) 1.3×10^{10}, and (c) 3.2×10^{9} W-cm^{-2}.

It should be recalled that the stagnation layer first forms via scattering collisions of fast ions first to reach the midplane. As ions are continually being fed to the nascent stagnation layer, collisionality increases provided ions do not escape due to outward diffusion. This condition is encompassed in the collisionality parameter or inverse Knudsen number (see Section 1.4.1). Per this criterion for stagnation, plasmas produced from a more intense laser are expected to interpenetrate, undergoing softer stagnation. This can be concluded due to higher expected ion velocities and therefore longer mean free path. More ions traverse the midplane without colliding, leading to a slower onset of formation of the stagnation layer. Additionally, a reduced portion of the total ablated inventory is available to continually resupply the stagnation layer and apply confining pressure.

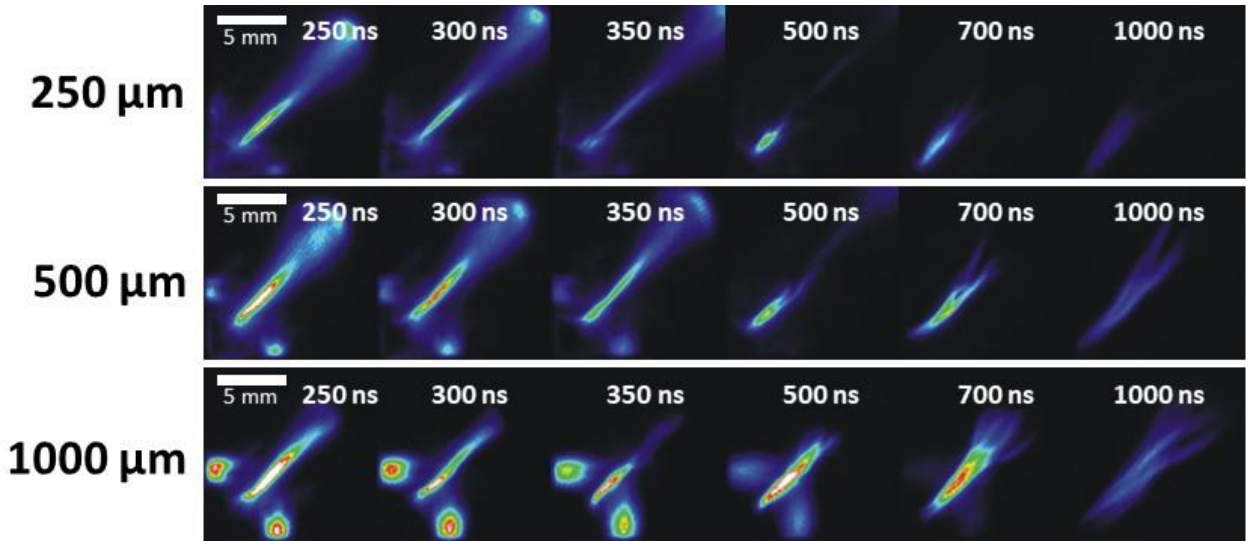

Figure 3.3 Plume imaging showing development of the stagnation layer in colliding carbon plasma through 1 µs using laser intensity (a) 5.1×10^{10}, (b) 1.3×10^{10}, and (c) 3.2×10^{9} W-cm^{-2}.

By examining Figure 3.2, it can be seen that the seed plasmas persist longer when lower laser intensity is used. In the high laser intensity scenario, the seed plasma has almost entirely dissipated by 250 ns. In the low laser intensity scenario, the seed plasma persists well until 500 ns as is seen from Figure 3.3. The result is a well-confined stagnation layer across its lateral dimension

3.3.2 Monochromatic Optical Emission Plume Imaging

Monochromatic plume imaging was conducted in an identical fashion to that of plume imaging conducted over the full VIS spectrum except that a choice bandpass filter was placed in front of the camera. The bandpass filter served to block all emissions except those falling within a desired bandwidth window (set by the bandpass filter). The ionic 657.8 nm C^{1+} line was observed as well as rovibronic emissions from the 0-0 Swan band of C_2 (Table 3.2, Section 3.2).

The two sets of monochromatic imaging for C^{1+} and C_2 are shown in Figure 3.4 and Figure 3.5 respectively. Our experiments could not effectively image carbon neutrals in this manner since the most prominent emission lines of carbon neutrals reside outside the spectral range of our imaging apparatus. In this study, a laser intensity of 1.3×10^{10} W-cm^{-2} was used (500 μm spot size).

3.3.2.1 C^{1+} Imaging

The C^{1+} monochromatic imaging results in Figure 3.4 reveals that C^{1+} ions persist in the stagnation layer for approximately 400 ns before becoming depleted from the stagnation layer plasma. As the stagnation layer plasma cools, electron-ion recombination processes occurring in the plasma around this time would account for this observance. At times earlier than 100 ns, the central core of the stagnation layer is too hot to sustain high C^{1+} populations. Around this time, higher charge states of carbon such as C^{2+}-C^{4+} exist. The C^{1+} emission actually appears to peak at around 200 ns. This occurs much later than the collision onset which is evidenced to occur at around 75 ns as was seen from Figure 3.3b. In a succeeding investigation of colliding plasma using wavelength-dispersed spectral imaging, the observance of prominent C^{2+} line emission at 464.7 nm early in the stagnation layer development substantiate this description.

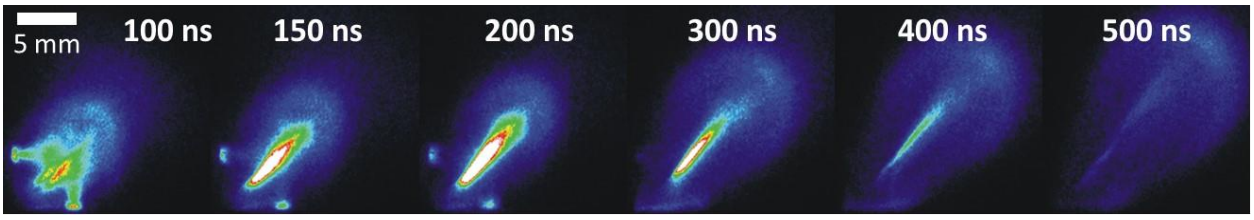

Figure 3.4 C^{1+} monochromatic plume imaging of 656.7 nm ionic line emission using a bandpass filter (CWL: 656 nm, FWHM: 10 nm) through 500 ns.

3.3.2.2 C_2 Imaging

C_2 molecular dimers were located using a 510 nm bandpass filter which selectively transmits (0–0) Swan band emission. The (0–0) Swan band provided high luminosity making it suitable for imaging. Monochromatic imaging for C_2 can be seen in Figure 3.5. The most intriguing trend that can be discerned from the images transpires at 350 ns. At the bottom of the stagnation plume, a high intensity region forms, occurring several hundred nanoseconds after the collision of the seed plasma has already transpired. We posit that this region corresponds principally to the emergence of C_2 species produced via dimerization of C neutrals from the seed plasmas. Through comparison of Figure 3.4 and Figure 3.5, we see that the seed plumes close to the graphite surface appear much more luminous in the C_2 imaging than in C^{1+} imaging. It has been observed in laser-produced carbon plasma that C_2 emerges in the near vicinity of the ablation site which is attributed to the dissociation of large carbon molecules ejected during ablation [35]. In this vicinity, the plasma is quite dense and bears a high electron density which incurs dissociation via electron impact. The emergence of C_2 in the stagnation layer is not, in fact, due to re-excitation of C_2 but rather from enhanced C_2 dimerization. At later time steps, the Swan band emitting region grows and extends upward along the collision midplane, achieving peak brilliance at around 700 ns. This climb can be interpreted as the ongoing dimerization of continually supplied C neutrals leading to C_2 synthesis.

It will later be se seen (Section 3.5) that the arrival of merging C neutral populations is synchronous with the emergence of C_2 in the stagnation layer. Carbon neutrals are essential for carrying out $C + C + R \rightarrow C_2 + R$ three-body recombination reactions (dimerization) where R is a momentum carrier. The timely preponderance of carbon neutrals accumulating in a certain region is indicative of C_2 dimerization. The observed outward extension of the Swan band

emitting region would similarly be explained by the continual introduction of carbon neutrals reaching higher parts of the stagnation layer.

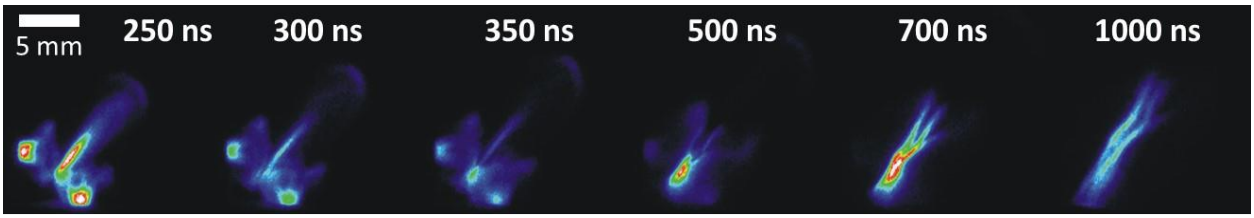

Figure 3.5 C_2 monochromatic plume imaging of (0-0) Swan band emission using a bandpass filter (CWL: 510 nm, FWHM: 10 nm) through 1 μs.

It should be mentioned as a caveat that a series of C^{1+} ionic lines with non-negligible luminosity reside in the window centered around 510 nm. These lines could bleed into the imaging of C_2. At such times, C^{1+} ionic line transitions would give false positive indication of C_2 Swan band emission. This only presents a concern when C^{1+} ions are greatly abundant. As seen from Figure 3.4, this only presents a concern before 300 ns. Through comparison between Figure 3.4 and Figure 3.5, it is elucidated that the stagnation layer at 250 ns could comprise C^{1+} ionic line emission but certainly not the seed plasma (the ratio of emitting intensities of the seed plasma and the stagnation layer are quite different). Confidence that the observed emissions at 350 ns can be ascribed to (0-0) Swan band emission is confirmed later in Section 3.4 with time-resolved wavelength-dispersed spectral imaging. Similarly, emissions before 350 ns will be shown to be ionic in nature.

3.3.3 Plume Imaging of Seed Plasma

To possess confidence in any spectrochemical interpretation of the stagnation layer, it is necessary to understand the nature of the individual seed plumes. Plume imaging of an individual seed plume is shown in Figure 3.6. Through the ICCD software, logarithmic intensity scaling and incremental gating were used to accentuate certain plume features. These tools were not used in the imaging of the colliding plasmas since an accurate representation of the stagnation layer emissions is paramount. Introducing an incremental increase in the gate width of exposure would greatly exaggerate these emissions.

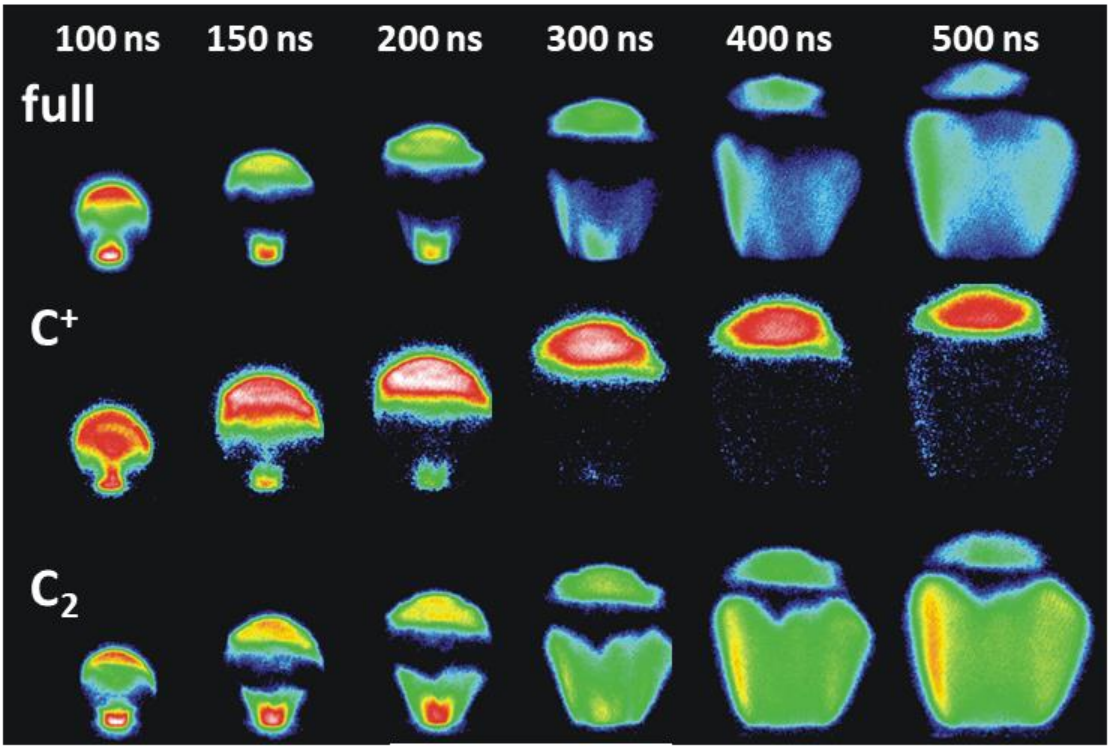

Figure 3.6 Plume imaging of individual carbon plasma in 0.1 Torr air ambient from 100-500 ns including the full visible emission spectrum (top), 657.8 nm C^{1+} emission (middle), and ~510 nm C_2 emission (bottom). An exposure equal to 10% of the gate delay was used.

It can be seen in Figure 3.6 that the full, spectrally-integrated emission is chiefly the composite of emissions from a fast component of C^{1+} ions and slow component of C_2 dimers. The cap of the plume is heated through the highly collisional expansion into the 0.1 Torr air ambient. This heating is sufficient to maintain a large population of C^{1+} ions and retard expansion. In the collision of two such seed plasmas, it is the collision of the plume fronts of the two caps that initiates the formation of a stagnation layer. The second region, the C_2 region, lags the bow of fast ions in expansion. It starts small, restricted to the near ablation site. As the plume cap leads in expansion, it leaves a vacuous region in its wake which becomes occupied by C_2. We recall that C_2 is formed from dissociation in the close vicinity of the laser ablation site due to electron-impact dissociation of larger carbon molecules. In the space enclosed between the ionized plume front and the target surface, diffuse populations of C_2 preside. In this space, dimerization is occurring but at a slow rate.

3.4 Optical Emission Spectroscopy

While plume imaging offers immense value in ascertaining the spatial development of the colliding carbon plasmas, optical emission spectroscopy (OES) may be used to characterize the spectral nature of the plume emissions. By analyzing the emission spectrum, much information can be acquired. Plasma temperature data may be obtained through the Boltzmann plot method, and plasma density may be determined using the Stark-broadened profiles of prominent emission lines. Additionally, species identification through identifying various spectral signatures can be used in tandem with plume imaging to corroborate an understanding of the various mechanisms occurring in the plasma.

3.4.1 2D Wavelength-dispersed Spectral Imaging

3.4.1.1 Time-integrated Wavelength-dispersed Imaging

The time-integrated wavelength-dispersed spectrum of the stagnation layer was taken by mapping the slit along the axial length of the stagnation layer of the colliding plasmas (Figure 3.7). Immediately jumping out are the (1-0) and (0-0) Swan bands centered near 466 and 512 nm respectively. The brightest feature is the 426.7 nm C^{1+} ionic line transition. Other notable spectral features include additional violet C^{1+} lines, a strong C^{2+} line at 464.7 nm, and the (0-1) Swan band near 550 nm.

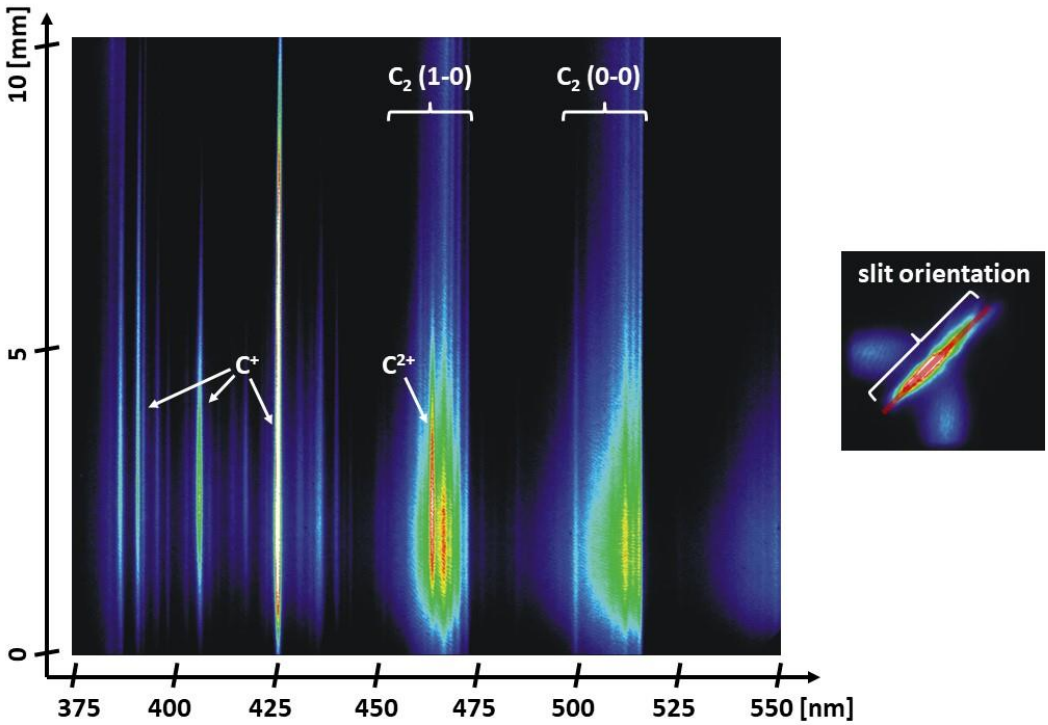

Figure 3.7 Wavelength-dispersed spectral imaging from 375-550 nm of the stagnation layer formed from colliding carbon plasma via a 2 μs time-integrated exposure through a 30 μm slit.

From Figure 3.7, it is seen that C_2 Swan band emissions principally emanate from the lower portion of the stagnation layer. This conclusion agrees with plume imaging previously shown in Figure 3.5. While the C^{1+} lines streak across the much of the slit length, the C^{2+} line at 464.7 nm is more spatially restricted. This region is understood to reach the highest plasma temperature, so it makes sense that higher charge states of carbon would be congregated there. Over the 2 μs time integration, the C^{2+} ions are expected to have undergone electron-ion recombination before transiting far outbound. Time-resolved wavelength-dispersed images will provide the necessary information to discern the temporal evolution of the stagnation layer.

3.4.1.2 Time-resolved Wavelength-dispersed Imaging

To track the populations of C^{1+} ions and C_2 dimers, it becomes necessary to examine time-resolved wavelength-dispersed images (Figure 3.8). It can be seen that at 100 ns, ionic line emission is dominant. This is true also at 300 ns, but the Swan emission is just starting to appear. Come 600 ns, the Swan band emission is quite prominent, and by 1000 ns, it nearly entirely comprises the totality of the spectrum. Recalling that in Section 3.3.2.2, we asserted that the emission around 510 nm after 300 ns was chiefly (0-0) Swan band emission, we can certify this claim now. An apparent C^{1+} line is observed at 514.5 nm at time 100 ns. This line appears only weakly at 300 ns and is entirely absent thereafter.

Another observed trend from the time-resolved spectral imaging is the outbound motion of C^{1+} ions. It should be intuitively clear that at early times, the C^{1+} lines should be positioned lower since this region is closer to the seed plasmas and thus ions streaming from the seed plasmas will reach here sooner. It then follows that the preferred motion of ions is outward (upward per Figure 3.8) along the collision midplane. Since this LPP study is being performed at

some ambient pressure, a degree of ionization is expected also along the leading bow front of the expanding plasma. By examining the monochromatic imaging results from Figure 3.4, this contribution appears to be more prevalent at later times succeeding 300 ns.

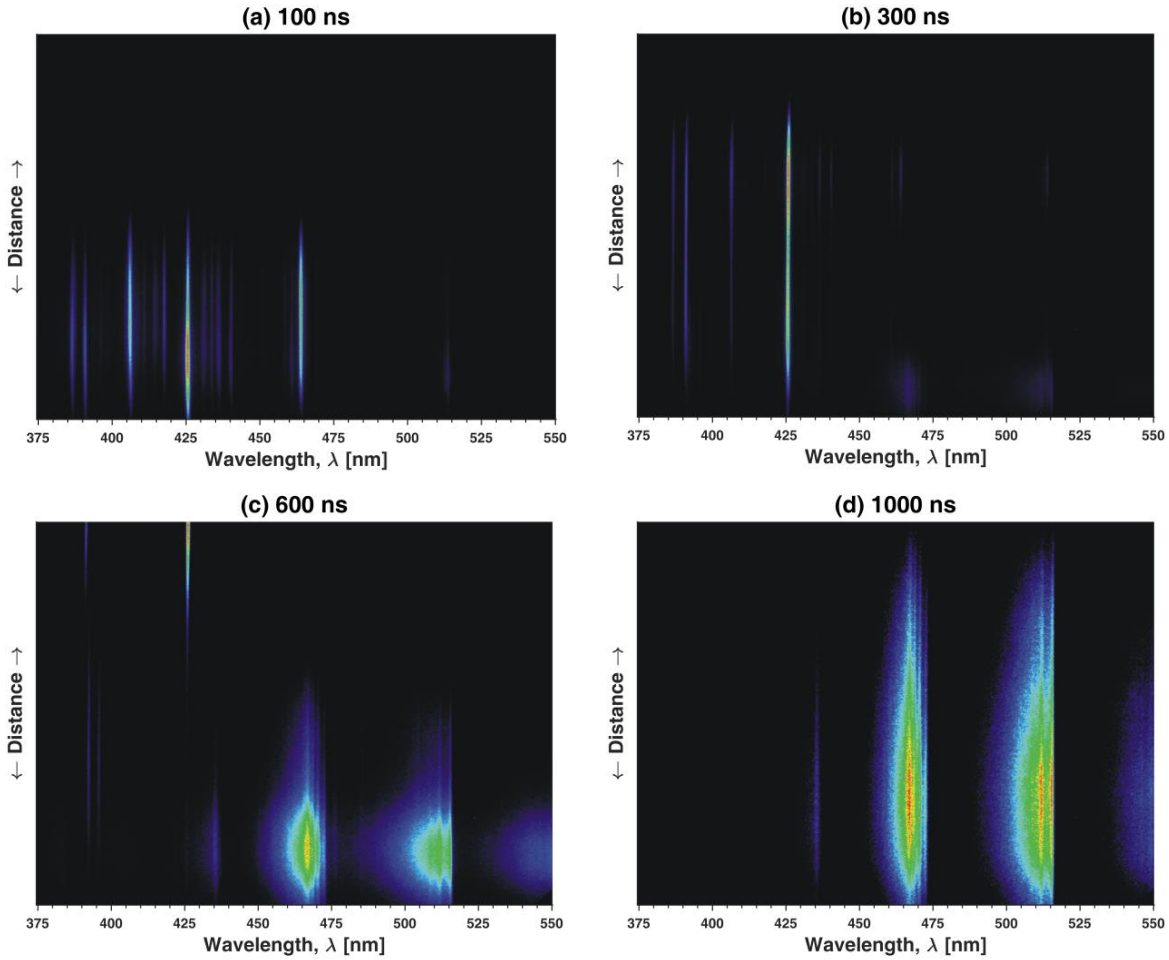

Figure 3.8 Time-resolved, wavelength-dispersed spectral images along the stagnation layer of colliding carbon plasmas taken at (a) 100 ns, (b) 300 ns, (c) 600 ns, and (d) 1000 ns. Exposures were taken using a 100 ns gate width and a 30 μm slit. Images are individually autoscaled to accentuate the relative spectral features.

3.4.2 Time-resolved, Spatially-integrated OES

Wavelength-dispersed imaging contains a great deal of information, but it is difficult to attain a quantitative understanding of how various emission features compare. Optical emission spectra can provide a complementary understanding in a more palatable format. Shown in Figure 3.9 are spectra taken at the three investigated spot sizes. In these spectra, the spectrograph slit was mapped onto the region in the stagnation layer which first exhibits appreciable Swan band emission (see 500 ns Figure 3.5).

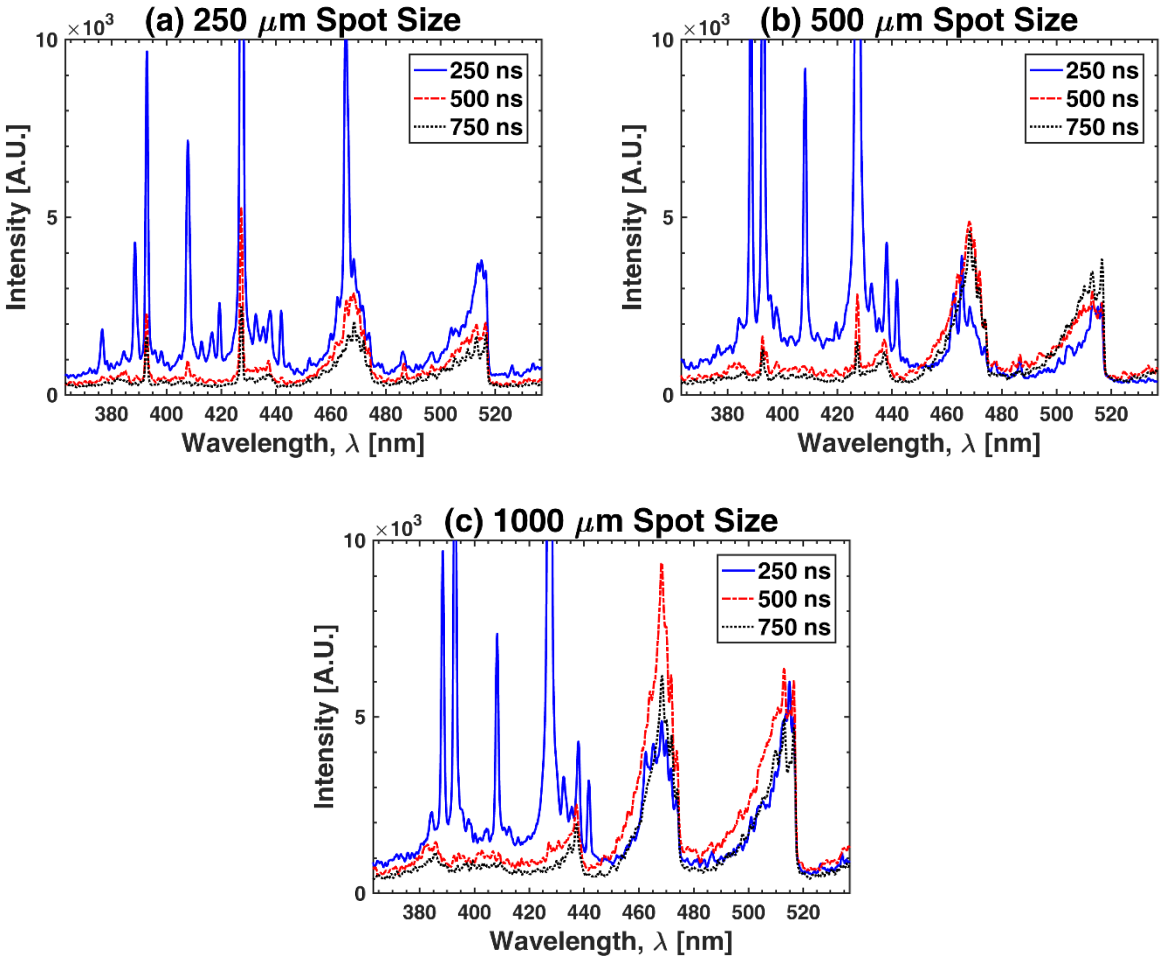

Figure 3.9 Time-resolved optical emission spectra of colliding carbon plasma using three spot sizes (a) 250 μm, (b) 500 μm, and (c) 1000 μm. Spectra were taken at three times: 250 ns, 500 ns, and 750 ns following Nd:YAG lasing.

Emission spectra for the carbon plasma were acquired in the 375–525 nm window to include numerous strong C^{1+} and C_2 emission lines and prominent (1–0) and (0–0) Swan bands. It should be recalled that the 657.8 nm C^{1+} ionic line used for the monochromatic imaging of C^{1+} ions resides outside the selected spectral window. However, preliminary spectra showed this line to be well segregated from other emission sources. For persistence purposes, the 392.1 nm C^{1+} ionic line is comparable. Per expectation, early time was dominated by ionic line emission. C^{2+} lines (namely, 464.7 nm) were relatively short-lived with C^{1+} lines (392.1 and 426.7 nm) persisting longer. To corroborate C_2 imaging from Figure 3.5, the (0–0) Swan band was assessed. When high laser intensities are employed, a greater number of ions achieve high charge states, which leads to increased ionic line emission. This is seen in Figure 3.9(a) as an anomalous peak due to the C^{2+} line contribution to the measurements of the (1–0) Swan band. In Figure 3.9(a) and (b), this is seen as uncharacteristic curvature of the rising slope of the (0–0) band. The curvature in Figure 3.9(b) is only slight at 250 ns, and so, we can claim that monochromatic imaging after this time correctly depicts the (0–0) Swan band emission of C_2 dimers.

In all three scenarios, Swan band emission appears at approximately 250 ns and persists for roughly 500 ns. The greatest yield of Swan emission occurs when the lowest laser fluence is used. Swan emission was shown to decrease with increased laser intensity (fixed pulse energy). A combination of several factors contributed to the observed magnitude of Swan band emission in the plasma environment created by lasers with the same energy and different spot sizes. Emission yield is a function of number density of the relevant emitting species and of plasma temperature, so both should be considered.

It was previously discussed in Section 3.3 that the low intensity scenario is favorable for stagnation layer formation. In high laser intensity scenario, the coupling of the laser with the

seed plasma results in greater laser-plasma interaction in a tighter volume. More laser energy is converted into ionization and kinetics of plasma species. The net effect is enhanced energetics of the expanding plasma and expedited rarefaction of the developing plume due to quick cessation of seed plume pressure. This also leads to enhanced interpenetration upon the collision of the seed plumes. With low laser intensity, a hot stagnation layer is pre-established by the fast ion component but with marginal interpenetration. In this manner, there is a greater utilization of the ablated matter in contributing to the plume stagnation. The spatiotemporal optimization of seed plasmas is appropriately dependent upon the laser parameters pulse energy and intensity (and therefore also spot size) which dictate plume energetics.

Spectra for individual single seed plumes were also briefly evaluated but evanesced rather quickly without giving rise to prominent Swan band emission. Still, when low laser fluence was used, Swan emission persists for several hundred nanoseconds albeit with much lower luminosity than that seen from colliding plasmas.

3.5 HEIGHTS Modeling

Experimental results were verified by 3D computational modeling using HEIGHTS simulation package. For a comprehensive summary of HEIGHTS, go to Section 2.5. The results are explained based on a fundamental analysis of plasma evolution, colliding layer formation, stagnation, and expansion. Three-dimensional simulations of a relatively large LPP system for modeling colliding plasma experiments up to a microsecond were conducted on a multi-processor system. Various algorithms were developed and optimized for task distribution among several processors. A non-uniform mesh was also used for fine spatial resolution of the target

surface region that allowed accurate simulations of target evolution. Exact experimental parameters were used in the modeling of colliding plasmas.

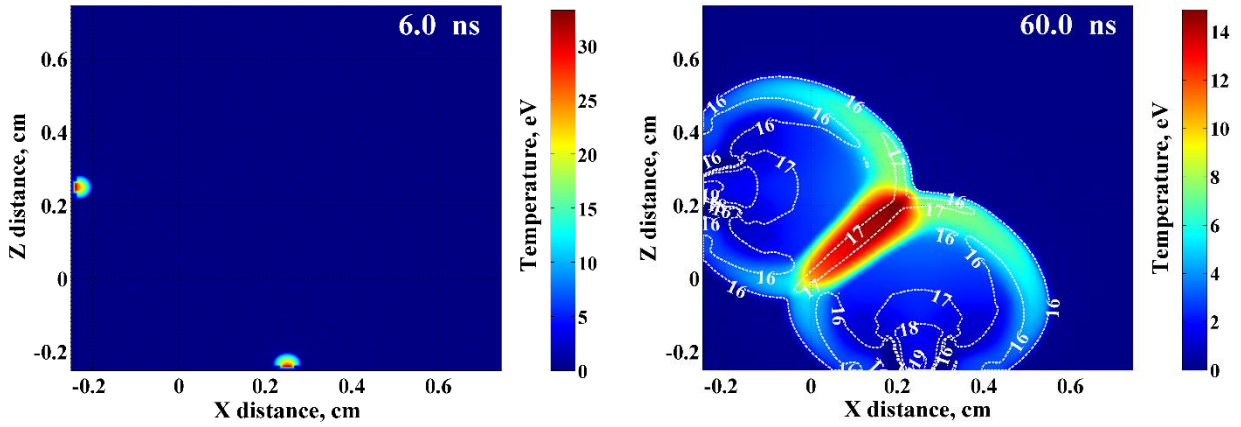

Figure 3.10 Plasma temperature and density (a) during the pulse and (b) at 60 ns after the pulse beginning.

Three-dimensional modeling allowed a detailed analysis of the developed plasma plumes and stagnation layer, spatial and temporal distribution of plasma parameters, and species. Figure 3.10(a) shows that the laser beam with energy of 150 mJ, duration of 6 ns (FWHM), and a spot size of 500 μm creates the plasma from graphite with a maximum temperature of around 35 eV at the peak of laser pulse intensity. Energy redistribution by collisions of plasma species in the expanding plumes and by radiation transport result in the temperature decrease to ~10 eV before the seed plumes contact. Subsequently, hydrodynamic pressure driving the two plumes leads to increased particle collisions at the intersection of two plasma fronts, resulting in an increase in temperature in the developing stagnation layer [Figure 3.10(b)].

3.5.1 Ion Distributions

Plasma species distributions at the initial interpenetration of two plasmas showed prevailing concentrations of C^{2+} - C^{4+} ions in the stagnation layer and in the plasma front layers [Figure 3.11(a)]. Only the near surface area with a high concentration of neutrals can be the source for carbon molecule formation at this time [Figure 3.11(b)]. C^{2+} - C^{4+} ions were found in the core of the stagnation layer up to 350 ns, corresponding approximately to the confinement time of this plasma layer.

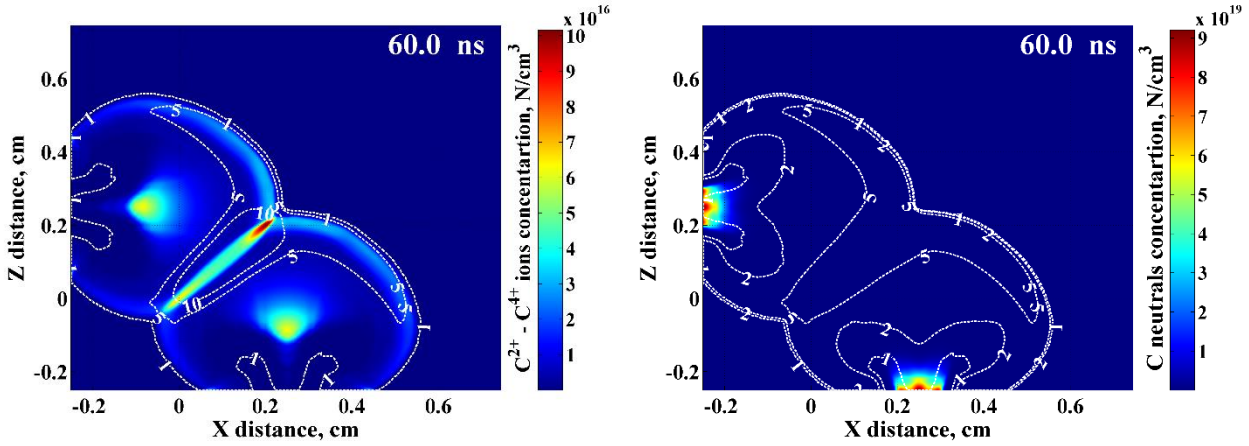

Figure 3.11 Plasma species distribution at the beginning of colliding two plumes: (a) C^{2+}-C^{4+} ion concentration and (b) C neutral concentration. White contours show electron temperature.

Experimental results showed that the initiation of C_2 molecule formation in the area of the stagnation layer corresponds to the time of ~250 ns after laser pulse for the considered laser parameters and ambient conditions. Continual expansion of original plasma plumes and plasma species recombination lead to the increased concentration of neutrals surrounding the stagnation layer at this time. However, relatively high pressure of the expanding plumes prevents fast

cooling of the core of the stagnation layer that leads to the prevailing concentration of carbon ions (mostly C^{1+}) in this area. These conditions continue for a relatively long time, around hundred nanoseconds, without significantly changing the stagnation layer properties (Figure 3.4 and Figure 3.12).

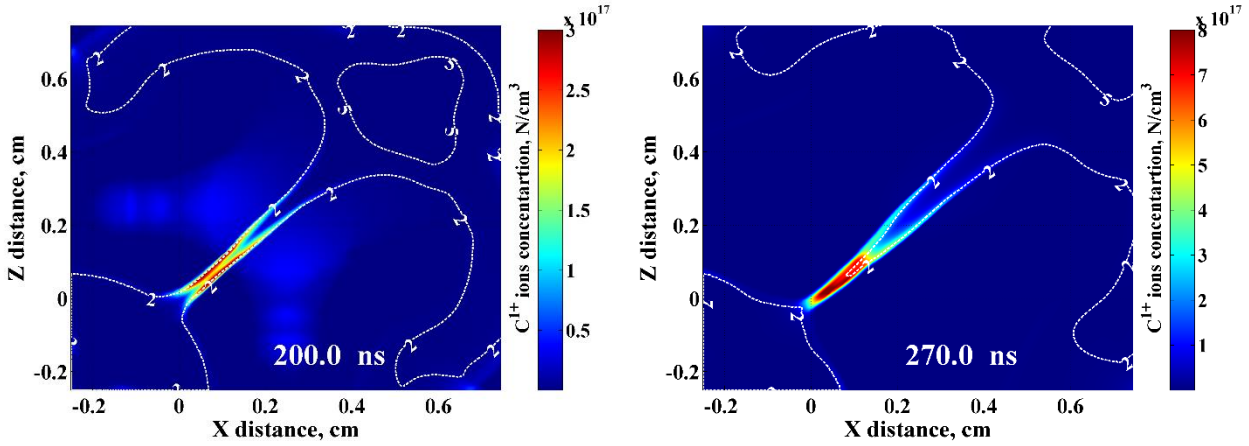

Figure 3.12 Cross-section of the C^{1+} ion concentration at different times. White contours show electron temperature.

Modeling of colliding plasma experiments provides a good opportunity to test integrated models comparing plasma dynamics and species distributions for a wide span of plasma/particle interactions. Given in Figure 3.4 and Figure 3.12 are the results showing the long-term existence of C^{1+} ions in the stagnation layer predicted in modeling and in spectroscopic images of C^{1+} ions emission at a wavelength of 656 nm.

The temporal evolution of the stagnation layer properties and neutral accumulation can be described by plasma hydrodynamics with incorporated mechanisms of electron thermal energy distribution and plasma species ionization/recombination. Initially, expanding plumes create a dense layer at the intersection with temperature higher than in the surrounding plasma. This

layer lasts for a relatively long time due to continued pressure being applied from the original plumes [Figure 3.13(a)]. When radiative cooling and plume expansion processes reduce significantly the seed plasma pressure, high pressure in the core of the stagnation layer initiates the expansion of the stagnation layer [Figure 3.13(b)]. Energy redistribution in the rarefied layer leads to a significant reduction of plasma temperature that finally leads to the prevailing neutral concentration and preferred temperature for carbon molecule formation.

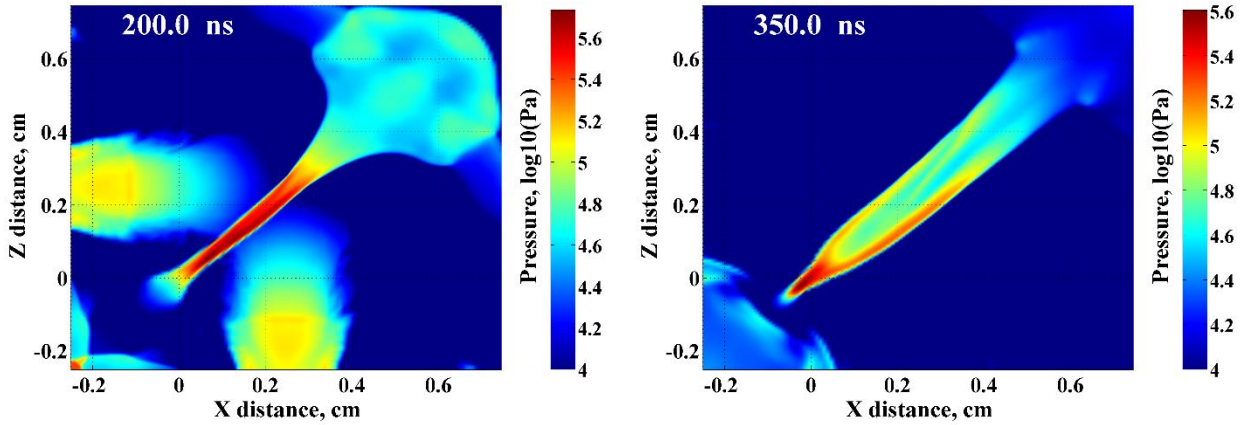

Figure 3.13 Pressure distribution (a) during the stagnation stage and (b) during the expansion of the stagnation layer.

A comparison of plasma temperature distribution at 500 ns and 750 ns (Figure 3.14) with Swan emission intensity found in the experiments (Figure 3.5) permits the indication of favorable conditions for carbon molecule formation and persistence within the plasma lifetime. These conditions describe regions with a relatively high concentration of carbon neutrals and with plasma temperatures between 0.7 and 1.1 eV. At earlier time, 500 ns, the high intensity of Swan emission is found close to the bottom edge of the stagnating plasma column due to relatively high plasma temperatures in the top area [Figure 3.5 and Figure 3.14(a)]. Further

expansion and cooling of the stagnation layer lead to larger area with optimum conditions for a high reaction rate [Figure 3.5 and Figure 3.14 (b)].

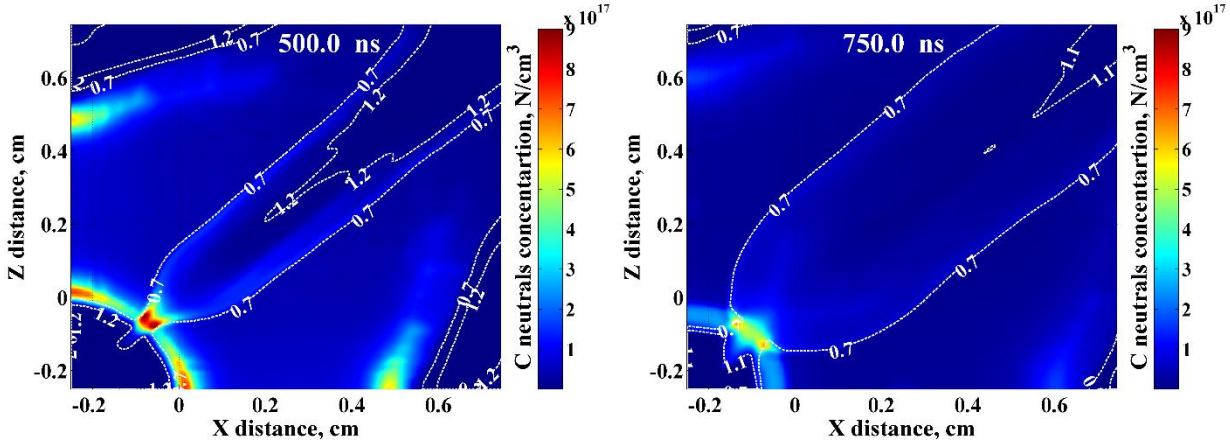

Figure 3.14 Cross-section of carbon neutral accumulation in the stagnation layer at (a) 500 ns and (b) 750 ns. White contours show plasma temperature.

The above analysis showed that stagnation layer evolution and properties can be determined by the interplay of two processes: (1) stagnation layer expansion due to high pressure in the core of this layer and (2) pressure from two seed plasma plumes due to continuous expansion of these plasmas. The higher energy accumulated in the stagnation layer in the case of more intense lasers leads to faster expansion and rarefaction of the colliding plasma layer that reduces the neutral concentration in the area with optimum temperatures for molecule formation and persistence.

A slight temperature increase at the intersection of two plumes occurs also for less energetic plasma flows created by lasers with intensities two times less than those considered above [Figure 3.15(a)]. However, much less energy is accumulated in thin intersection layer due to lower pressures of seed plumes. Such conditions lead to slower expansion of the stagnation

layer created by less energetic plasmas. Thus, the combination of two phenomena, lower energy in the stagnation layer in the case of less intense lasers and continuing supply of neutrals from the expanding seed plumes, prevents fast rarefaction of this layer that results in a high neutral concentration in the areas with optimum plasma temperatures for carbon macromolecule formation. Figure 3.15(b) illustrates the uniformity of conditions in the stagnation layer in the case of less intense lasers, showing pressure distribution at the stage of layer expansion.

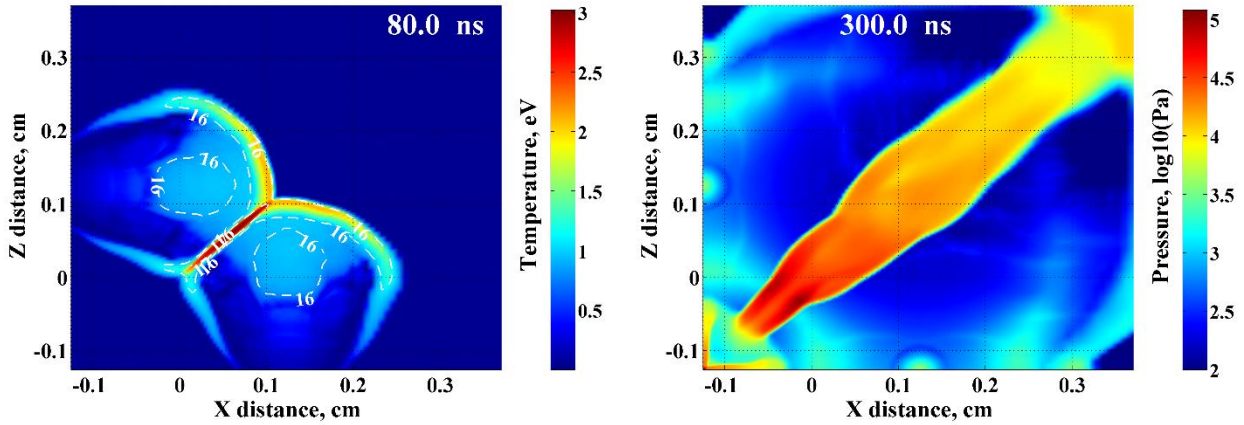

Figure 3.15 Evolution of the colliding plasma created by lasers with 6×10^{10} W/cm^2, 6 ns (FWHM) duration, and 200 μm spot size: (a) temperature increases at the intersection and (b) pressure distribution during stagnation layer expansion.

The maximum plasma temperatures in the stagnation layer varied from ~2.5 eV at 400 ns to 1.2 eV at 700 ns (in the case of 1.3×10^{10} W/cm^2 laser intensity). Other researchers showed similar slow cooling of the stagnation plasma for approximately the same laser parameters [36]. While experimental results predicted temperatures along the longitudinal distance averaging this parameter along the lateral distance, our modeling results enabled the prediction of the 3D temperature distribution in the entire layer. A comparison of modeling results with the previous experiments mentioned above and with our current experimental results regarding time-resolved

ion emission images gives us confidence in the correctness of used methods for the modeling of colliding plasma experiments. Theoretical validation for the hydrodynamical description of such a plasma arises from the relatively high Mach numbers of the considered flows [37].

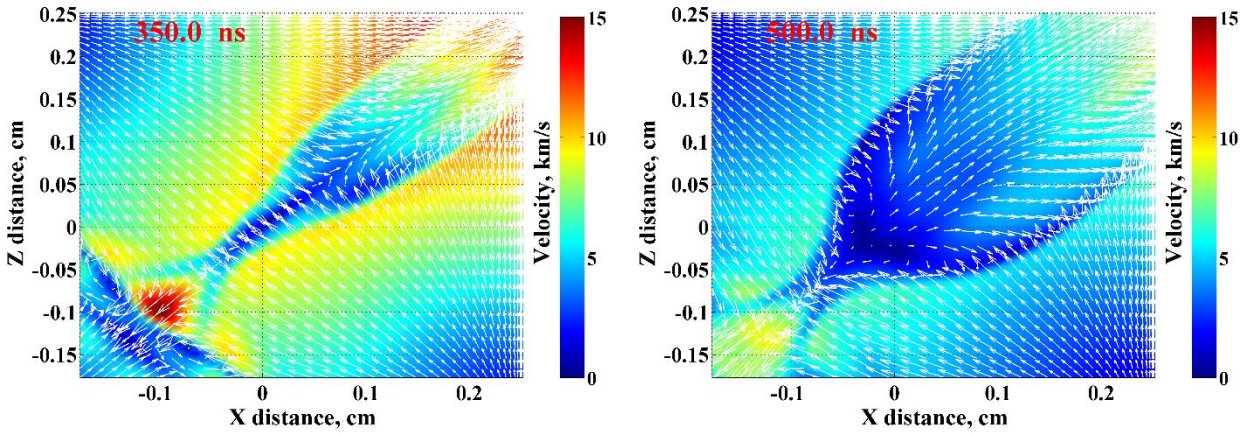

Figure 3.16 Velocity magnitudes and directions in colliding plasmas created by a laser with a spot of 500 μm.

Modeling results were used for a further analysis of the conditions at the location of high Swan intensity during the period of increase in the emission intensity (Figure 3.16). Changes in the velocity directions show that an increase in the C_2 concentration during the time from 350 ns to 500 ns is most likely due to increase in the formation rate at this particular location rather than drift from other areas. Future experiments supported by modeling will be conducted to provide details of carbon dimers and higher structure formation in the entire stagnation plasma layer. Based on the above analysis, preferable conditions for C_2 formation in LPPs can be described as a high neutral concentration along with relatively high, 0.7-1.0 eV, electron temperatures, confined in the volume not surrounded by hot plasmas, and lasting for a long, hundreds of nanoseconds, time. Such conditions can be created by multiple beams with relatively large spot

sizes, having, however, enough intensity to create and confine the colliding layer that can also be controlled by the setup geometry. Thus, the development of optimum colliding LPPs for the synthesis process depends on the interplay of several parameters, e.g., laser intensity which determines the amount of the evaporated material and seed and colliding plasmas velocities, laser spot size which determines collision dynamics along the stagnation layer, and ambient conditions and setup geometry which affect plasma confinement.

3.6 Conclusions

The collision between two colliding laser-produced plasmas features the formation of a stagnation layer produced by the accumulation of ablated material from each laser-produced plasma plume. The onset and development of the stagnation layer was affected by the selection of laser parameters with harder stagnation being observed upon using less laser intensity. The spatiotemporal evolution of the stagnation layer is strongly influenced by the spatiotemporal expansion mechanics of the seed plasma. Specifically, higher laser intensity causes greater laser-plasma interaction resulting in quick rarefaction of the seed plasma before a stagnation layer can be established.

The enhancement in C_2 synthesis in stagnation layer has been attributed to increased dimerization. This onset was synchronous with the merging of the two carbon neutral populations produced individually from each seed plume. Seed plumes should be produced such that their spatiotemporal development favors the formation of a sustained stagnation layer while also offering continual supply of carbon neutrals. The development of optimum colliding LPPs for the synthesis process depends on the interplay of several parameters, e.g., laser intensity

which determines the amount of the evaporated material, seed and colliding plasmas velocities, laser spot size which determines collision dynamics along the stagnation layer, and ambient conditions and setup geometry which affect plasma confinement.

4. SPECTROCHEMISTRY OF THE DEVELOP STAGNATION LAYER OF COLLIDING CARBON PLASMAS[2]

This chapter will expand upon concepts presented in the previous chapter, exploring the development of the stagnation layer of colliding carbon plasmas at times much later than the initial formation. Interest will be placed in discovering whether the collision of the two plasmas influences intermediate-time (1-10 μs) concentrations of transient molecular species C_2 and C_3. Laser-induced fluorescence (LIF) and optical time-of-flight (OTOF) are used to study these scenarios. The findings revealed from colliding plasmas will be discussed in context with single plasma results which will serve as a control experiment.

4.1 Introduction

Understanding the persisting behavior of carbon plasmas is of great interest in several disciplines. In chemistry, knowing how plasmas behave in the intermediate-to-late-time of a laser-produced carbon plasma offers an understanding of how small transient carbon dimers and trimers amass, chain together, and ultimately construct large macromolecules such as carbon nanotubes. In physics, knowing how these fullerene precursors aggregate is important in discerning chamber conditions unfavorable for high rep-rate operation. Various carbon macromolecules would be favored or disfavored depending on where they present. A better understanding of fundamental processes in their formation can enable engineering solutions to suppress their deleterious creation.

[2] J.P. Oliver, N. Bharadwaj, and T.S. Sizyuk, "Laser-induced fluorescence of C_2 and C_3 in colliding carbon plasma." Journal of Applied Physics, (under review).

Laser-produced plasmas typically undergo recombination reactions at late times ($\gtrapprox$ 1μs) when the plasma temperature is thermodynamically favorable. If plasma species are still in sufficiently high concentrations, three-body recombination processes may succeed one another to form larger and larger compounds. The most common means of attaining sufficiently high concentrations of plasma species at late times is by imposing spatial confinement of the expanding plume using a gas buffer. Alternatively, colliding plasmas may mutually impose confining pressures upon each other, even if they are in high vacuum. In an inertial fusion chamber, colliding plasma regimes are inevitable.

In this chapter, the intermediate-time (1-10 μs) formation of C_2 and C_3 transient molecular species will be explored in colliding carbon plasmas. Laser-induced fluorescence has been used to study these plasmas for carbon plasma in vacuum. Here, LIF techniques are carried out to image these species in the rarefied stagnation layer following plasma collision. Optical time-of-flight offers corroborative results in describing the spatial and temporal evolution of the stagnation layer.

4.2 Experimental Setup

In this set of experiments, a similar setup was used as was described in Chapter 3. A wedge formed by two graphite surfaces was placed inside a vacuum chamber which was pumped down to a 10^{-5} Torr vacuum. Two seed plumes were created from the laser-produced plasma of the graphite surface and were positioned in proximity such that they would collide. Ablation of the graphite was achieved using a Continuum Surelite III Nd:YAG laser. A 300 mJ pulse energy

output from the Nd:YAG laser was split using an ensemble of waveplates and polarizer cubes into two individual pulse arms each bearing 150 mJ.

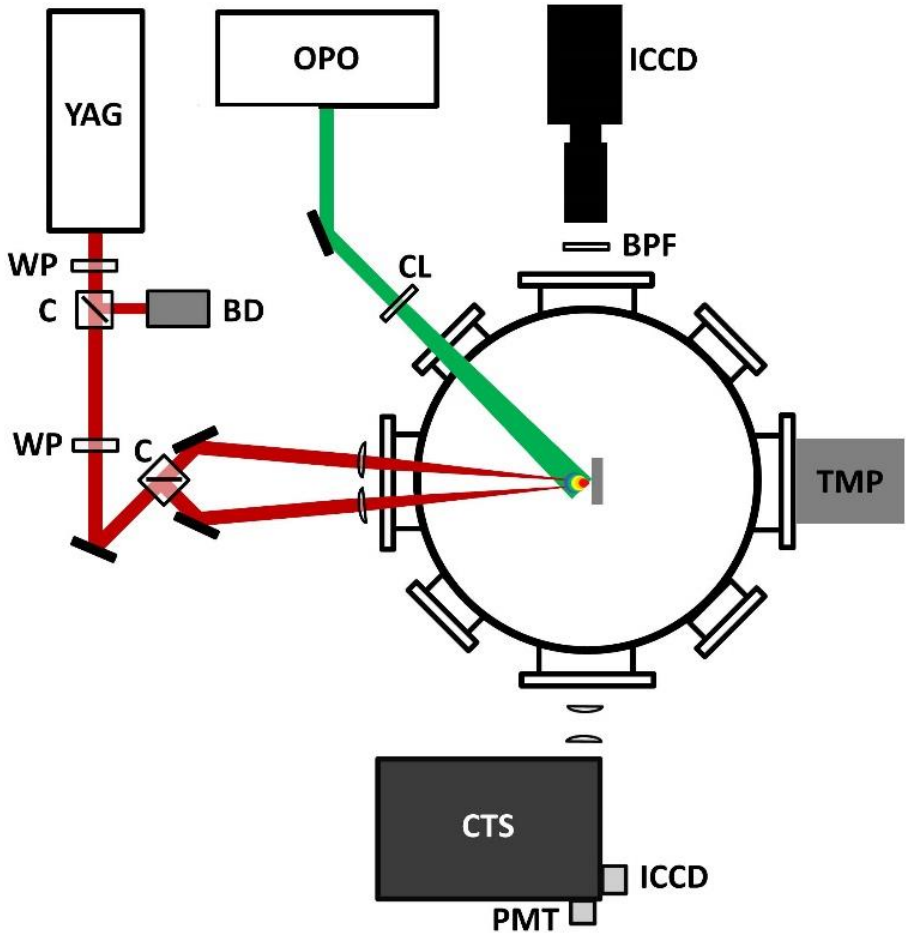

Figure 4.1 Experimental setup used in the study of colliding laser-produced carbon plasmas. Instrumentation used: Nd:YAG laser (YAG), tunable optical-parametric oscillator laser (OPO), Czerny-Turner spectrograph (CTS), intensified charge-coupled device (ICCD), turbomolecular pump (TMP), photomultiplier tube (PMT), bandpass filter (BPF), waveplate (WP), cube polarizer (C), beam dump (BD), and convex lens (CL).

Laser-induced fluorescence was accomplished using an Opotek RADIANT HE 355 LD tunable laser. The signal from the optical parametric oscillator (OPO) cavity was used as a probe

beam to excite C_2 and C_3 species in the plasma. To improve fluence uniformity, the probe beam was spatially cropped using an iris. The transmitted portion then passed through a 10 cm concave lens to increase the areal exposure of the probe beam onto the expanding plume. The probed plasma was located in the far-field sufficiently distant from the lens such that beam divergence was minimal across the plume dimension. Fluorescence was collected for 100 ns immediately following the probe laser pulse. The probe beam intercepted the expanding plume at a 45°. Probe beam parameters for the two excitation/fluorescence pairs are summarized below in Table 4.1.

Table 4.1 Laser-induced Fluorescence Parameters

SPECIES	EXCITATION	FLUORESCENCE	FLUENCE
C_2	516.6 nm	560 nm	0.4 mJ cm^{-2}
C_3	410 nm	400 nm	0.3 mJ cm^{-2}

Optical time-of-flight (OTOF) was additionally used to study the dynamics of carbon species in the plasma. This was accomplished using a photomultiplier tube (PMT, Hamamatsu R298) attached to an exit port of a Czerny-Turner type monochromator (Acton SP-2500, Princeton Instruments) with an 1800 grooves/mm grating. A bias voltage of ~1150 V was applied. A Faraday cup (Kimball Physics FC-71A) with -26V bias was used to measure ion time-of-flight (TOF). Both devices were connected to 1GHz digital oscilloscope (Agilent D8104) which was used to render files for the output signals and to monitor the timing of the lasers and other electronics. Timing settings were set using two synced programmable timing generators (Quantum Composers 9600+). The first PTG was used to continually flash the Nd:YAG and tunable lasers while the second was used to trigger Q-switching and plasma diagnostic electronics.

4.3 Laser-induced Fluorescence

Optical emission plume imaging offers a useful tool to observe plasma behavior when there is an abundance of excited species in the plasma. At later times in the plasma development, when species exist largely in their respective ground states, radiative emissions cease providing contour information about the various populations of species. However, this does not necessarily indicate that those species are not present. Using laser-induced fluorescence (LIF), populations of transient molecules C_2 and C_3 were qualitatively evaluated during the plasma lifetime exceeding 1 μs.

In LIF, a probe laser interacts with the plasma following some duration during which the plasma is permitted to develop. By prescriptively selecting the wavelength of the (tunable) probe laser beam, the selected species will discriminately fluoresce. In order to observe C_2 populations, a 516 nm excitation was chosen with fluorescence of the (0-1) Swan band observed near 563 nm. Alternatively, a 410 nm probe wavelength was chosen to observe C_3. 405 nm excitation of C_3 is ideal, but the lowest setting of our tunable OPO laser is 410 nm though this will be shown to be adequate. Sample excitation spectra are shown in Figure 4.2. In Figure 4.2(a), the rotational modes near 562 nm are more pronounced because their corresponding modes in the higher vibrational state reside within the optical bandwidth of the 516 nm excitation laser. By finely tuning the excitation wavelength, the optimal excitation wavelength can be determined which maximizes optical transmittance through the bandpass filter chosen for monochromatic imaging. In Figure 4.2(b), the C_3 Swing bands are observed appearing a semi-continuum spectrum peaking at 405 nm. The sharp peak seen at 410 nm is inherent due to the

resonant excitation by the tunable OPO laser. Both spectra were only minimally apparent without LIF excitation for the evaluated delay time.

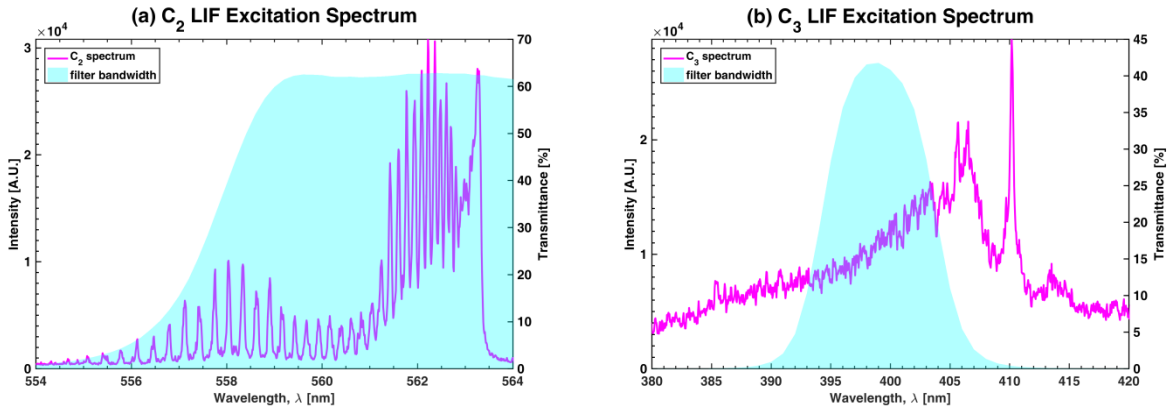

Figure 4.2 Sample excited spectra (magenta) of (a) (0-1) C_2 Swan band and (b) C_3 Swing bands using 516 nm and 410 nm excitation wavelengths respectively. Spectra were taken over 2 and 10 μs gated exposure respectively. Cyan overlays show the optical bandwidth (nominal 10 nm FWHM) of chosen bandpass filters used in LIF imaging.

4.3.1 LIF Imaging

Laser-induced fluorescence images for the colliding carbon plasma scheme are shown for C_2 and C_3 species respectively in 10^{-6} Torr vacuum in Figure 4.3 and Figure 4.4. The early time behavior preceding the first microsecond of development entails the onset of stagnation and has been shown in previous experiments [16]. LIF imaging of an individual seed plasma was also conducted for control comparison. This enables discernment of processes occurring prior to plasma collision and will also help us identify which processes are intrinsic to the colliding plasma scheme. The imaging procedure was conducted as described in the previous section. Five accumulations were taken for each time frame to minimize the effect of potential shot-to-shot variance of the tunable laser energy while also capturing crisper images from collecting

more light. A logarithmic color scaling is implemented to allow simultaneous observation of the stagnation layer and the outer expansion dynamics of the plasma.

4.3.1.1 C_2 Carbon Dimers – Colliding Plasma

Figure 4.3 shows the distribution of transient C_2 molecules over the course of 5 μs. Initially, the C_2 rich region is highly localized along the collision midplane. Soon thereafter, C_2 covers a larger space following the transition occurring at around 2 μs. We attribute the initially high concentration to enhanced dimerization – the process wherein C_2 is synthesized via the recombination of neutral atomic carbon – around the stagnation layer. The reaction rate of this process is bimolecular with association to carbon neutrals and is thus expected to increase approximately quadratically with the local C density. The stagnation midplane of colliding plasma offers favorable conditions for dimerization during the interval in which carbon neutrals coincide. Higher plasma temperature along the stagnation layer should also increase emission through enhanced collisional excitation.

After 1 μs, the lateral confinement imposed upon the stagnation layer by pressure exerted from the seed plasma relaxes, and the stagnation layer simultaneously begins losing (i) density/collisionality and (ii) influx of carbon neutrals. Consequently, the rate of dimerization slows, gradually lessening the C_2 in the now-rarefied stagnation layer plasma.

By 2.5 μs, the stagnation layer has fully transitioned from its initial well-defined form with sharp pressure boundaries into a homogenous, nebulous plume. The ensuing development of the stagnation layer only results in further rarefaction of the plume. Continued consumption of C_2 dimers results in the production of increasingly larger carbon compounds. The population of C_2 at any particular moment in the plume development is regulated by the competition

between production and consumption (i.e. dimerization and molecular recombination). At any particular moment, it cannot be definitively determined whether C_2 levels are attributed to slow-production–slow-consumption or to fast-production–fast-consumption. We believe production effectively ends by 2 μs due to a lesser abundance and concentration of carbon neutrals. The ensuing depletion of C_2 thus reflects the rate of C_2 consumption in forming larger and larger carbon molecules.

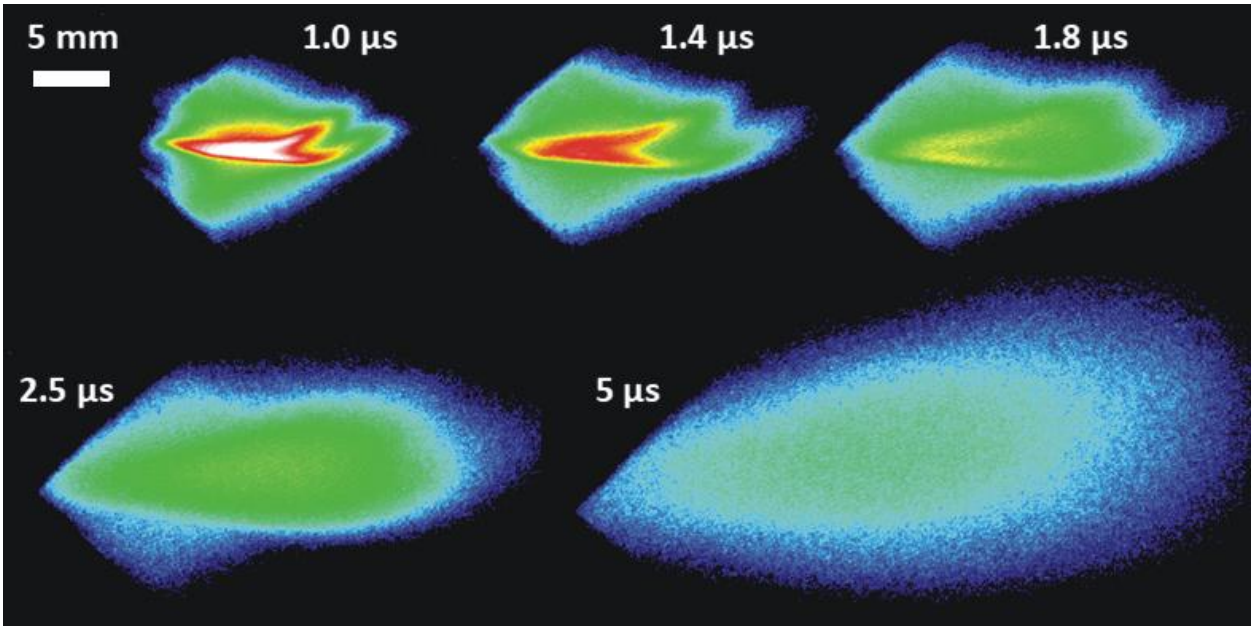

Figure 4.3 Laser-induced fluorescence images of C2 populations from colliding carbon plasma in a 10^{-6} Torr vacuum. LIF was performed using a 517 nm excitation wavelength with discriminant observation around 560 nm through a select bandpass filter.

4.3.1.2 C_3 Carbon Trimers – Colliding Plasma

Triatomic carbon, C_3, is the next largest carbon molecule present in homonuclear carbon plasma. In gathering an understanding of large carbon allotrope synthesis, LIF imaging C_3

naturally succeeds C_2 LIF. In spectroscopic studies, Swan band emissions are very evident in C_2-abundant carbon plasma. While not generally as pronounced, pseudocontinuum Swing bands belonging to C_3 transitions ($A^1\Pi_u \leftrightarrow X^1\Pi_g^+$) may be observed with the aid of LIF. Due to the more intricate spectrum of C_3, the fine differences between individual rovibrational bands are not readily resolved (as is clearly possible for C_2 Swan spectra, see Figure 4.2) [27,28]. This gives the spectrum the false appearance of being noisy.

C_3 LIF imaging was performed for colliding carbon plasma in 10^{-6} Torr (Figure 4.4). Seen here as early as 1 μs, C_3 occupies the entire domain enclosed by the two graphite surfaces. This behavior distinguishes C_3 from that previously observed in Figure 4.3 where C_2 dimers were highly localized along the collision midplane. Certainly, the stagnation region is more brilliant, but this could easily be attributed to enhanced collisional excitation and to the accumulation of transiting C_3 as it blocked by the stagnation layer. The fact that C_3 engrosses the space near the graphite surface suggests that that C_3 is directly produced from laser ablation rather than solely upon processes occurring in the stagnation layer.

While C_3 is produced in part ab-initio from laser ablation, it remains present for several microseconds thereafter suggesting that a balance of gain and loss mechanisms maintain a steady population. A similar three-body recombination mechanism to C_2 dimerization is undertaken to synthesize C_3:

$$C_2 + C + M \rightarrow C_3 + M$$

where M is some third body participating in momentum transfer. This three-body recombination process is rate-determined by prevailing concentrations of C_2 and carbon neutrals. It follows that C_3 produced in this fashion would lag C_2 dimerization. Couple this hypothesis with the previous knowledge that C_3 is produced ab initio from the laser ablation and we form a picture of how C_3

levels could remain relatively constant across multiple developmental stages of the colliding plasma. C_3 would ultimately be exhausted from the plasma as it is consumed synthesizing larger carbon clusters. Alternatively, C_3 could simply be nonreactive following initial formation. Inquiry into the prevailing nature of C_3 in the standalone expansion of singular seed plasma will equip us with the insights needed to make this distinction.

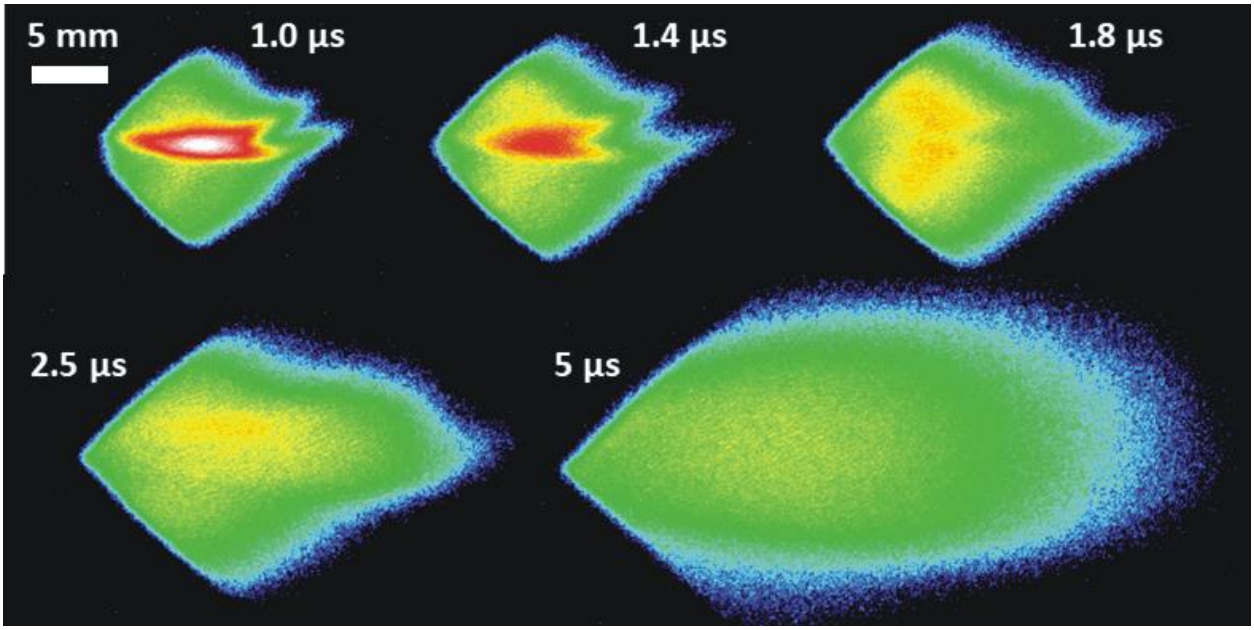

Figure 4.4 Laser-induced fluorescence images of C_3 populations from colliding carbon plasma in a 10^{-6} Torr vacuum. LIF was performed using a 410 nm excitation wavelength with discriminant observation around 400 nm through a select bandpass filter.

4.3.1.3 Single LPP of Carbon

LIF imaging was performed for an individual carbon laser-produced plasma at 10^{-6} Torr. Figure 4.5 shows LIF excitation for (a) C_2 and (b) C_3 respectively using the same LIF excitation scheme introduced earlier. It is useful to study the plume development of an individual carbon laser-produce plasma. In this way, we gather two important pieces of information regarding seed

plasma: (i) which molecules form prior to collision and (ii) how long do they remain present over plasma lifetime. To ensure the best comparison, we recall the same total laser pulse energy (300 mJ) and intensity (8×10^8 W/cm^2) as were used in colliding plasma study (spot size was adjusted accordingly). Carbon laser-produced plasma was generated from a planar graphite surface.

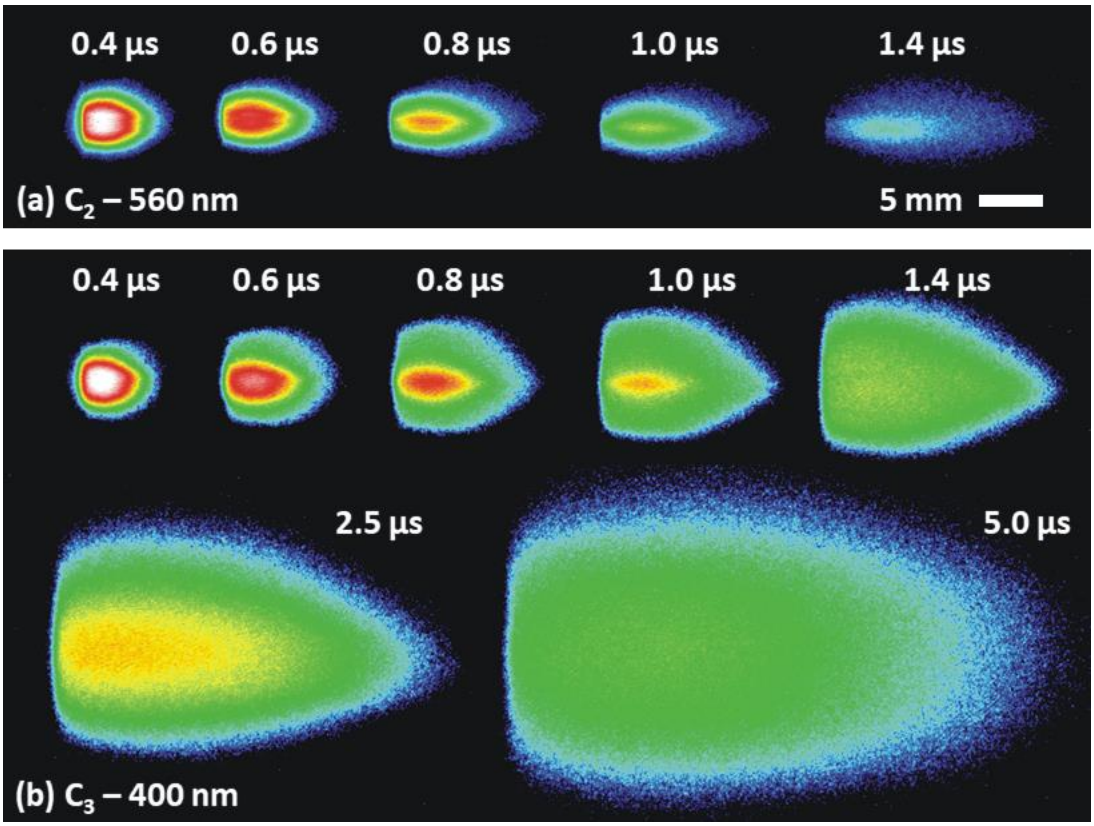

Figure 4.5 Laser-induced fluorescence images of (a) C_2 and (b) C_3 populations in the single plume expansion of carbon laser-produced plasma in a 10^{-6} Torr vacuum. LIF was performed using a 410 nm and 517 nm excitation wavelengths for C_2 and C_3 respectively.

Figure 4.5(a) portrays LIF imaging for C_2 dimers in a single plasma. The color scaling of the image here is equal to that featured earlier in Figure 4.3 for colliding plasma, making absolute comparison between the two appropriate (this likewise applies for C_3 upon comparing

Figure 4.4 and Figure 4.5(b)). From Figure 4.5(a), we observe that the C_2 is only present within the first 1 μs or so. Thereafter, we presume that existing C_2 is consumed in synthesizing larger carbon structures. Without inducing a high concentration of carbon neutrals, C_2 populations may not be replenished. Following 1.4 μs, C_2 is nearly absent from the plasma.

The results of C_3 LIF show differing behavior of C_3 from C_2. Over the course of microseconds, the plume expands beyond its ablation site origin without indication of depletion. Knowing that C_3 is synthesized from C_2, it should be inferred that C_3 is largely unreactive (since we just saw that C_2 is largely absent). At this time, the plasma is too cool to favor dissociative processes which might further introduce C_3. Our conclusion is that C_3 is produced ab initio in great abundance during the course of the laser pulse (and shortly thereafter) due to extensive dissociation of large carbon molecules initially liberated from the surface. C_3 continues to linger in the plasma thereafter.

A further observation suggesting C_3 is relatively unreactive is the remarkable similarity in plume development at 2.5 μs and 5 μs time steps for both single and colliding plasma. It appears the plasma collision had only marginal effect besides perhaps collisional excitation along the collision midplane. Ultimately, C_3 trimers will still react but over a longer timescale then presently considered. The key observation is that C_2 production is massively enhanced in a vacuum environment by implementing a colliding plasma scheme.

4.4 Optical Time-of-flight

Optical time-of-flight data provides complementary information to LIF imaging, especially since it may be used to observe elusive carbon neutrals, C(I). Carbon neutrals

command interest in this investigation due to their central role in C_2 dimerization. LIF imaging C(I) would be ideal, but this isn't realizable due to sparse visible emissions from C(I). Fortunately, ultraviolet emissions are readily observed by our OTOF apparatus, allowing us to record emission of the 247.9 nm line of C(I). Carbon dimers were also observed using (0-0) Swan band emission at 516.5 nm. Space-time contours of C(I) and C_2 are shown in Figure 4.6.

The space-time contour of C(I) seen in Figure 4.6(a) reveals a few trends regarding carbon neutrals during plume development of the colliding plasma. Within 500 ns, the expansion of carbon neutrals is limited within 5 mm outbound from the seed plasmas. From 500 to 1000 ns, the stagnation layer cools, allowing carbon ions to undergo electron-ion recombination, manifesting neutral carbon farther out. This effect is observed as the bend in Figure 4.6(a).

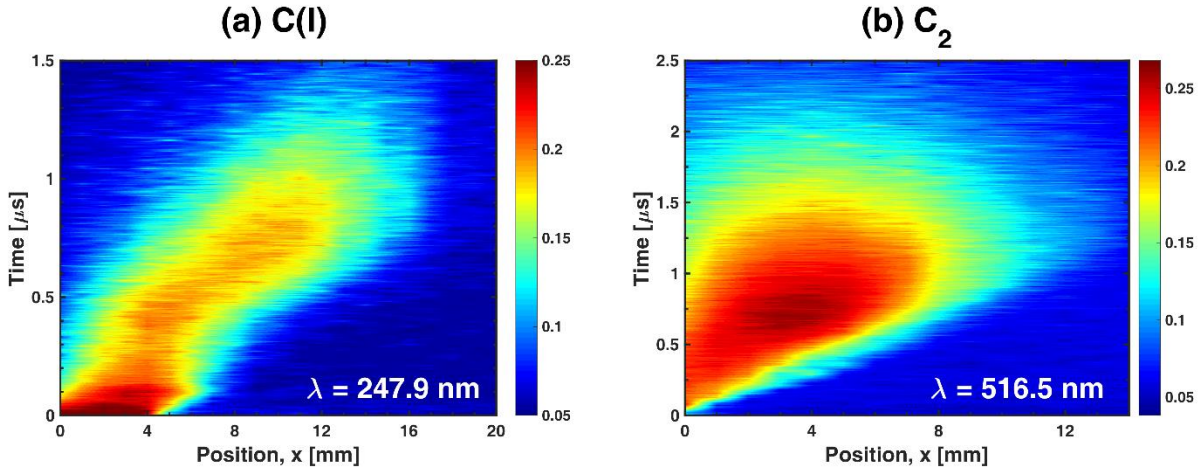

Figure 4.6 Space-time contour plots created from OTOF profiles taken from cross sections along the stagnation layer of the colliding plasma. At position x = 0 mm, the slit of the monochromator is aligned to observe the cross section containing both seed plasmas. Incremental increase in x observes cross sections farther outbound from the seed plasmas and graphite surfaces. OTOF space-time contours of (a) C(I) neutrals and (b) C_2 dimers are shown.

The creation of C_2 in the stagnation layer may be observed in Figure 4.6(b). The C_2 space-time contour is immediately distinguishable from that of C(I) regarding the first onset of emission. For C(I), emission was immediately observed a t = 0 over a 4-mm range, suggesting neutral source from seed plumes. Conversely, the onset of C_2 emission experienced a small yet discernable delay. Moreover, peak Swan band emissions aren't realized until ~750 ns. This behavior strongly suggests that C_2 is formed later in the plasma through a formation process (i.e. dimerization). The reach of C_2 ultimately extends only 12 mm, an observation aggregable with LIF imaging (Figure 4.3).

Individually, space-time OTOF contours of C(I) and C_2 offer information but are more useful through mutual comparison in this context. It has been mentioned that C_2 is principally produced in colliding carbon plasma through dimerization in the stagnation layer. In this process, carbon neutrals mutually undergo collisions in the presence of a third body to produce C_2. As such, it is expected that C_2 populations emerge at places and times within the plasma possessing an abundance of carbon neutrals. We recall that C_2 peaks at 750 ns at a distance of 4 mm. At this time and place, C(I) populations are certainly present though they are more abundantly distributed farther out. It is essential that the C(I) populations reach areas before C_2 is observed there since C(I) is understood to be its precursor. This is indeed the case, giving credence to our interpretation.

OTOF features high spatial resolution (equal to the 20 μm slit width) in X. However, transverse to X, emission is spatially integrated (over the 12 mm slit height). The dimerization rate is bimolecular with respect to C(I), making it sensitive to the local concentration. In colliding plasma, lateral pressure exerted upon the stagnation layer maintains confinement. In the present case, this ceases at around 500 ns. Thereafter, the stagnation layer relaxes, losing

peak concentration due to this lateral expansion. Appropriately, one should expect decremental C_2 production tied to decreasing C(I) population at later times in the plume development. Modeling of colliding carbon plasma will provide these and other complementary insights in the next section.

4.5 Ion Time-of-flight with Faraday Cup

The ion time-of-flight (TOF) signal of the colliding carbon plasma shows (Figure 4.7) the standard fast component associated with the emission of fast ions from the initial energetic plume expansion. In a colliding plasma regime, a portion of the fast ions encounter scattering collisions in the stagnation layer which reduces their energy. It can be seen in Figure 4.7 that the tail end of the fast peak features a long pedestal from 2 to 5 microseconds. This behavior is typical of colliding plasmas [38,39]. This change is attributed to the screening effect on ions interpenetrating through the opposing plasma, causing them to slow.

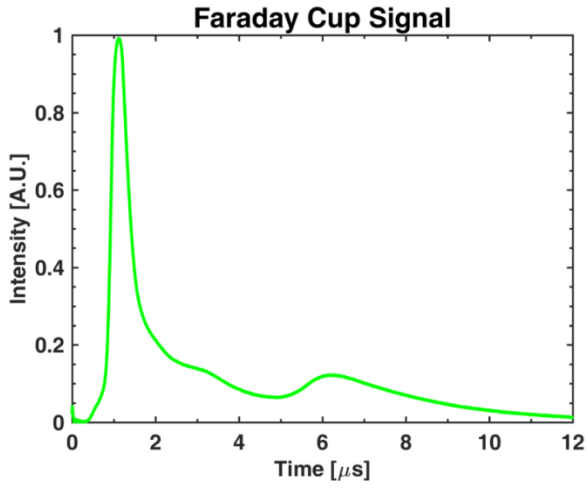

Figure 4.7 Ion time-of-flight signal of colliding C plasma collected using a Faraday cup (9 cm away, 20° from target normal) in 10^{-5} Torr vacuum.

4.6 Modeling

The effect of colliding plasmas properties on C_2 molecules formation was analyzed using 3D HEIGHTS models. In the present study, lasers with relatively low intensity of 4×10^9 W/cm^2 and 1 mm spot size were used to produce seed plumes. Collision of two plumes initiated at approximately 150 ns after the laser pulses and the maximum electron temperature in the stagnation layer was around 3 eV. Figure 4.8 shows simulation results of mass density and contours of electron density (logarithmic values) distribution in the entire domain at 250 ns, when the stagnation layer consisted mostly from carbon ions, and at 550 ns, when the concentration of neutrals was higher than ion concentration.

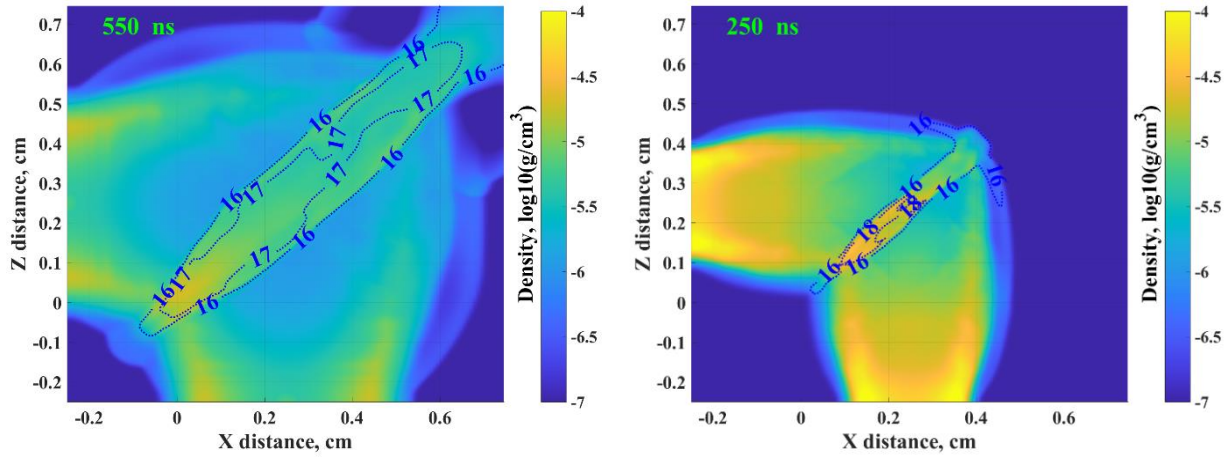

Figure 4.8 Mass density and electron density (contours of logarithmic values) in the stagnation layer at different times corresponding to low and high C_2 intensity detection.

Cooling of the stagnation layer to ~1 eV and increased concentration of neutrals can explain enhanced C_2 emission, detected at later time. Cooling mechanisms of colliding carbon plasmas include kinetic energy losses in expanding stagnation layer, escape of radiation energy

produced by electron-ion recombination, ions and atoms de-excitation and energy consumption by possible carbon molecule dissociation. The rates of atomic and molecular processes have strong dependence on the properties of the developed low temperature plasma. Figure 4.9(a) shows the difference in plasma emissivity due to electron-ion recombination and relaxation processes for the densities and temperatures relevant to plasma properties shown in Figure 4.8. Given in Figure 4.9(b) absorption probabilities show that significant part of emitted radiation in the case of warmer and denser plasma can be reabsorbed in the stagnation layer that delays cooling of this layer.

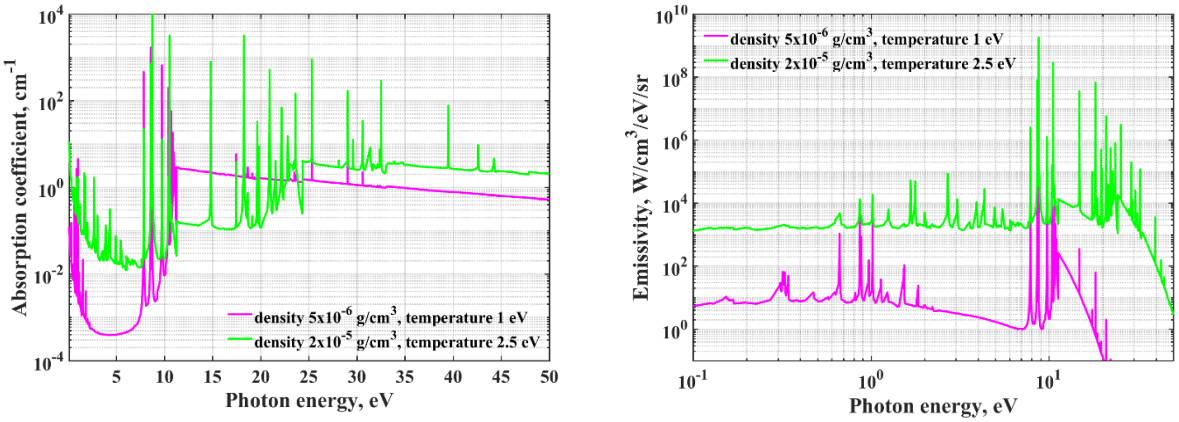

Figure 4.9 Effect of low temperature plasma parameters on emissivity (a) and photon absorption probability (b).

At earlier time, high density and temperature in the stagnation layer resulted in prevailing concentration of ions in this location, mostly C^+ and C^{2+}. Figure 4.10(a) shows neutrals density and contours of ions density distribution (logarithmic values) at 250 ns. The cooling mechanisms inside the stagnation layer at this time are governed by electron-ion recombination and relaxation processes. Further expansion and cooling of colliding plasma layer leads to increase of neutrals concentration in the area (Figure 4.10(b)) with temperatures around 1 eV.

Such unique species composition in the stagnation layer develops favorable conditions for carbon dimers formation. A comparison between Figure 4.6 and Figure 4.10 shows that significant enhancement of C_2 formation at later time is determined by the colliding plasma layer.

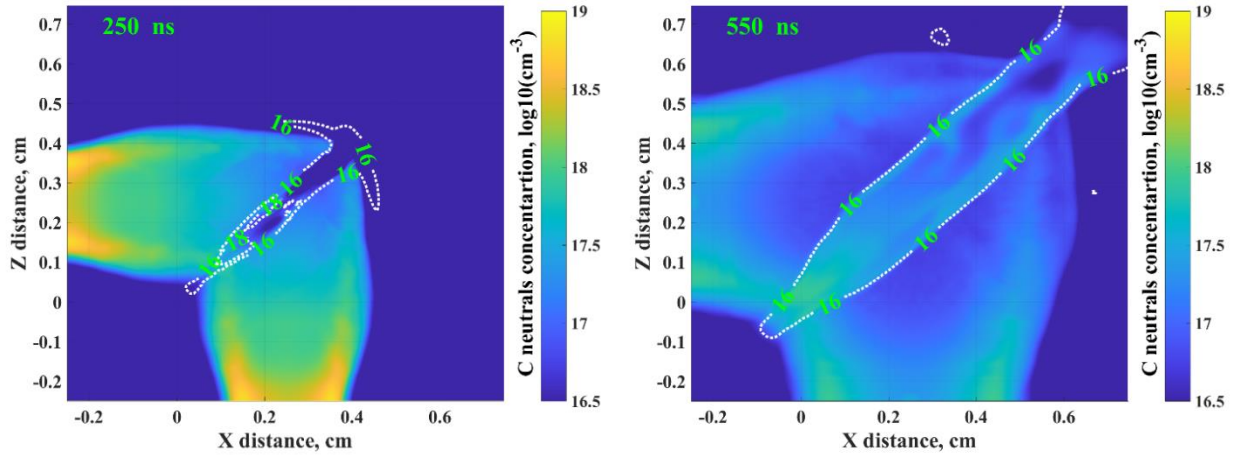

Figure 4.10 Neutrals and ions concentration (white contours of logarithmic values) in the colliding plasmas at different times corresponding to low and high C_2 intensity detection.

4.7 Discussion

At any given moment, several chemical processes simultaneously govern populations of C_2 and C_3 in carbon plasma. C_2 and C_3 populations are introduced by two general reactions: recombination and dissociation. The most important of these chemical processes are given in Table 4.2. With laser-produced plasma, dissociation is most prevalent in the nascent plasma when plasma temperature greatly exceeds the dissociation energy of many constituent species in the plasma. Within nanoseconds, electron impact and photo-absorption cause carbon clusters to deconstruct into basic molecules C_2 and C_3. Photo-dissociation of carbon clusters is greatly predicated on the photon wavelength as well as the intensity (giving rise to multiphoton

absorption) [40]. Following ablation, recombination accounts for C_2/C_3 production during the ensuing cooling of the developing laser-produced plasma.

It was revealed in the previous section that C_3 is produced ab initio during laser ablation and that, generally speaking, C_2 is not. Previous studies exploring the photo-dissociation of linear carbon clusters reveal that the most energetically favorable fragmentation channel is typically through dissociation into neutral C_3 and C_{n-3} [41]. This is conditionally true for visible and near-infrared laser wavelengths at low intensity. The dissociation energy of a C_2-producing fragmentation channel is usually around 6 eV. This fragmentation channel may become viable once either laser frequency matching or exceeding vacuum ultraviolet or multiphoton absorption becomes significant. Alternatively, C_2 may be produced from the dissociation of C_{60} which must be present [42,43].

Table 4.2 Chemical reaction channels important in laser-produced plasma of graphite

SPECIES	REACTION	TYPE
C_2	$C + C \rightarrow C_2$	recombination
	$h\nu + C_{60} \rightarrow C_{58} + C_2$	photodissociation
	$C_n \rightarrow C_{n-2} + C_2$	dissociation
C_3	$C + C_2 \rightarrow C_3$	recombination
	$h\nu + C_n \rightarrow C_{n-3} + C_3$	photodissociation

* Disfavored while $h\nu < E_{dis}$

Ultimately, the properties of the stagnation layer vary with different laser parameters and target geometries. Plume hydrodynamics determine the onset of colliding plasma stagnation – the continual expansion of seed plasma provides the initial pressure confinement necessary to

sustain accumulation of material in the stagnation layer. As this material is exhausted however, the colliding plasma may no longer be most effectively described by the juxtaposed interpenetration of the cross-propagating seed plasmas. By now, the large number of collision events in the stagnation layer has randomized (thermalized) the motion of constituent atoms and molecules. By inducing collisionality in this manner, chemical processes required for carbon allotrope formation are enabled even within a vacuum environment.

This shift from "colliding" plasma to "collisional" plasma suggests a change in the prevailing physics. The underlying physics of established collisional plasma should conceivably be less sensitive to particular experimental parameters (viz. target geometry, laser parameters) than it was at the initial collision. In this study, the transition of colliding plasma to collisional plasma occurs at around 1 μs and is completed by 2 μs. The exact moment of this transition is a bit arbitrary when attempting to generalize the observations. Experiments have shown colliding carbon plasma capable of producing single-wall carbon nanotubes (SWNT). These studies attribute growth of carbon nanotubes to enhanced dimerization within the stagnation region of colliding plasma setup. An abundant supply of C_2 has in turn been shown to facilitate CNT formation [44].

From the introduction, we recall that the chamber walls of an inertial fusion energy (IFE) reactor endure extreme conditions associated with intense photon and ion deposition following each target implosion. Evaporation of wall material is expected during normal operation and can contribute to chamber contamination. Replicating this exact erosion process proves a difficult feat in a lab setting. In IFE, the ablation of wall material occurs first from prompt photoemissions (namely x-rays but also gammas and scattered drive laser). After a few microseconds, the slow-moving ions reach the wall upon first bypassing material initially

removed from photon loading. An accurate depiction of the blowoff plasma from the first wall must (i) account for the ion component interaction with the preliminary x-ray-ablated plasma, and (ii) include the ensuing ablation from ion bombardment. The blowoff plasma from each succeeding target implosion could certainly disrupt carbon fullerene accumulation attained in the chamber during previous implosion cycles (which would concordantly improve chamber clearing). Dissociated fullerene debris might therefore occupy the chamber in a sort of steady-state manner. This all occurs while active chamber-clearing measures are enacted, further adding to the complexity.

While conditions explored in the present study differ from those expected in an IFE device, the results may still provide insight. Namely, the production of C_2 in vacuum is greatly enhanced by a colliding plasma scheme. Cross-propagating jets of carbon plasma encounter sufficiently numerous collisions to create a region of stagnation characterized by strong thermal behavior. An abundance of carbon neutrals caught in this region is therefore inclined to synthesize C_2 due to the high local collisionality. Ultimately, this finding suggests that during the radially inward collapse of carbon plasma towards the chamber center, the attendant self-interpenetration of the plasma will result in enhanced fullerene production, even under vacuum conditions. In practice, an IFE chamber will indeed possess a low-pressure inert gas ambient. For pressures exceeding about 0.1 to 1 Torr, the present study loses validity as pressure confinement now provides the necessary conditions for high carbon vapor density and collisionality. Future studies should also address the high IFE chamber temperature. An IFE device might expect a steady-state plasma temperature of 6000 K due to slow conductive cooling [45].

4.8 Conclusion

It is understood that short-lived carbon molecules C_2 and C_3 serve as building blocks which ultimately assemble into large carbon allotropes such as carbon nanotubes (CNT). This process is preferred in the presence of a low-pressure, inert gas ambient. For CNT synthesis to become prevalent in a vacuum environment, a high carbon vapor density with high collisionality must be attained. Conditions within the stagnation layer of colliding plasma satisfy this criterion. In this work, laser-induced fluorescence of C_2 and C_3 was performed on the stagnation layer of two colliding carbon plasmas. Results indicate that C_2 dimerization is greatly enhanced by the plasma collision due to the accumulation of carbon neutrals along the collision midplane. Conversely, C_3 was mostly produced ab initio during laser ablation and was largely unaffected by the plasma collision within the explored time domain.

Purposeful laser-oven methods for CNT production have already been identified [46,47]. The present discussion addresses deleterious CNT production within an inertial fusion energy (IFE) chamber. Vapor erosion from the graphite first wall may introduce large carbon macromolecules which reduce the shot-to-shot performance of target implosions. Equipped with an understanding of the carbon plasma chemistry, one may engineer chamber conditions which address this issue. Additional work should explore the continued carbon chaining into large carbon allotropes. This could be approached through in-situ laser-induced incandescence of the plasma and particle collections observed ex-situ with SEM/TEM.

5. COLLIDING TIN PLASMA AS AN EUV SOURCE FOR NEXT-GENERATION PHOTOLITHOGRAPHY

Emission from laser-produced Sn plasma is currently favored as an extreme ultraviolet (EUV) light source for next-generation photolithography. Development of this photon source requires maximizing the conversion efficiency of laser light into in-band EUV photons at high power while minimizing the ion debris produced in the plasma. Colliding plasmas offer an advantage in this respect because they can amass ablated material along the collision midplane. The stagnation layer of the colliding Sn plasmas exists as high-density plasma that could be optically pumped by another laser to efficiently generate EUV light. Such a dual-pulse colliding plasma scheme will be explored in this chapter.

5.1 Introduction

According to Moore's law, the number of transistors in a dense integrated circuit (IC) doubles approximately every two years [48]. Decreasing transistor feature sizes has been essential for the continuation of this trend since the 1970s [49]. The minimum feature size (or critical dimension, CD) can be reduced through decreasing the illumination wavelength or by increasing the numerical aperture (NA) of the imaging lens. Historically, UV lines from mercury gas-discharge lamps were used as a light source in photolithography. In the 1980s, the inception of excimer lasers in the photolithography industry enabled further decrease in feature size. Deep ultraviolet lithography (DUVL) using 193 nm light from ArF lasers made it possible to reach feature sizes 45 nm and below. Recently, immersion lithography has been used to increase NA to about 1.35 for even further improvement. However, as illumination wavelength decreases,

large numerical aperture imposes a limit to depth of focus (DOF) which in turn restricts the thickness of the photoresist.

The path forward for next-generation lithography (NGL) calls for an extreme ultraviolet (EUV) or soft X-ray light source with high brilliance and in-band spectral purity [50]. Since EUV light is readily absorbed in most matter, the optical path of the EUV light must be in vacuum or very low-pressure gas [51]. Furthermore, EUV light is absorbed by glass lenses, so all optical components must be mirrors. The availability of Mo/Si multilayer mirrors with ~70% reflectivity at normal incidence of light centered at 13.5 nm (good for this wavelength) indicates a natural choice for the targeted wavelength for NGL light sources [52]. Due to the large amount of transmittance losses of the EUV light as it navigates a set of mirrors that focus and navigate the beam from the light source chamber to the photoresist and stepper, less than 1% of the in-band EUV light is actually harnessed for photolithography. Therefore, a brilliant EUV light source is necessary to overcome this setback so that a high wafer throughput may be achieved to meet the exigent demands of high volume manufacturing (HVM).

Several considerations should be made for the design of a EUV light source. First, the EUV emission should possess high spectral purity so that a monochromatic source of light can be used in the photolithography process. This is important for attaining high etch resolution. Additionally, the EUV source should not produce large amount of atomic or particulate debris which would shorten the lifetime of collection optics [54,55,56]. It is generally known that surfaces with roughness on-the-order-of or greater than the wavelength of an incident photon tend to absorb or diffusely scatter that light. It is therefore understood that collection optics must be highly polished. As debris deposits on the surface, the mirror loses its optical smoothness and the EUV transmittance through the system suffers accordingly.

Over the years, several element candidates have been given prominent consideration as a EUV light source: namely lithium, xenon, and tin. The idea is to heat and vaporize the material to the point that it becomes a hot dense plasma. Once in the plasma state, atom species that achieve high charge states then undergo radiative emission of EUV light. In lithium plasma, the singular Lyman-alpha (Ly-α) of Li^{2+} emits at 13.5 nm from the 2p-1s transition. Alternatively, in Xe and Sn plasma, a cluster of transitions centered around 13.5 nm are emitted due to a vast multitude of possible transitions. In Xe plasma, these lines are principally produced by Xe^{+8}-Xe^{+11} whereas in Sn plasma, charge states Sn^{+8}-Sn^{+13} give rise to an unresolved transition array (UTA) of intense in-band emission and detrimental out-of-band emission. Ultimately, the source module must also include (in addition to the source) collection optics, debris mitigation schemes, and the necessary spectral filters to constitute the source-collector module (SoCoMo). Laser-produced plasma (LPP) design concepts have been shown favor in recent years for their capability of generating a steady, bright output of EUV radiation.

Currently, major research efforts are being devoted to the analysis and optimization of Sn LPP due to the higher efficiency of these plasmas in producing EUV photons in the 13.5 nm range [56]. Several studies showed dependences of the conversion efficiency (CE) of EUV source on different laser parameters, e.g., laser wavelength [57], pulse duration [58], intensity [59], spot size [60], as well as target geometry [61]. Variations of the above parameters will determine the optimum regime for EUV light output. A maximum CE for Sn LPP from planar targets is ~2.5% obtained by optimizing parameters of Nd:YAG laser [62]. A maximum CE of 4% has been achieved from a Sn cavity target [63] and of 5% in grooved Sn targets [64] using a CO_2 laser. Implementation of the above targets in a SoCoMo is a challenging task, so other elegant solutions are currently being explored. The currently preferred method, using a train of small

descending Sn-doped microdroplets [58,59,28], still faces such obstacles as a low CE and a need for debris mitigation schemes.

To further increase the CE of EUV light from the Sn plasma, dual laser pulse irradiation techniques have been successfully employed [60,61]. In this scheme, a high energy pumping pulse heats the low-density vapor/plasma created by a low energy pre-pulse. The total imparted laser energy is split optimally so as to supply sufficient vaporized Sn while effectively pumping the so-called pre-plasma to EUV generating temperatures. This increases the overall EUV emission efficiency. Implementation of this technique also serves to reduce the production of high-energy ions, preventing damage of collection optics [68]. Recent performance requirements set for future EUV lithography systems require 1000 W of clean, in-band EUV power thus necessitating further optimization of EUV sources. Detailed fundamental studies of laser-plasma interactions which are needed to help to identify ways of improving the source power and efficiency while extending the lifetime of system components.

5.2 Methodology

The experimental setup here-featured shares commonality to a typical laser-produced plasma setup – within a vacuum chamber, a nanosecond laser pulse is narrowly focused onto a foil target, causing ablation of target materials. In the present setup however, two laser beams are uniquely focused onto two separate (but closely positioned) surfaces as is depicted in Figure 5.1. The two LPPs created in close proximity may then expand into one another with great consequence to their mutual hydrodynamic development. The two Sn surfaces form a 90° wedge,

and the ablation sites are equidistantly positioned 0.65 mm from the shared edge (0.9 mm apart from each other).

A Continuum Surelite III Nd:YAG laser (τ_p = 6 ns, λ = 1064 nm) was used to generate the plasma. In order to simultaneously create the individual seed plasmas, the beam was split using a wedge prism which bisected the beam into a top and bottom portion. After diverging for some distance, the two beams passed through a large 20 cm planoconvex lens whereby they quickly converged towards a common focal point. The wedge target ensemble was positioned slightly ahead of the common focal point to establish the desired separation between the seed plasmas. The spot size was determined to be 300 μm. Laser energy was appropriately adjusted to acquire desired laser intensities. All shots were performed under a 3×10^{-6} Torr base pressure.

Two experimental techniques were used to study plume development. First, plume imaging of the colliding plasma setup was carried out using an intensified charge-coupled device (ICCD) (Princeton Instruments, PI-MAX) outfitted with a Nikon focusing optic attachment. Due to the limited magnification of this focusing optic, a 10 cm focal lens was placed within the chamber, at 11 cm away from the collision plane for additional telescopic magnification. The spectral sensitivity of the ICCD comprises UV-visible emissions range from 300-900 nm. Time-resolved plume images were acquired using a 2 ns gate width of exposure.

Empirical electron temperature and density measurements of the stagnation layer were obtained through spectroscopic analysis of Sn line emission. At incremental distances along the stagnation layer, spectra were collected for each cross section. Spectra were obtained using an Acton SP-2500i (Princeton Instruments) Czerny-Turner style spectrograph. Three different gratings (1800, 600, and 150 grooves/mm) could be accessed via a rotating turret within the spectrograph enclosure. For purposes of this study, the 600 g-mm^{-1} grating with 500 nm blaze

angle was used in acquiring line profiles of individual spectral lines with 0.39 Å resolution. The slit aperture to the spectrometer was open 20 μm. Calibration of the spectrometer was achieved using an HgAr pencil style calibration lamp which was also used to estimate instrumental broadening (0.97 Å) of the spectrometer.

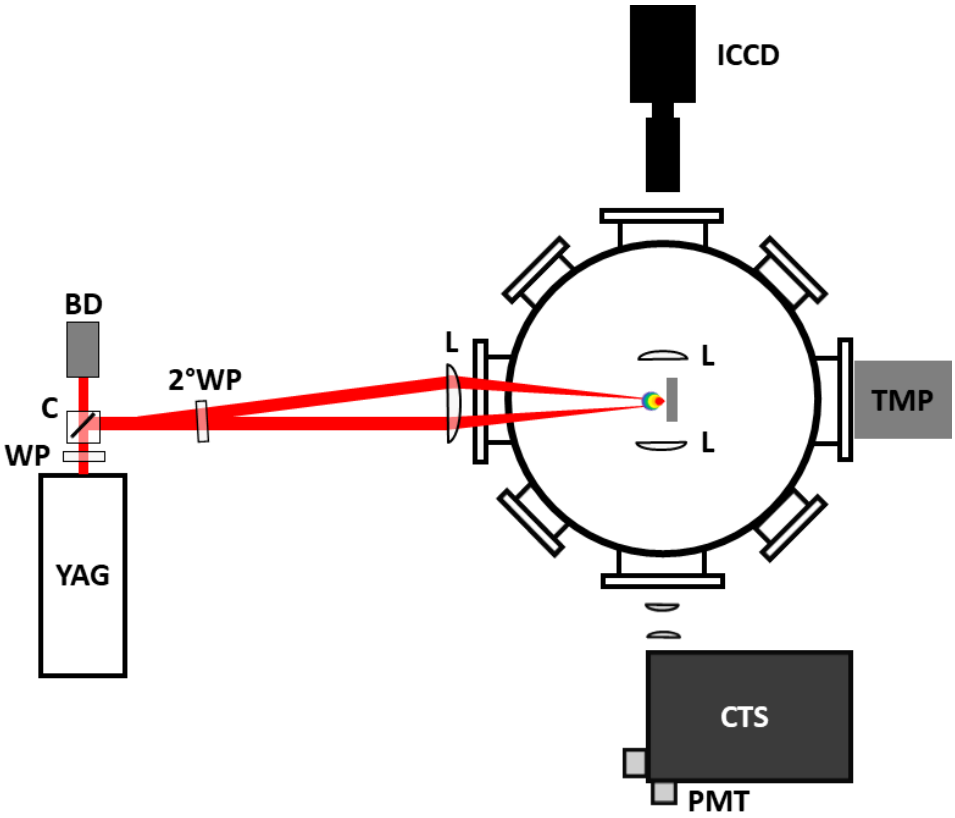

Figure 5.1 Experimental setup used in the study of colliding laser-produced tin plasma. Instrumentation used: Nd:YAG laser (YAG), Czerny-Turner spectrograph (CTS), intensified charge-coupled device (ICCD), turbomolecular pump (TMP), photomultiplier tube (PMT), 2° Wedge Prism (2°WP), waveplate (WP), cube polarizer (C), beam dump (BD), and lenses (L).

EUV emission from the colliding Sn plasma scheme was determined using an EUV power tool. The EUV power tool acquires plume emissions within a small solid angle, discriminating EUV emission using two 200 μm Zr filter foils and a Mo/Si dielectric mirror. An

AXUV-100G photodiode then measures the transmitted EUV light. The signal from the slow-response diode is integrated to quantify the yield of EUV light. The EUV emission was measured at 24° relative to the collision midplane between the two seed plasmas. For conversion efficiency calculation, EUV emission is reported per steradian.

Timing settings for Nd:YAG laser operation and ICCD external triggering were set using two synced programmable delay generators. The first delay generator (Stanford Research Systems DG535) was used to continually operate flash lamps of the Nd:YAG laser at 10 Hz while the second (Quantum Composers 9600+) triggered the Q-switch in single shot mode. Time monitoring of the laser pulse camera exposure as well as EUV signal acquisition from the EUV power tool was accomplished using a 1 GHz digital oscilloscope (Agilent D8104).

When determining temperature using the Boltzmann plot technique, it is important to select lines which span a range of values for the upper energy level. This allows greater coverage of the Boltzmann plot space, reducing potential method application error when implementing the linear regression. Appropriately, five emission lines of Sn II were chosen: 533.2 nm ($5s^2 6d\,^2D \rightarrow 5s^2 6p\,^2P^\circ$), 556.2 nm ($6d\,^2D \rightarrow 6p\,^2P^\circ$), 558.9 nm ($4f\,^2F^\circ \rightarrow 5d\,^2D$), 645.4 nm ($6p\,^2P^\circ \rightarrow 6s^2\,S$), and 684.4 nm ($6p\,^2P^\circ \rightarrow 6s^2\,S$). For the colliding plasma regime, an emission spectrum was acquired for the stagnation layer. Shown in Figure 5.2 (left), this wavelength-dispersed image was captured by aligning the slit along the length of the stagnation layer by rotating the slit using a Dove prism. This image concisely provides spectral information as it varies outbound along the stagnation layer (downward on the plot). During data collection, cross-sectional spectra taken from transverse slices along the stagnation layer length were alternatively captured to more accurately discern peak temperature. Regardless, the wavelength-dispersed spectral image effectively captures the diminishment and narrowing of lines farther

outbound along the stagnation layer. A typical Boltzmann plot procured from the spectra bearing our five emission lines of interest is also shown in Figure 5.2 (right).

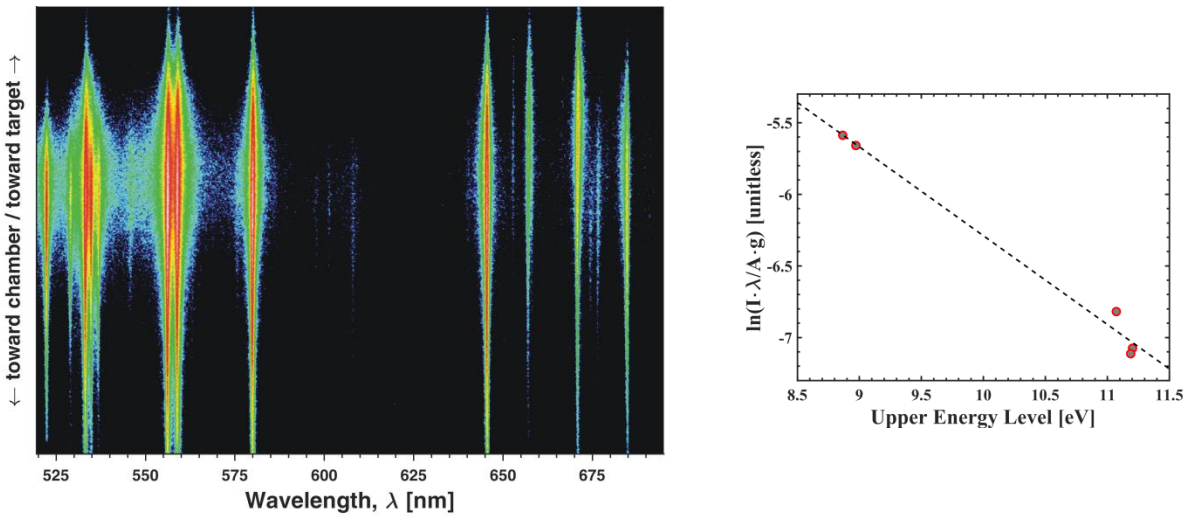

Figure 5.2 A wavelength-dispersed spectral image (left) depicts Sn emission along the axial length of the stagnation layer (logarithmic intensity scaling). At incremental distances, Boltzmann plots may be drawn (right) from which electron temperature is determined by the slope (-1/*kT*) of the fitted linear regression.

The electron density of the plasma may be ascertained from the spectral line width of a prominent bound-bound transition selected from the emission spectrum. High electron density within the plasma instigates Stark broadening of the line. This is caused by perturbations of atomic energy levels arising from a high local electric field enhancement. Literature provides temperature-dependent Stark broadening parameters which we may interpolate across different temperatures to determine electron density [21,70]. Multiple unique mechanisms concurrently contribute to line broadening (e.g. Doppler, pressure, instrumental, etc.) which should be reconciled for accurate electron density determination. Doppler broadening is minimal within the ~2 eV stagnation layer. Using the equation $\Delta\lambda_D(1/2) = 2\sqrt{ln2}\sqrt{2kT_r\lambda_0^2/M_Rc^2}$ [23], we

estimate Doppler broadening to be a mere 0.06 Å. The plasmas generated here are sufficiently low density for us to neglect pressure broadening. Instrumental broadening (0.97 Å) is significant and must therefore be subtracted from the observed line FWHM to obtain the empirical Stark widths.

For measuring electron density, the 645.4 nm ($5s^2 6p – 5s^2 6s$) line belonging to Sn(II) was identified as suitable due to its emission prominence and the greater relative invariance of its Stark broadening to plasma temperature. Furthermore, it is well isolated from other spectral features. The electron temperature determined earlier is used presently to provide the Stark broadening parameter, performing linear interpolation with literature values. The 645.4 nm line was captured using a 600 grooves/mm grating (0.39 Å spectral resolution) and fitted with a Lorentz fit using Origen© software. The electron density is then calculated using the relation: $\Delta\lambda_{½} = 2*w(T_e)$ $(n_e \times 10^{-16})$ ($\Delta\lambda_{½}$, Stark broadening FWHM [Å]; $w(T_e)$, temperature-dependent Stark broadening parameter [Å]; n_e, electron density [cm^{-3}])[22]**.** This treatment does not include the ion correction since the ion contribution to Stark broadening is marginal.

The multiphysics HEIGHTS computer simulation package was again used for the modeling and optimization of both single LPPs and colliding plasmas produced from tin targets. The package has been extensively used for fundamental study and parameter optimization of laser- and discharge- produced plasmas at the regimes relevant to EUV photon source development [71,26]. Recently, the package was also used for the modeling colliding plasmas produced from carbon targets [71]. The work was devoted to the study of mechanisms of carbon macromolecules formation using several experimental tools and modeling technique.

5.3 Seed Plasma

In order to properly characterize the stagnation layer formed by colliding plasma, it is important to understand the properties of an individual plasma plume so we may effectively distinguish this behavior from that attributed to the colliding plasma. The purpose of separately studying seed plasma is twofold: (i) it elucidates an understanding of their individual contribution, and (ii) it serves as a control group upon which behavior intrinsic to the colliding plasma regime may be identified.

The mechanism for laser ablation from a nanosecond laser features three developmental stages. First, the leading front of the laser pulse deposits its initial energy into the target surface, creating plasma at the focal spot. During the second stage, the remaining portion of the laser pulse interacts with the nascent plasma; this is called laser-plasma interaction (LPI). Plasma heating during this interval is isothermal. Upon termination of the laser pulse, the LPP cools, undergoing free adiabatic expansion (third stage).

5.3.1 Seed plasma characterization using optical emission spectroscopy

Optical emission spectroscopy (OES) of laser-produced tin plasma was performed to determine electron temperature and density of the developed plasma in the manner outlined in Section 1.5.3. Here, a 2.5×10^{10} [W-cm^{-2}] laser intensity was normally incident on the Sn foil. Figure 5.3 shows key plasma parameters: electron temperature and electron density. The ICCD exposure began 50 ns after laser incidence with 300 ns gate width of collection. The start at 50 ns corresponds to the approximate moment in colliding plasma development when visible spectroscopy becomes viable. Prior to this time, the seed plasma possesses high electron

temperature and density which causes a preponderance of continuum emissions while simultaneously being optically thick to visible emissions and emitting in the ultraviolet window. In particular, EUV light is emitted during the earliest few nanoseconds (nearly cotemporaneous with the laser pulse) from seed plasma exhibiting 30-40 eV temperature.

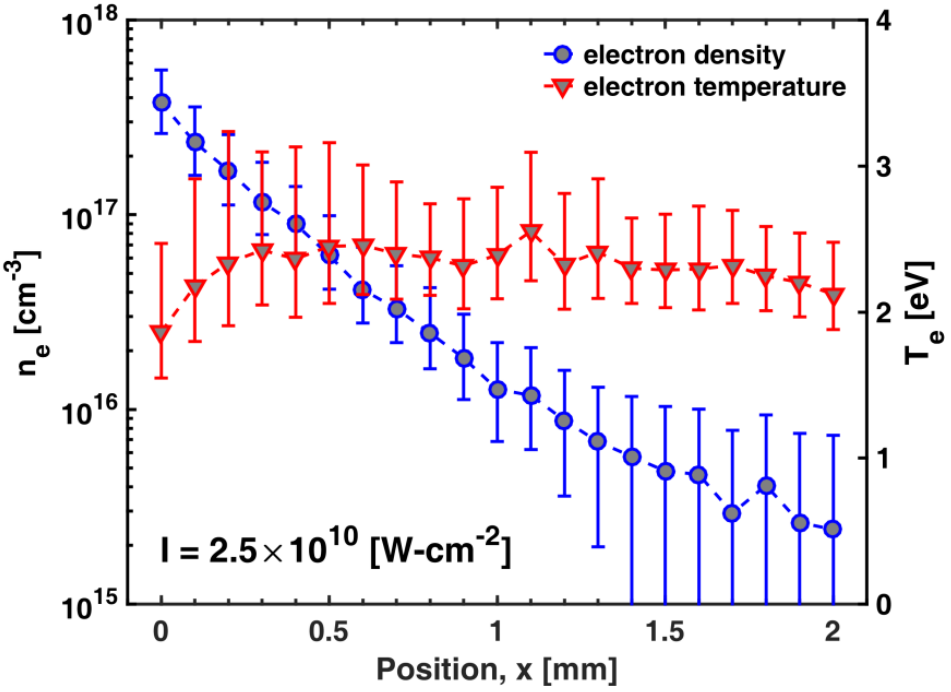

Figure 5.3 Electron temperature and electron density outbound along the central axis of an individual laser-produced plasma generated by a 2.5×10^{10} [W-cm^{-2}] laser intensity (250 μm spot diameter).

Over the 300 ns time-integration, electron temperature remained mostly constant at about 2 eV. Conversely, electron density shows monotonic exponential decrease, dropping approximately two orders of magnitude over 2 mm. The contribution to electron temperature arising from the wave of hot multi-charged ions is demoted by this method. Time-integrated spectroscopic techniques inherently weight moments during the gated exposure which correspond to a high concentration of the line-emitting species. While the outermost front of the

expanding plasma considerably exceeds 2 eV, temperature information is relayed only later once appreciable quantities of Sn(II) have arrived. Spectroscopy results provide good estimation of electron temperature for regions abundant with Sn(II).

Error in temperature values arises from the data processing, specifically error from the fitting of Boltzmann plot regressions. Temperature error is propagated into the electron density calculation since plasma temperature is used to determine the Stark parameter. For more narrow lines, the spectral resolution introduced greater error. Both of these errors were added in quadrature and are depicted in Figure 5.3.

5.3.2 Seed plasma simulation using HEIGHTS

Time-resolved simulations from HEIGHTS modeling provide valuable information regarding species concentrations and plasma properties of the evolving plasma plume. We use this information to explain the spatiotemporal development of the laser-produced Sn plasma. During laser-plasma interaction, a high pressure region located at the laser absorption front manifests a high electron density and multi-charged ions. Hot ions located along the laser absorption front possess high kinetic energy and are first to propagate away from the ablation site. Figure 5.4 shows the aggregated distribution and concentration of multicharged Sn^{2+}-Sn^{5+} ions as the plume develops over 150 ns. It is seen that the populations of these ions quickly rarefy into the plasma chamber.

The emergence of singly charged Sn(II) differs slightly from that of its higher charge-state counterparts. The time-dependent concentration of Sn(II) from 50 to 300 ns is shown in Figure 5.5. Sn(II) is produced via electron-ion recombination in the wake of the multicharged ions, facilitated by the frequent collisions made by electrons. As the plasma cools, electrons are

reclaimed by the ions (recombination) in a manner acquiescent to local thermodynamic equilibrium. The average charge state of the plasma then drops.

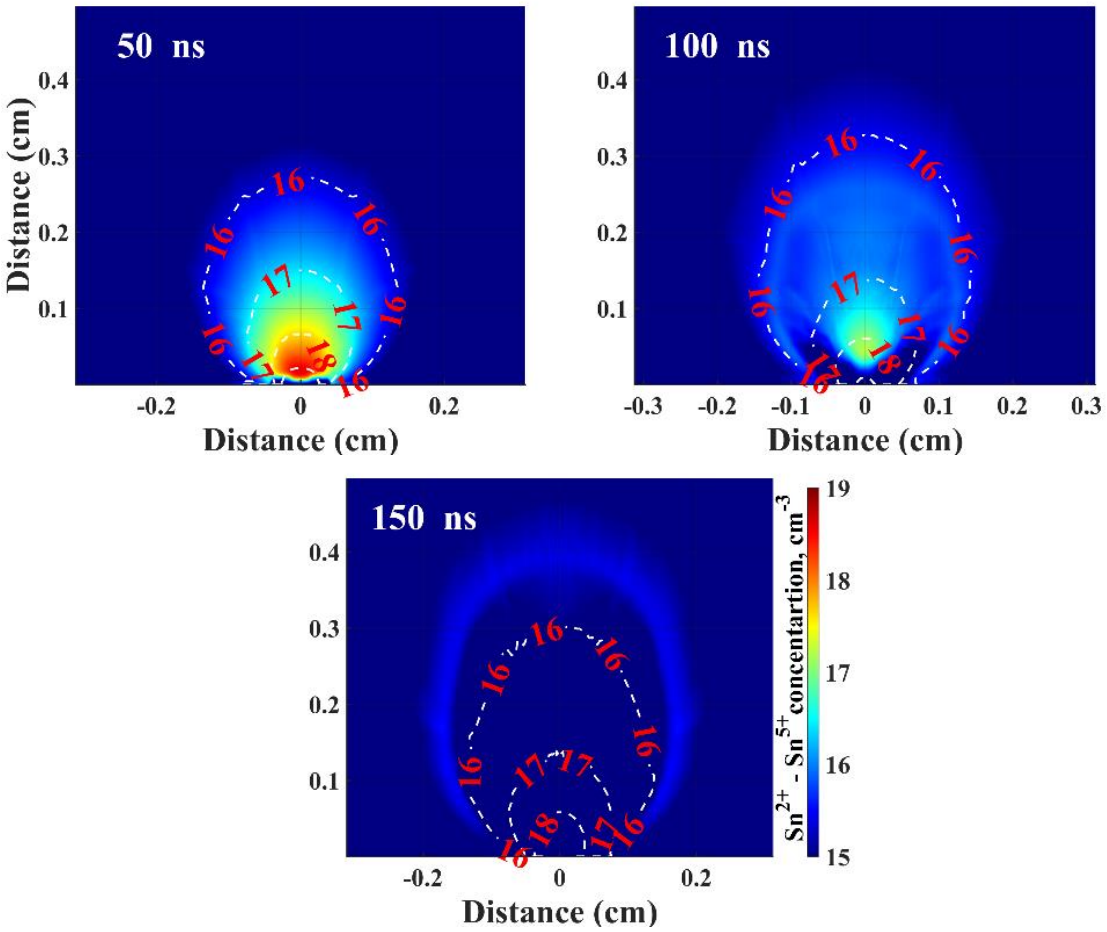

Figure 5.4 Aggregate concentration of Sn^{2+} - Sn^{4+} ions in Sn LPP generated by a 2.5×10^{10} [W-cm^{-2}] Nd:YAG laser irradiation (250 μm spot diameter) after 50, 100, and 150 ns plume development. White contours show the logarithm of electron density [cm^{-3}].

A dense, low-temperature plasma hovers slightly above the target surface where the target was exposed to the intense laser irradiation. Ensuing the laser-plasma interaction, a wave of hot ions is jettisoned. In accordance to Newton's third law, the plasma caught in-between the hot ion blowoff and the target experiences a compressive force. Intense radiation from this dense

plasma causes continued erosion of the target surface, further supplying the near-surface plasma with additional ablated materials. This region is rich with Sn(II) and Sn (I) neutrals.

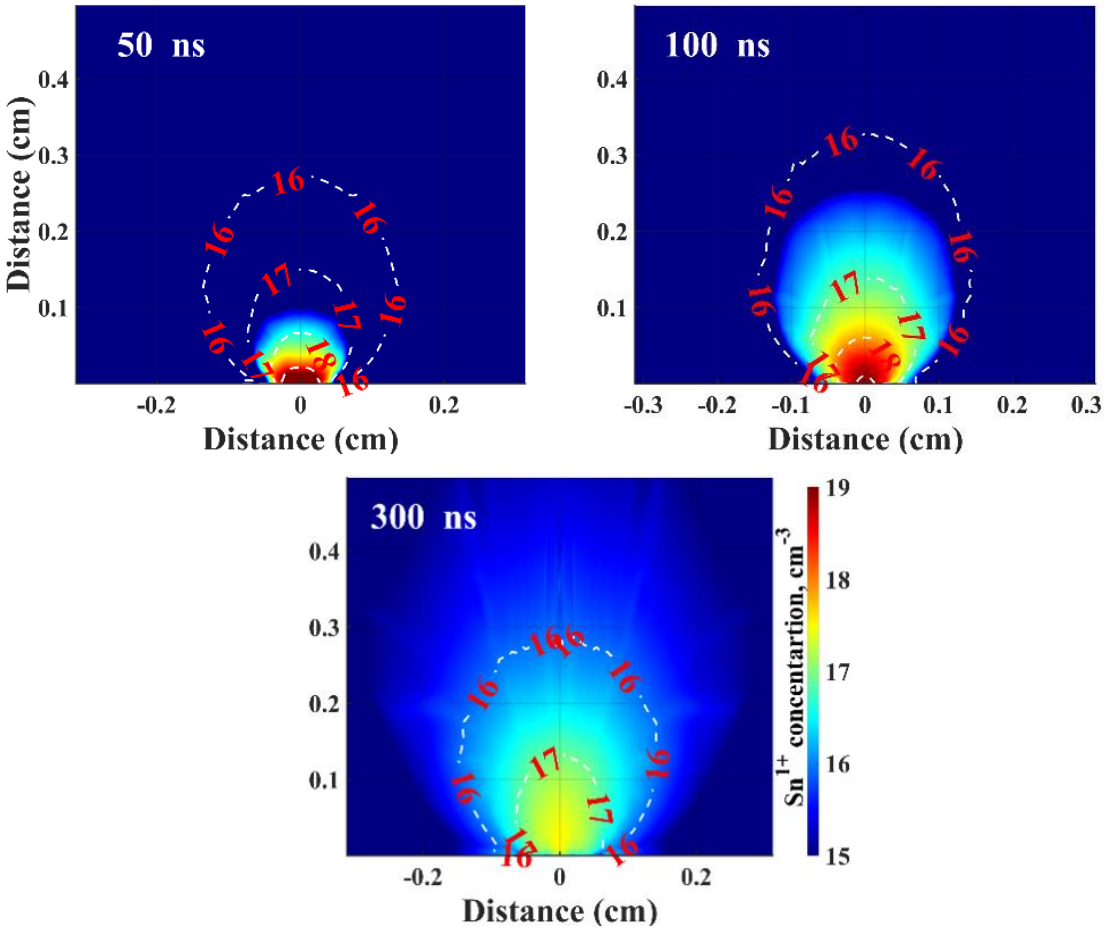

Figure 5.5 Concentration of Sn^{1+} ions in Sn LPP generated by a 2.5×10^{10} [W-cm^{-2}] Nd:YAG laser irradiation (250 μm spot diameter) after 50, 100, and 300 ns plume development. White contours show the logarithm of electron density [cm^{-3}].

Electron density and temperature (white contours) of the single plasma are shown in Figure 5.6. The hottest region of the plasma occurs along the expansion front of the plasma, reaching temperatures of ~7 eV at 40 ns after end of the laser pulse. The dense near-surface

plasma retains a more modest temperature of ~1-2 eV over the course of plume evolution from 50 to 300 ns.

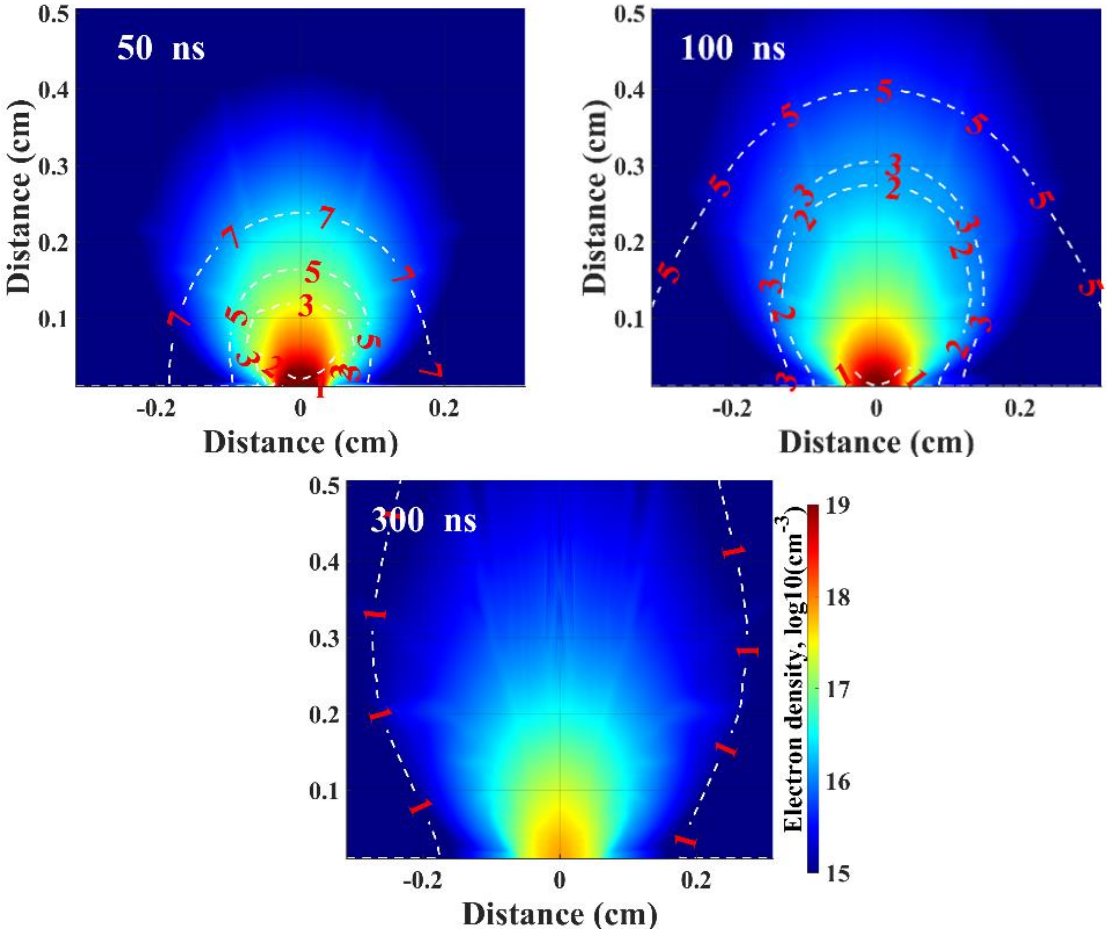

Figure 5.6 Electron density of Sn LPP generated by a 2.5 × 10^{10} [W-cm^{-2}] Nd:YAG laser irradiation (250 μm spot diameter) after 50, 100, and 300 ns plume development. White contours show electron temperature [eV].

5.4 Stagnation Layer – Colliding Plasma Regime

In the preceding section, plume evolution dynamics of an individual seed plume was discussed. Here, we incorporate this knowledge into our discussion of colliding plasma. In a

colliding plasma regime, fast ions from each seed plume are first to intersect along the midplane bisecting the two plasmas. For an individual seed plasma, it was previously observed that the hot ion population (Sn^{2+} – Sn^{5+}) quickly rarefied or underwent charge reduction via recombination. In the present situation, a significant fraction of these hot ions scatter with comparable hot ions originating from the opposing seed plasma. These scattering events lead to a buildup of material along the collision midplane. The lagging portion of the seed plume now observes this relatively hot, dense stagnation layer and will continually supply seed plume material until all evaporated matter is exhausted. We will begin by observing the plume morphology with fast imaging and follow with plasma spectroscopic analysis and HEIGHTS computational modeling.

5.4.1 Plume morphology using fast imaging

The collision between two laser-produced plasmas may be readily observed through plume imaging. Plume imaging (described herein) is obtained by mapping the focused image from the object plane onto an ICCD matrix. Appropriately, the image only comprises photoemissions from the region of the electromagnetic spectrum which is readily transmitted through system optics and corresponding to high detection efficiency (i.e. visible emissions) of the ICCD apparatus. Typically, plasma most efficiently emits in the visible spectrum when it possesses electron temperature of only a few electron-volts (eV). For the ensuing plasma collision regimes being considered, plasma temperatures may reach several tens of eV, incurring emission in the extreme ultraviolet. It is therefore appropriate to interpret plume images with due consideration for the local emissivity across various light wavelengths. Regardless, plume imaging provides a valuable tool to discern general development of the plasma system. Figure 5.7 shows (a) the collision process leading to the formation of the stagnation layer at 2×10^9 [W-

cm^{-2}] laser intensity and (b, c) the developed stagnation layers at higher laser intensities 6×10^9 [W-cm^{-2}] and 2×10^{10} [W-cm^{-2}] (b and c respectively).

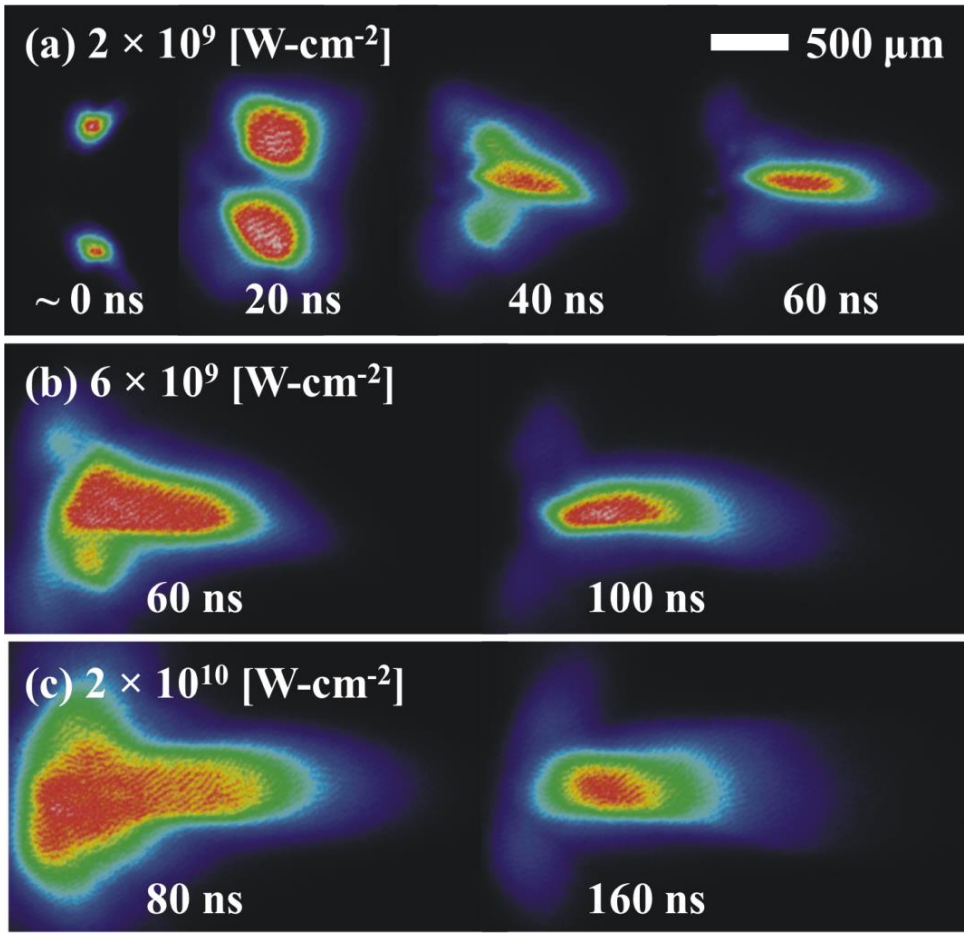

Figure 5.7 Plume images for a colliding plasma regime (laser incident from right) with 0.9 mm separating the seed plasmas across three laser intensities: a) 2×10^9, b) 6×10^9, and c) 2×10^{10} [W-cm^{-2}] respectively.

The strip of images shown in Figure 5.7(a) depicts the collision of two individual seed plasmas giving rise to the formation of a stagnation layer along the collision midplane (the frame at t = 0 ns has been embellished to better show the initial positions of seed plasma). At 20 ns, the seed plumes have undergone expansion at a rate of ~3×10^6 [cm/s]. The image shown at this

timestep features a red region speckled with white (the color of maximum normalized intensity). This flat-top intensity profile suggests a high plume opacity due to overdense plasma. Since the collected emission is line-integrated along the observation axis, light originating from within the plasma interior may experience self-absorption. By 40 ns, the two plumes have collided, forming the stagnation layer. The stagnation process effectively reclaims ion kinetic energy from expanding the plasmas as internal energy, interrupting the natural rarefactive expansion of these plasmas. This promotes the accumulation of ablated Sn material along the stagnation layer.

As the laser intensity was increased to 6×10^9 and 2×10^{10} [W-cm^{-2}], plume imaging revealed increased occurrence of plasma optically dense to visible light. This indicates plasma temperature significantly exceeding ~5 eV. Figure 5.7(b) and (c) show the enlarged stagnation layer resulting from use of higher laser intensity (and energy). The two images were acquired at a later delay, providing time for the stagnation layer to both rarefy and cool.

5.4.2 Plasma characterization using optical emission spectroscopy

For two colliding plasma scenarios presented in the preceding fast-imaging section (2×10^9 and 2×10^{10} [W-cm^{-2}]), spectra were collected along the length of the stagnation layer with intent to determine electron temperature from Boltzmann plots. As was realized from plume fast-imaging, stagnation layer development is greatly influenced by seed plume behavior which further varies across the parameter space of laser intensity. Increasing drive laser intensity prompts the stagnation layer to reach a higher temperature during the first 50 ns. This requires that visible spectroscopy be performed later once the stagnation layer is no longer optically thick.

Figure 5.8 provides electron temperature and density along the stagnation layer manifested using laser intensities (a) 2×10^9 and (b) 2×10^{10} [W-cm^{-2}]. Spectra are time-

integrated over 300 ns with acquisition beginning at 70 and 150 ns delay respectively. The electron temperature remains largely steady along the length of the stagnation layer. The peak value exists slightly outbound from the seed plasma plane. Anterior to the seed plasma, the stagnation layer declines in temperature. Seed plume expansion is greatest along the target-normal. For this wedge configuration, this prompts hydrodynamic pressure imposed by seed plasma to develop the stagnation layer farther out, posterior to the seed plasma plane. Anterior to the seed plasma plane, continual erosion of the Sn surface (caused by intense radiation from near-surface plasma) may introduce relatively cold matter to the plasma, maintaining a low local temperature.

Electron density along the length of the stagnation layer is also shown in Figure 5.8(a) and (b). Even though the ICCD exposure began later for the high laser intensity case, it is seen that electron density of the stagnation layer has increased considerably. The electron density of the plasma appears to reach a peak slightly outbound from the seed plasma plane. Again, this is likely due to some optimized collision scenario between (i) alignment with seed plume target-normals and (ii) close proximity to the seed plasma. Alternatively to electron temperature (which remains largely steady), electron density exhibits a marked reduction farther out. However, unlike during single plasma evolution, the electron density remains steadily above $\sim 10^{16}$ [cm^{-3}]. This is maintained by the accumulated material along the stagnation layer and the concomitant conversion of kinetic energy from fast ions into plasma internal energy.

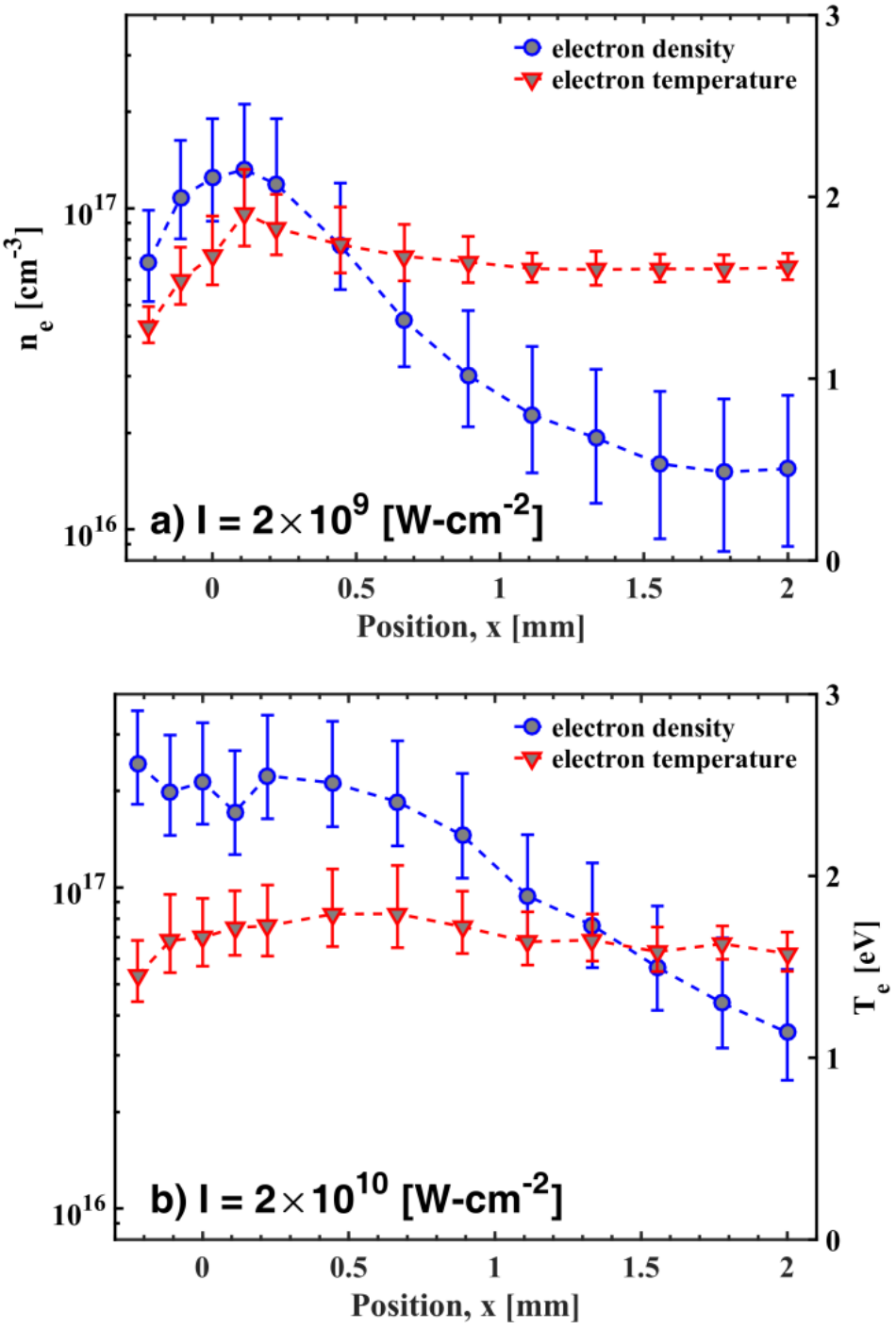

Figure 5.8 Electron density and temperature axially along the columnar length of the stagnation layer constructed from seed plasma (produced using two laser intensities: 2×10^9 and 2×10^{10} [W-cm^{-2}]). The position x = 0 corresponds to the cross section of the stagnation layer which is coplanar to the seed plasmas.

The validity of these spectroscopic methods to determine electron temperature and density largely rests on the appropriateness of certain assumptions made. One such assumption is that the plasma is in local thermodynamic equilibrium (LTE). We revisit the McWhirter criterion which was introduced in Section 1.5.4. Supplying $T \approx 18{,}000$ K (~1.6 eV) and $\Delta E = 1.92$ eV, we must then have $n_e > 4.1 \times 10^{14}$ [cm^{-3}]. The McWhirter criterion is easily satisfied (even for single pulse data discussed earlier). However, error may arise elsewhere from neglecting the optical opacity on the plasma. A degree of self-absorption is expected within the plasma. Figure 5.9 shows (top) the mass density distribution in the colliding layer along Y axes obtained from the HEIGHTS simulation and (bottom) calculated Sn plasma opacities at relevant temperature in visible range.

The stagnation layer is indeed a layer of plasma, extending over a greater area of the collision midplane than just the immediate vicinity between the two seed plumes. Figure 5.9 (top) indicates that the plasma scale length along Y is approximately 0.1 cm, considerably larger than the width of the stagnation layer. A side view of the stagnation layer (XZ plane) may depict the plasma to be columnar, but it actually spans considerably along the Y axis. Using Figure 5.9 (bottom), we estimate the minimum optical mean free path of the 645.4 nm (1.92 eV) emission (which was used for density measurements) to be ~0.1 cm under the considered conditions. Opacity effects are thus anticipated to affect line shape and diagnostic results derived therefrom. Quantified error (errorbars) arises from the same sources discussed earlier in Section 5.3.1 for single plasma.

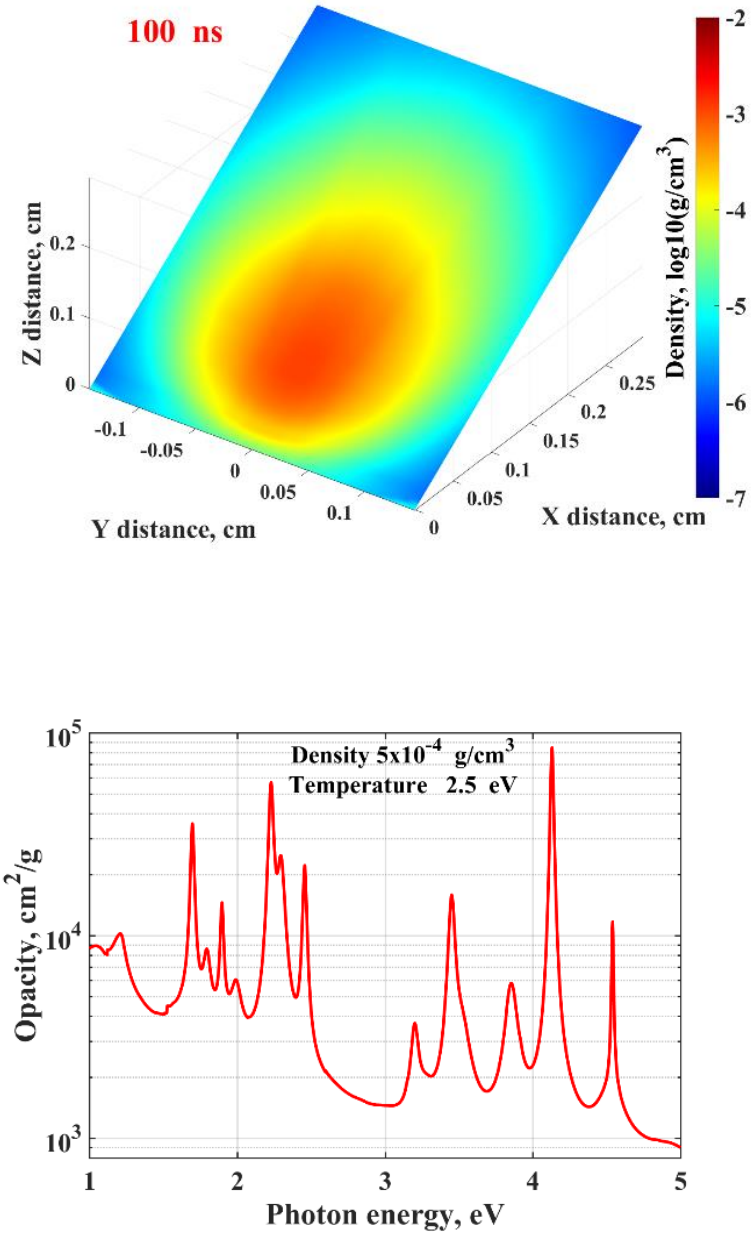

Figure 5.9 HEIGHTS simulation results: mass density distribution (logarithmic values) along Y axes of the stagnation layer formed from seed plumes produced by lasers with 200 μm spot size and 5×10^{10} [W-cm^2] intensity (top) and Sn plasma opacities (bottom) at relevant temperature and density.

5.4.3 Colliding plasma simulation using HEIGHTS

Empirically measured electron temperature and density were compared with modeling results. The colliding plasma regime was modeled using similar laser energy and duration as in the experiment and with 200 μm spot size. Figure 5.10 shows the distribution of temperature and density at 100 ns for 4×10^9 and at 150 ns 5×10^{10} [W-cm^{-2}] laser intensities. Despite hotter and denser seed plasma being created by the higher intensity laser irradiation, with maximum temperature of 60 eV for 5×10^{10} W-cm^{-2} compared to 15 eV maximum temperature achieved in the case of 4×10^9 W-cm^{-2} intensity, the equilibrium plasma temperatures in the stagnation layer at later time are approximately the same and are similar to temperatures found in experiment (Figure 5.8 and Figure 5.10).

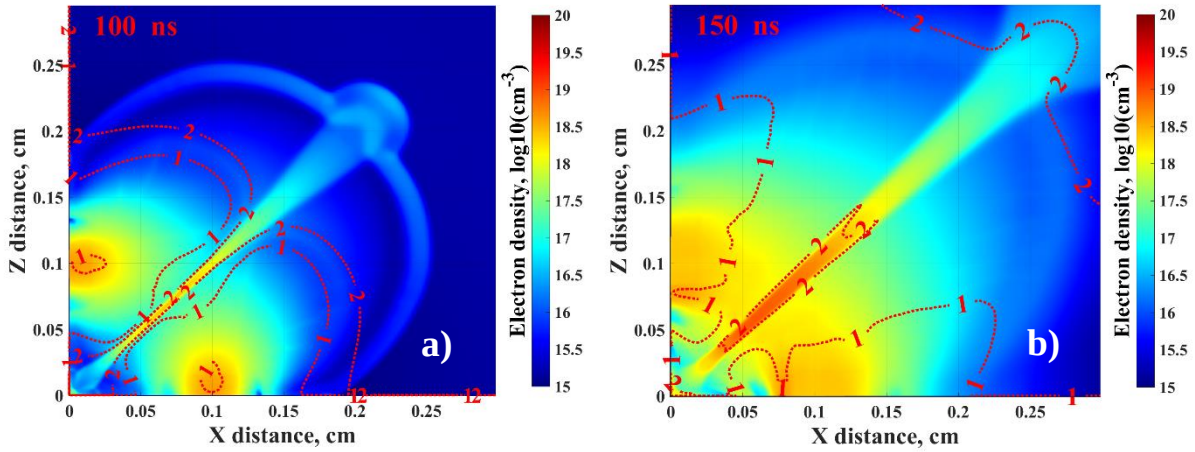

Figure 5.10 Electron density (logarithmic values) and temperature (shown by red contours) distribution in colliding plasmas at 100 ns and 150 ns created by Nd:YAG lasers with 6 ns duration and with intensities of a) 4×10^9 and b) 5×10^{10} [W-cm^{-2}].

The main difference in the stagnation layer formed at lower laser intensities is determined by the difference in the ablated mass that determines the stagnation layer evolution dynamics, i.e.,

interpenetration or stagnation of collisional plasmas; transition to cooling and expansion of the formed dense layer [21]. The high intensity laser irradiation ablated 5 times more mass that resulted in denser stagnation layer (Figure 5.10(b)). Continuous expansion of seed plumes leads to long time persistence of stagnation layer (Figure 5.11) that can be optimized for double-pulse technique to produce powerful EUV source.

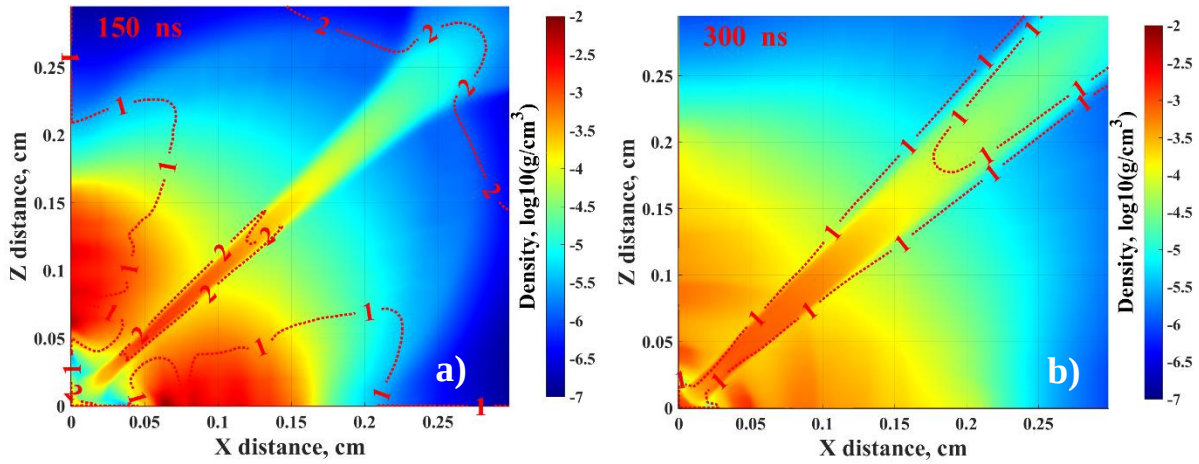

Figure 5.11 Mass density (logarithmic values) and temperature (shown by red contours) distribution in the stagnation layer formed from seed plumes created by laser pulse with 5×10^{10} [W-cm^{-2}] intensity at a) 150 ns and b) 300 ns.

When using higher laser intensity, a more pronounced and dense layer is formed which would benefit from being reheated by a second, pumping laser pulse (viz. CO_2 laser) to produce a large EUV-emitting and sustainable interaction area. From a side view of the XZ plane, the colliding layer appears to feature a column shape whereas the pancake shape observed in the XY plane (Figure 5.9) suggests potential high photon reabsorption that can affect plasma parameter measurements as well as EUV source efficiency.

5.5 EUV Emission

The unique features of long lasting stagnation layer can be optimized for EUV source production by adjusting laser parameters and the system geometry within the dual-pulse scheme. Reheating the well-developed pre-plasma by a second [CO_2] laser enhances efficiency of LPP-based sources and will significantly increase the source power, a task vital for the current development of high volume manufacture (HVM) tools. The high intensity laser irradiation creates plasma with a 60 eV maximum temperature in the seed plumes and with 30-40 eV plasma in the stagnation layer (Figure 5.12(a)). Electron temperatures from 30-40 eV manifest the highest EUV photon (13.5 nm) production from Sn plasma. Electron density is another important parameter and the combination of both determines source location and intensity (Figure 5.12).

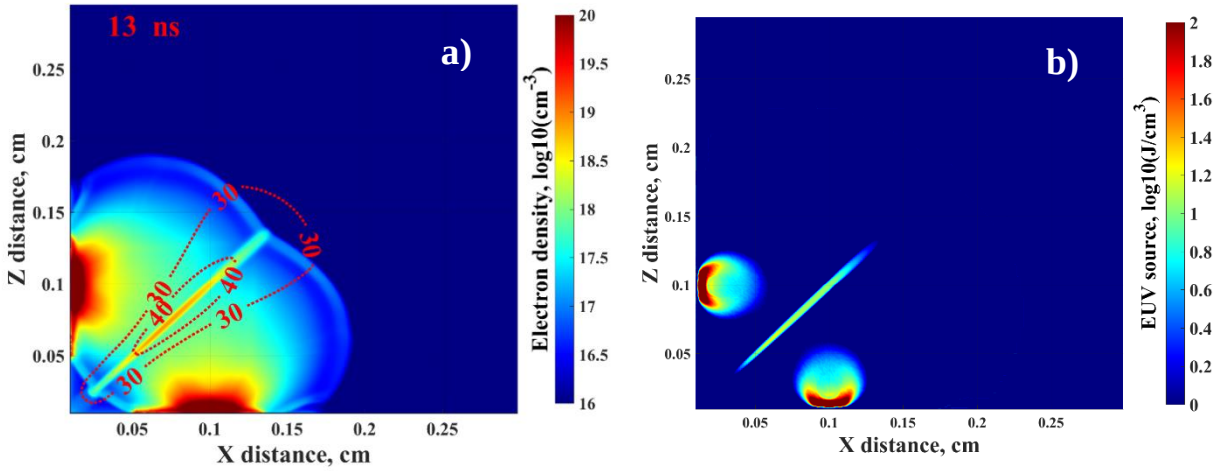

Figure 5.12 a) Electron density (logarithmic values) and temperature (red contours) distribution in plasma created by lasers with 5×10^{10} [W-cm^{-2}] intensity;
b) time-integrated EUV source from developed plasmas.

Figure 5.12(b) shows that the EUV source can be produced during the initial stage of plasma collision with most EUV being produced by seed plasma. While the colliding layer possesses an optimal electron temperature, only marginal EUV is produced due to a much lower electron density. The path forward entails optimizing the stagnation layer as an ideal pre-plasma for CO_2 laser coupling. This dual Nd:YAG laser scheme showed smaller EUV source efficiency, 1.8%, in comparison with 2.1% efficiency of the source produced by single laser with similar laser parameters and collected in 2π sr. This reduction is caused by much smaller collecting angle possible in colliding plasma device, slightly larger than π sr. In our HEIGHTS simulation, we calculated the actual EUV photon output at free surfaces of 3D domain taking into account photon absorption on their way to these surfaces. The angular distribution of the in-band EUV fluence obtained in this manner is shown in Figure 5.13(a). Radiation produced in the developed plasma was partially absorbed in the neighboring plume, resulting in a slightly increased plasma temperature in comparison with singular seed plasma. The efficiency of the above system could be increased further by purposely shaping the laser spot. A more elliptical spot (shorter along the Y axis) would reduce deleterious lateral expansion of the stagnation layer along the Y axis. Reducing the plasma scale length in Y promotes the creation of a more localized EUV source resulting in lower etendue and improved overall utilization of produced EUV light.

EUV emission from this configuration was studied experimentally (Figure 5.13(b)) with an absolutely calibrated EUV power tool. The tool placement was fixed at 69° relative to the X plane, coplanar with seed plasma. The EUV emission was collected from the colliding plasma regime (red) and from the collective emission from each seed plasma collected individually (blue). Emission originating from the stagnation layer or emission enhancement caused via some other synergistic mechanism involving both plumes may be discriminated out via this manner.

Ultimately, only a marginal increase in EUV output was observed for the colliding plasmas at the considered measurement angle, suggesting that the total EUV output was unaffected by the synergy between the two plasmas. Figure 5.13(a) shows the agreement between experiment and modeling at the pertaining parameters.

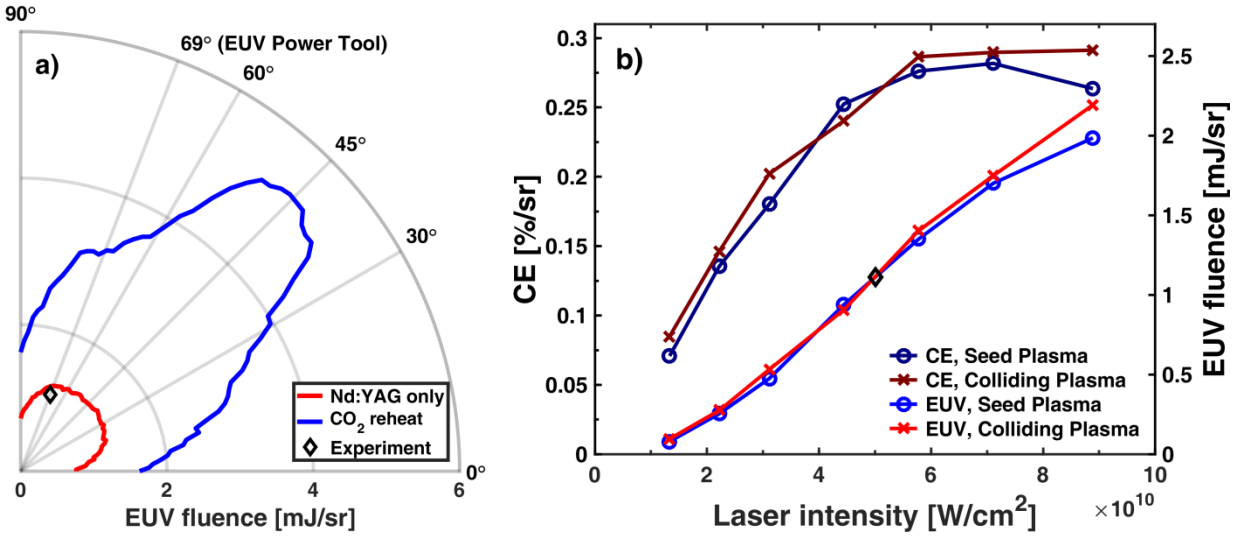

Figure 5.13 a) The angular distribution of EUV emission (13.5 ± 2% nm) incident upon a reference sphere of radius 0.25 cm (centered at origin); laser intensities are 5×10^{10} [W-cm^{-2}] Nd:YAG and 7×10^{9} [W-cm^{-2}] CO_2 b) empirical data for EUV emission (no CO_2 laser reheat).

Reheating of the developed stagnation layer by CO_2 laser with 400 μm spot size, 30 ns duration and 7×10^{9} [W-cm^{2}] intensity produced a source with 3.5% efficiency (Figure 5.14). Figure 5.14(b) shows that the actual collecting angle is much smaller than 2π sr upon assuming imposing material surfaces across X and Z planes. Reducing the collection angle by almost a factor of two in comparison with a single plasma system provides compensation for the relatively large source area that is restricted by the etendue requirement of the optical system [72]. From Figure 5.14(a), we may elucidate that the EUV emission is directionally biased towards the

center of our π sr collection angle. The complex 3D geometry investigated here does not possess radial symmetry. Therefore, further study is needed to fully map the two-dimensional angular emission profile which includes azimuthal variation. Currently, our TEA CO_2 laser system in the lab is incapable of attaining the necessary laser intensity for efficient heating of larger stagnating plasma layer.

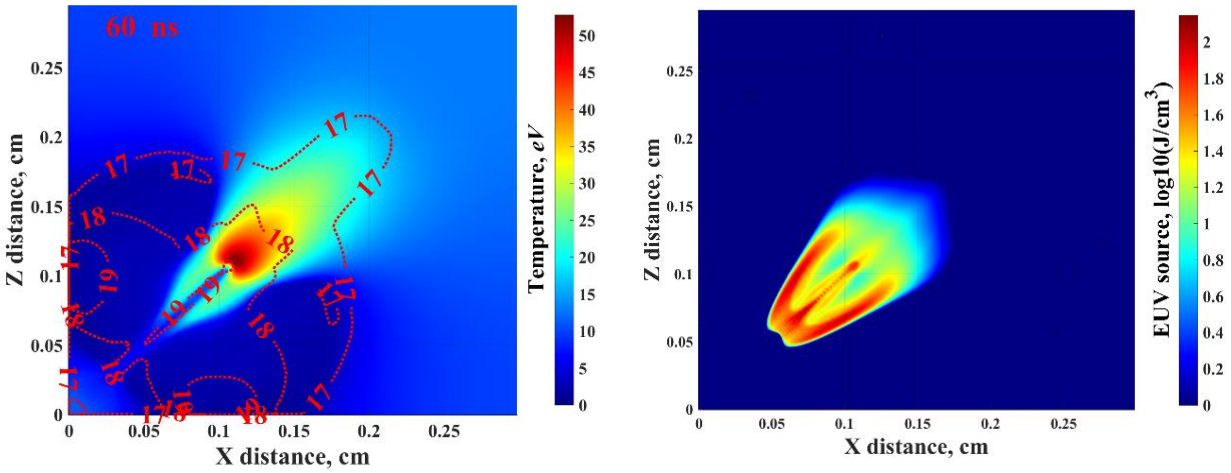

Figure 5.14 (a) CO_2 laser interaction with stagnation layer; (b) time-integrated EUV source produced by CO_2 laser from the stagnation layer.

The most important result of this work is the high EUV power that can be produced by the above proposed three-laser system. Currently, the optimized laser systems feature a EUV source with 250 W power [73]. The ultimate goal of future EUV lithography tools is to achieve 1000 W EUV output at the intermediate focus (IF). The colliding plasmas scheme described above produces around 12 mJ EUV in a single iteration. Taking into account an optical system reflectivity of 60% and assuming 100 kHz laser system, approximately 700 W EUV source can be developed in this configuration. Further optimization of laser parameters, e.g., laser spot shape to reduce EUV reabsorption in the layer developed along the Y axis, seed plumes size and

location, and time delay between Nd:YAG and CO_2 lasers can further increase the efficiency as well as the EUV source power.

5.6 Conclusion

The stagnation layer formed from colliding Sn plasmas was investigated as a potential pre-plasma target for an efficient high power EUV production. This plasma was studied using spectroscopy techniques to determine plasma temperature and density and was subsequently compared with results obtained from individual seed plasma which provided a control group. The HEIGHTS comprehensive simulation predicted detail time-resolved data of plasma temperature, plasma density, and accumulated mass density that agreed well with the experimental results. The EUV emission character of the colliding plasma scheme was also explored. Prior to using a delayed laser to reheat the stagnation layer, the total EUV being emitted from the colliding plasma regime remained largely unchanged though a decrease in conversion efficiency is predicted (from 2.1% to 1.8%) upon halving the collection angle from 2π sr to a more appropriate π sr. The interaction with a delayed main driver CO_2 laser with the preformed stagnation layer was simulated using HEIGHTS and predicted a 3.5% CE source collected in π sr. Furthermore, 12 mJ of useable EUV is produced during a single iteration, suggesting viability for high source power to meet imminent high volume manufacturing (HVM) requirements of power exceeding the 500-1000 W at the intermediate focus.

6. ASSYMETRIC PLUME MORPHOLOGY OF COLLIDING SILICON AND CARBON PLASMAS

In the preceding chapters, colliding plasma was created with seed plasma symmetry along the collision midplane using target material of identical elemental composition on either wedge surface. Presently, the collision of two laser-produced plasmas from different target materials (carbon and silicon) is shown to develop a very asymmetric stagnation layer due to unique laser-target coupling of the two surfaces. The asymmetry is both hydrodynamic and thermal in nature. Such a colliding plasma scheme could enable plasma-assisted chemistry promoting desired molecular formation.

6.1 Introduction

The majority of colliding plasma research has been focused on the collision between like plasmas which possess symmetry along the collision midplane. However, the use of colliding plasmas comprised of dissimilar material could prove advantageous for purposes of plasma-assisted chemistry. Thermal plasmas are known to synthesize large structures such as nanoparticles and carbon nanotubes if conditions are suitable within the plasma [74]. It is typical for the plasma to benefit from the presence of an inert ambient environment which provides confinement of the expanding plasma. In the work involving carbon nanotube synthesis, a He flow over the graphite surface is used as a carrier gas [75]. Greater gas confinement promotes clustering by increasing the collision frequency of cluster precursors in the plasma. Colliding plasma can mimic some of the confinement effects of a gas ambient while enabling the possibility of intermixing two plasmas with unique elemental composition. In the present work,

the collision between carbon and silicon plasma is partially motivated by the possibility of synthesizing silicon carbide (SiC).

Silicon carbide is a semiconductor which has been used for a variety of purposes including as an abrasive and to form very hard ceramics such as those contained in bulletproof vests. Its high-temperature hardness, wear resistance, low thermal expansion coefficient, high thermal conductivity and corrosion resistance has made SiC an ideal material for aerospace applications as well as for TRISO fuel in advanced pebble-bed nuclear fission reactor designs [76]. Its use has garnered further interest in the field of next generation photonics and electronics [77]. Synthesizing SiC nanocrystals is often accomplished by electrochemical etching of solid SiC wafers or by wet chemical etching of SiC powder [78,79] though techniques featuring plasma synthesis have been shown effective [80]. Most study of SiC follows a top-down approach. Studying colliding Si and C plasma could offer useful information regarding the fundamental early processes that give rise to SiC formation in a plasma environment.

6.2 Experimental Setup

Experiments were conducted in a vacuum chamber with low pressure (0.1 Torr) He ambient (Figure 6.1). Using two half-wave plate/ beam splitter pairs, 200 mJ from a Nd:YAG laser pulse (τ_p = 6 ns, λ = 1064 nm) was split equally into two separate beam paths each bearing a 100 mJ pulse. Both laser pulses were focused onto the target assembly. The target assembly resembles a wedge forming a 90° right angle. In previous experiments, both faces of the wedge would be constituted of material of identical composition (e.g. both being graphitic carbon or tin). In the present study, the two surfaces are of dissimilar composition: the top face is graphitic

carbon while the bottom face is silicon. Both laser pulses are focused to a relatively large 1.5 mm spot diameter (1×10^9 W/cm^2 laser intensity). The center of each spot is 3 mm distant from the shared edge, entailing that the seed plasmas are generated 4.2 mm apart.

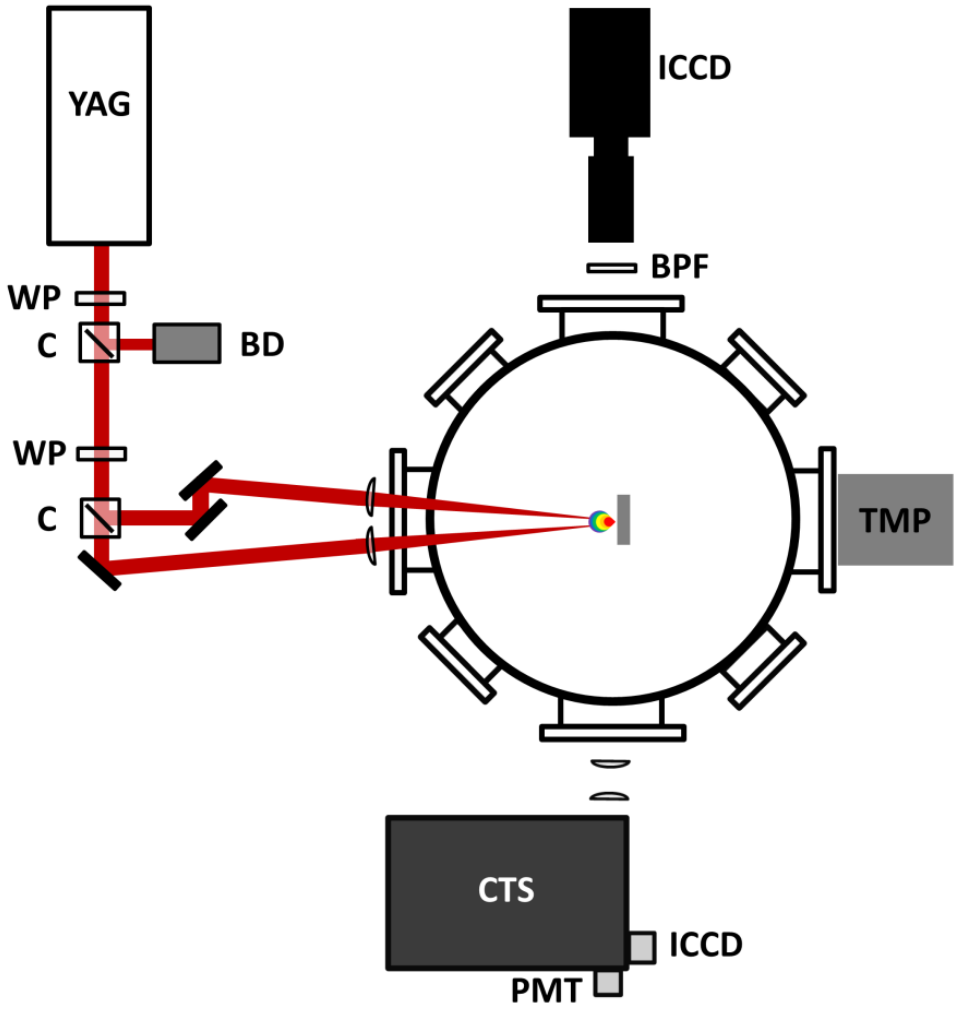

Figure 6.1 Experimental setup used in the study of colliding laser-produced carbon plasmas. Instrumentation used: Nd:YAG laser (YAG), Czerny-Turner spectrograph (spectrograph), intensified charge-coupled device (ICCD), turbomolecular pump (TMP), photomultiplier tube (PMT), bandpass filter (BPF), waveplate (WP), cube polarizer (C), beam dump (BD), and lenses (L).

Multiple diagnostic tools were used to investigate the developing laser-produced plasmas (LPP). Fast-photography of the colliding regime was captured using an intensified charge-coupled device (PI-MAX) configured with a Nikon optic for focusing. The ICCD is capable of capturing time-resolved (2 ns resolution) frames of the plume development with great temporal precision. By placing bandpass filters in front of the camera, a narrow bandwidth of spectral emissions may be selectively imaged. In this manner, particular emitting species within the plasma may be selectively observed, discriminating other contributing emission sources. Normally, the ICCD is most sensitive to emissions in the visible range (300-900 nm) and collects over this entire spectral range.

Using a Czerny-Turner spectrometer (Acton Sp-2500i), the ICCD may alternatively be used to capture the emission spectrum of our plasma. By design, light enters the spectrograph through a vertical entrance slit (20 μm wide). Appropriately, the analysis region of the plasma is a vertical cross section with line-integrated emission along the transverse horizontal component. By adjusting the two lenses which form a 1:1 telescope (which maps the plume image onto the entrance slit), different cross sections outbound from the target assembly may be analyzed. The Acton SP-2500i is also used as a monochromator. Light directed through an exit slit enters a photomultiplier tube (Hamamatsu R298) with an applied bias voltage of 1150 V. The optical time-of-flight signal is then registered by an oscilloscope. Timing settings were controlled using two programmable timing generators. One was dedicated to operating the flash lamps of the Nd:YAG laser at 10 Hz whereas the second timing generator was used to precisely trigger the Nd:YAG Q-switch and ICCD. Timing settings were monitored using 1 GHz oscilloscope.

6.3 Silicon and Carbon Colliding Plasma

The collision between silicon and carbon laser-produced plasma is considered presently. With a low laser intensity of 1×10^9 [W/cm^2], a rather mild ablation vaporizes material from the target surface, much below each's threshold for explosive boiling [82,83]. Since the two materials have unique ablation dependencies with laser fluence, the laser-material interaction (and laser-plasma interaction soon thereafter) of each will expectedly behave differently. Prominent emission lines from the various charge states of C and Si ion are shown in Table 6.1 which also includes each's ionization energy (if applicable). Ionization energy plays an important role in the evolution of the laser-plasma during its nascent formation over the course of the laser pulse and thereafter during the ensuing plume devolvement and plasma collision.

Table 6.1 Prominent Transitions and Ionization Energies for C and Si

Species	Wavelength [nm]	Transition	Ionization Energy [eV]
C(I)	247.9*	$2s^2 2p 3s$-$2s^2 2p^2$	-
C(II)	392.1 426.7*	$2s^2 4s$-$2s^2 3p$ $2s^2 4f$-$2s^2 3d$	11.3
C(III)	464.7*	$1s^2 2s 3p$-$1s^2 2s 3s$	24.4
Si(I)	390.6*	$3s^2 3p 4s$-$3s^2 3p^2$	-
Si(II)	385.6 413.1* 505.6	$3s^2 4p$-$3s 3p^2$ $3s^2 4f$-$3s^2 3d$ $3s^2 4d$-$3s^2 4p$	8.2
Si(III)	380.7 455.3* 482.9	3s4d-3s4p 3s4p-3s4s 3s5g-3s4f	16.3
Si(IV)	376.2 408.9	$2p^6 5p$-$2p^6 4d$ $2p^6 4p$-$2p^6 4s$	33.5
C_2	~468 ~516	$d^3\Pi_g \rightarrow a^3\Pi_u$	-

*used for OTOF in Figure 6.5

6.3.1 Fast-gated Plume Imaging

The collision between the carbon and silicon plasmas can be seen in Figure 6.2. The initial formation of the stagnation layer is seemingly quite similar to what was seen in previous chapters. Starting at around 200 ns, it becomes quite apparent that the stagnation layer drifts downwards, ultimately striking the bottom Si surface. This behavior can be effectively described using the plume hydrodynamic descriptions provided in Chapter 3. Colliding plasmas were explored while varying the laser intensity used to create seed plasma. It was concluded that higher laser intensity resulted in enhanced laser-plasma interaction. Consequently, the nascent plasma developed a higher electron temperature sooner. Once the laser encounters the critical electron density, it is reflected, shielding the material surface from further direct laser irradiation in a process referred to as laser-plasma interaction (LPI). The peripheral plasma is ejected as a hot blowoff of multicharged ions while the cold, dense near-surface plasma continues to erode the material via its own intense radiation and thermal contact with the target surface. With lower laser intensity, LPI occurs later such that less energy is deposited to the peripheral plasma. This results in a less violent early expansion of the seed plume.

In Figure 6.2, the two variants of plume expansion play out in the development of the colliding plasma regime. At 50 ns, it is seen that the Si plasma is more energetic. By 125 ns, it appears as though the Si seed plasma has expunged all ablated material and therefore ceases to exert hydrodynamic pressure. The C seed plasma continues to exert pressure from the top, pushing the stagnation layer downward. This effect plays out for several hundred nanoseconds following the initial seed plasma creation. For equal laser intensities being imparted to each material surface, it makes intuitive sense that the Si plasma will rarify more rapidly. We realize that Si is much more readily ionized than C since Si features much lower ionization energies.

Therefore, Si plasma more quickly established a high electron density which expedites the onset of LPI.

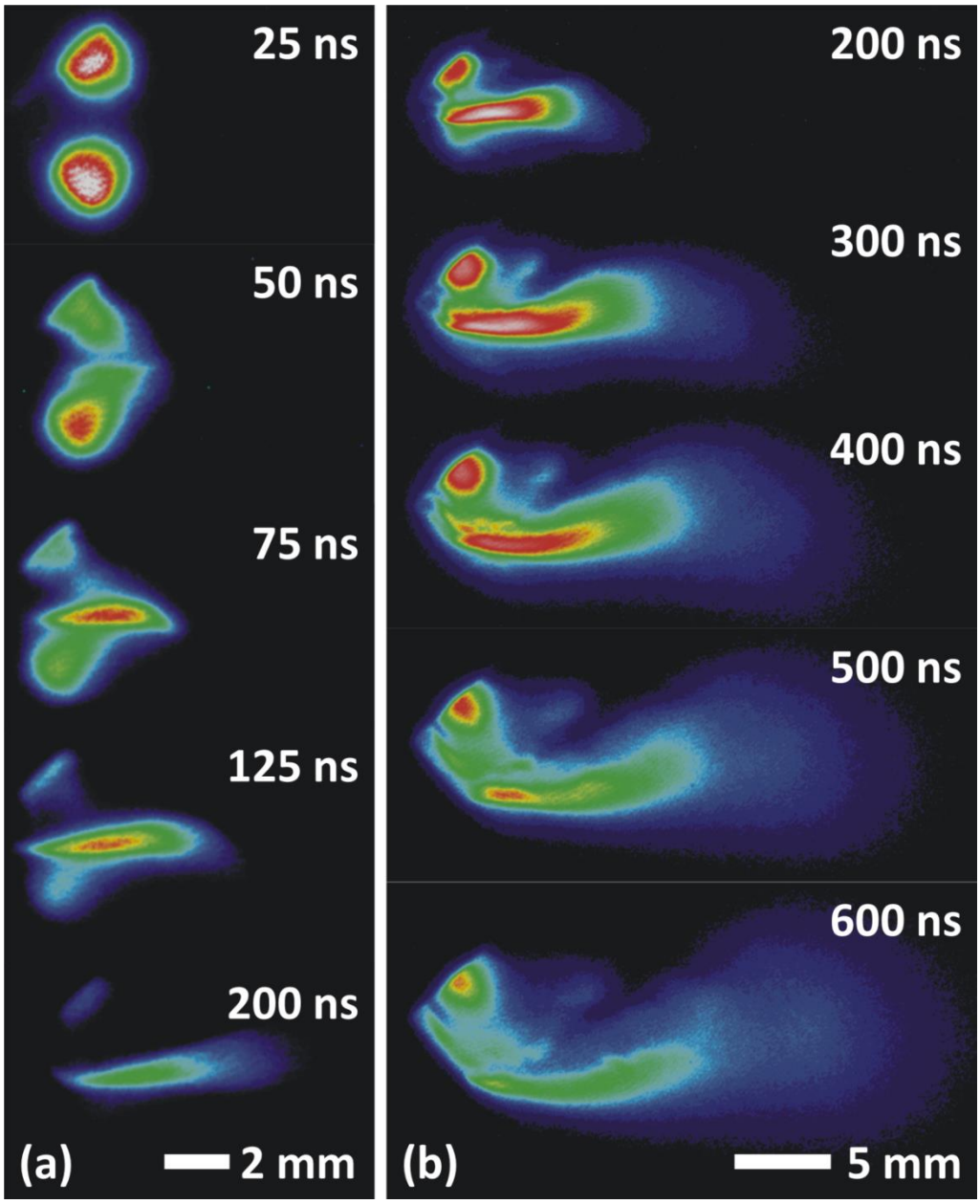

Figure 6.2 Plume imaging of the collision between C (top face) and Si (bottom face) laser-produced plasma generated from 1×10^9 [W-cm^2] laser irradiation shown using a nonlinear color scale showing (a) time-resolved imaging over the first 200 ns; (b) the ensuing behavior of the stagnation layer from 200-600 ns.

6.3.2 Optical Emission Spectroscopy

The atomic composition of the stagnation layer was analyzed using optical emission spectroscopy (OES). Spectra from cross sections of the stagnation layer were individually taken over a range up to 20 mm outbound from the plane where both seed plasmas were initially created. Normalized time-integrated spectra for three such cross sections are shown in Figure 6.3 with the exposure beginning 100 ns after laser incidence. Prominent emission lines from the most abundant species are given in Table 6.1. The three spectra are largely similar but each contains unique information pertaining to the region where they were collected. At the x = 0 mm plane, Swan band emission is observed due to the presence of C_2 dimers. The presence of C_2 is restricted to nearby the graphite surface and does not appear in appreciable quantity within the stagnation layer. C_2 did not appear farther out in the colliding plasma regime. The greatest emission within the stagnation layer appears at a distance approximately 3 mm outbound from the seed plasma. In this region, emission from doubly-charged states of both Si (455.3 nm) and C (464.7 nm) is observed which is perhaps surprising considering the low laser intensity used for target ablation. At the farthest observed location (x = 13 mm), the emission from doubly charged species has diminished while emission from neutrals remain substantial.

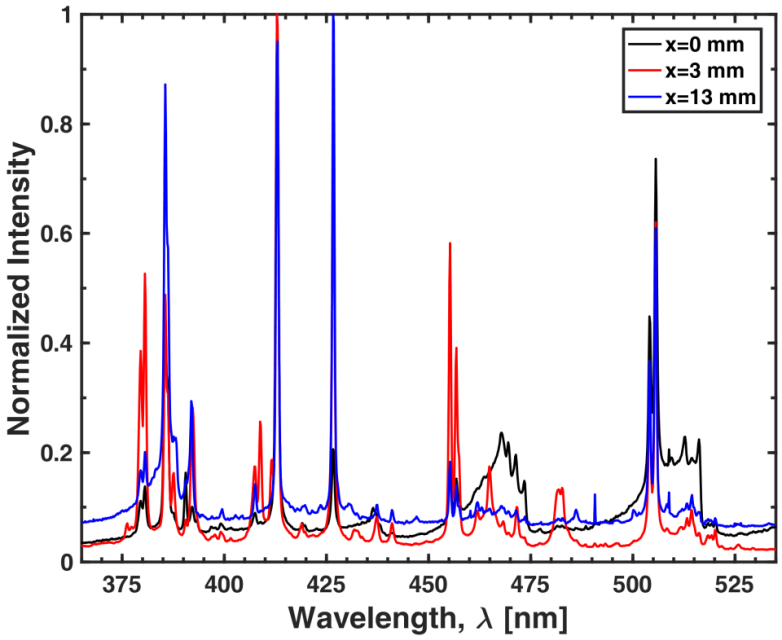

Figure 6.3 Normalized emission spectra for three cross sections of the stagnation layer formed between colliding C and Si seed plasma using a 1 μs exposure

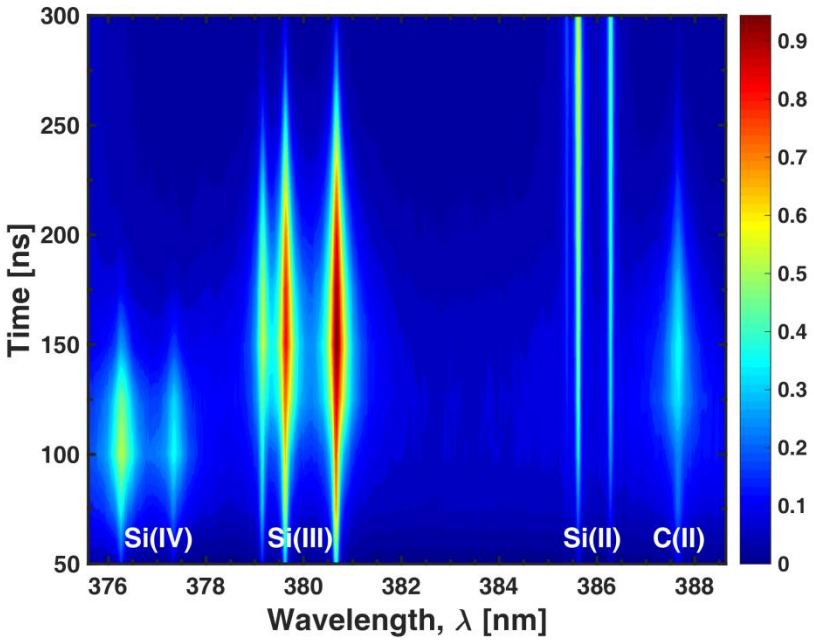

Figure 6.4 Time-resolved, wavelength-dispersed plot of the logarithm of SBR for the collision between Si and C plasma 3 mm outbound from the seed plasma

Time-resolved emission spectra from 50-300 ns were taken at the x = 3 mm distance in order to observe the stagnation layer onset and ionization stages during early development. Successive spectra were collected in 25 ns increments (beginning at 50 ns) with ±10 ns time resolution. A relatively small spectral window (375-390 nm) was chosen since it provides a rich locus of C(II), Si(II), Si(III), and even Si(IV) lines. Figure 6.4 shows the concatenation of time-resolved spectra constructing a wavelength-dispersed, time-resolved plot. Spectra were integrated over the entire width of the stagnation layer. This tended to underrepresent the intensity of the highly charged Si(IV) ion since it only occupied a thin region at the core of the stagnation layer. Color values indicate the logarithm of the signal-to-background ratio (SBR). The low SBR is completely reasonable since we expect considerable continuum emission in the stagnation layer though the background could increase by virtue of using time-resolved spectra which inherently adds background noise.

Different ionization stages of constituent species within the plasma are shown in Figure 6.4. From Figure 6.2(a), we recall that the onset of stagnation occurs at approximately 75 ns. This appears to be evidenced here as well. Furthermore, we observe that significant emission originates from Si(IV) species from 50-150 ns. Si(III) ions preside from 100-225 ns while Si(II) occurs at all time but increases steadily over the considered time domain. The reduction in ionization stage is quite expected though the occurrence of Si(IV) while using such a low laser intensity is somewhat unforeseen. However, Si(IV) observed at 100 ns was highly localized at the center of the stagnation layer which indicates hard stagnation of already present Si(IV) ions or that the induced stagnation could promote Si(III) to a higher charge state. Peak emergence of C(II) is caught sometime between appearances of Si(IV) and Si(III) from around 100-200 ns. The shorter lifetime of C(II) than its Si(II) counterpart may be explained by its higher ionization

energy (11.26 eV vs. 8.15 eV). However, the temporal separation is perhaps too pronounced for this explanation alone to suffice. After all, the Si(III) population appears to peak slightly later than that from C(II), yet its ionization is considerably higher (16.35 eV) and the upper energy level of the observed transitions is higher still (25.0 eV), greater even than carbon's second ionization energy (24.4 eV). From this, we can surmise that the Si and C populations possess different temperatures (the Si plasma being hotter). We had hypothesized previously that the Si seed plasma experiences greater laser-plasma interaction which would cause a hotter ejecta of Si ions. This observation, originally made by assessing the seed plume kinetics, is now further substantiated alternatively from a spectroscopic interpretation.

One might be tempted to absolutely proclaim the ratio between populations of the successive ionization stages simply by comparing relative signal intensities (colors) of the various lines. This is cautioned against since the lines are weighted by their respective oscillator strength among other distinctions. Recalling that emission is spatially integrated across the width of the stagnation layer (4.9 mm to be exact), highly localized emission (viz. Si(IV)) becomes muted upon integrating the background signal over the entire region. However, the relative preponderance of each ionization stage can be tracked in relation to its own occurrence at different moments of time during the plasma evolution. With improved spatial resolution (while maintain adequate time-resolution), it would be possible to discern how plasma temperature varies along the gradient between the energetically dissimilar carbon and silicon plasmas.

6.3.3 Optical Time-of-flight

Optical emission spectroscopy was complemented by the addition of optical time-of-flight (OTOF) data which provides the temporal evolution of the colliding plasma regime. Using the Acton SP-2500i as a monochromator, time-of-flight of a preselected line transition was acquired using a photomultiplier tube. The OTOF profiles of neutral, singly-charged, and doubly-charged C and Si obtained from 0 to 20 mm outbound from the seed-plume-containing plane were used to create the space-time OTOF contours shown in Figure 6.5. Line transitions used for OTOF data acquisition are indicated in Table 6.1.

OTOF data shows that C(III) is short-lived, diminishing within 200 ns of plume development. Si(III) presides for a much greater duration (~800 ns) than its C(III) counterpart, having a 8.8 eV lower ionization threshold. We observed earlier that the temperature of the carbon and silicon populations were unequal within the first 200 ns. It isn't clear when they reach equilibrium or the degree of intermixing between the C and Si plasmas at such time. Further study is required to discern the degree of intermixing of the two plasmas.

The population of neutral of both C and Si exhibited a slower development occurring over the duration of several microseconds. Si(I) species are observed farther out which most likely can be explained by the higher degree of interpenetration by the Si plasma. An increased local amount of S(I) is observed at about x = 1.3 cm. Looking at Figure 6.2, this appears to be the end of the stagnation layer though it remains unclear how Si(I) appears in such large quantity in this region following 1 μs.

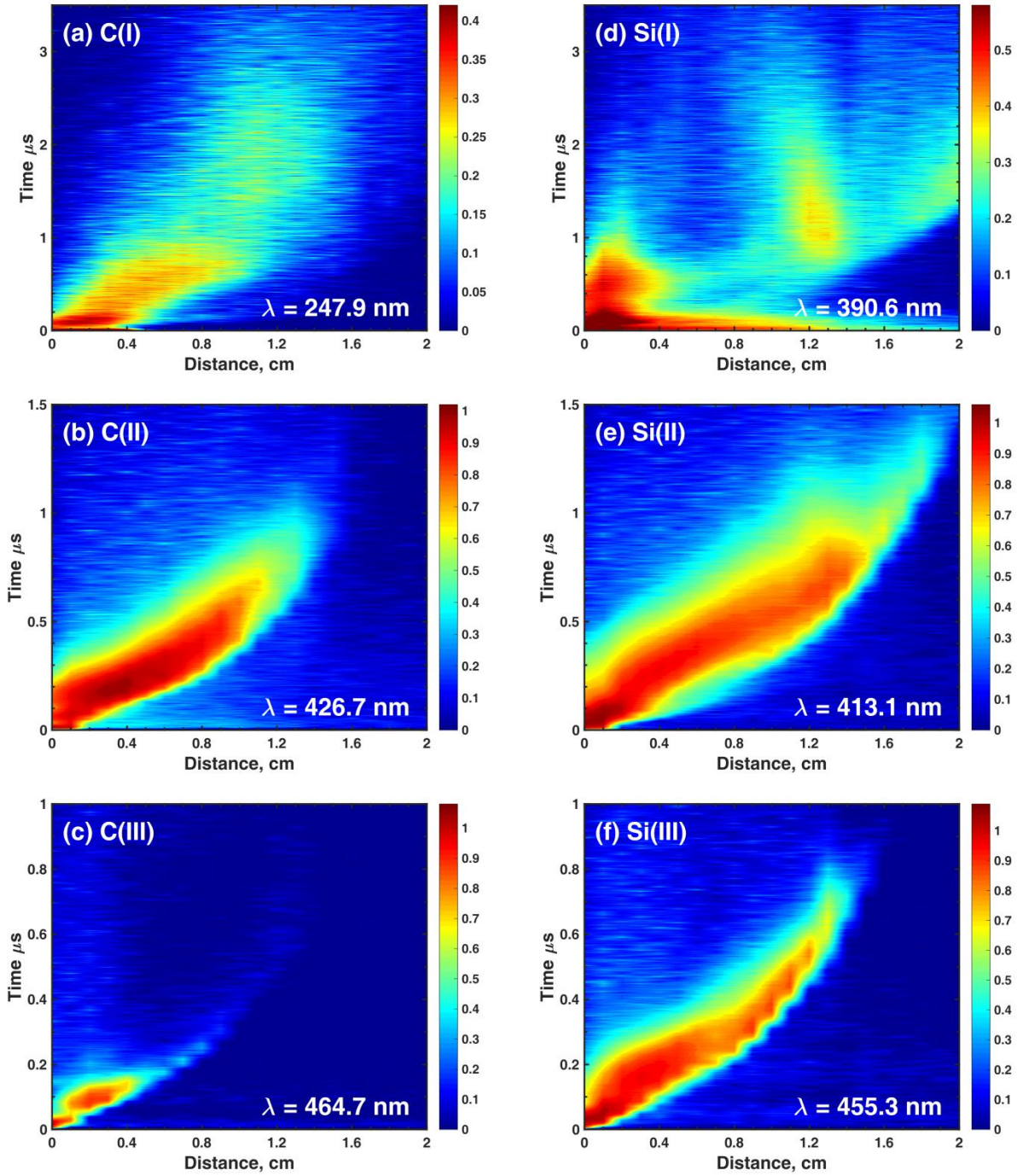

Figure 6.5 Space-time contours of (a) C neutrals, (b) C^{1+} ions, (c) C^{2+} ions, (d) Si neutrals, (e) Si^{1+} ions, and (f) Si^{2+} ions generated from optical time-of-flight profiles along the stagnation layer. At x = 0 mm, the slit is positioned atop both seed plumes.

6.4 Conclusions

Colliding plasma from carbon and silicon feature asymmetry along the collision midplane which was studied. The collision was studied via fast-gated plume imaging, optical emission spectroscopy, and optical time-of-flight. The asymmetry was immediately apparent in the laser ablation of each surface. We surmised that well-developed laser plasma interaction is more quickly established in the case of Si target since its lower ionization threshold allows a free electron population to more quickly manifest. The consequence was contrasting laser-plasma coupling for the two plasmas which led to creation of two plasmas with quite different plume kinetics. The time-dependent imbalance of the imposed seed plume pressure on the stagnation layer led to the pronounced drift of the layer away from the collision midplane (towards the Si surface). Additionally, the Si population possessed considerably higher electron temperature. The possibility of being able to tailor plasma parameters for both C and Si populations could offer unique advantages when attempting SiC synthesis via this approach.

7. SUMMARY AND RECOMMENDATIONS

7.1 Summary

The main objective of this dissertation was to further knowledge of prevailing physics and chemistry of colliding laser-produced plasmas and to discuss their application to inertial fusion energy (IFE) chamber design and extreme ultraviolet (EUV) source development for next-generation nanolithography tools. Harnessing controlled nuclear fusion for commercial energy production is one of the most prolific science topics of our generation. The promise of fusion is obvious: a virtually nondepletable source of green renewable energy. Multiple approaches are being explored in parallel, each requiring an array of expertise ranging across many fields of physics, chemistry, and technology to realize a complete design. In the IFE approach, high-energy density physics is used to understand the implosion and ensuing thermonuclear ignition of the fusion fuel. The chamber design must accommodate radiation and thermal loadings on the first wall for each shot during cyclical operation.

In Chapters 3 and 4, the collision of two carbon laser-produced plasmas was investigated using empirical approaches which were compared with computational modeling. In the first of these two chapters, the plume evolution of both seed plasmas and the stagnation layer were investigated using different laser intensities. With higher laser intensity, it was observed that greater laser-plasma interaction occurred between the laser pulse and the nascent seed plasma over the 6 ns pulse duration. As a result, the seed plasma rarefied much more quickly, casting off hot ions from the periphery of the critical electron density isobar. Upon using the lower laser intensity, the seed plume expansion was more gradual. Both cases would produce a stagnation layer, but greater interpenetration was reported when using greater laser intensity. When using

lower laser intensity, the slow-moving inventory of ablated material continued to supply material to the stagnation layer. In addition to accumulating more material along the collision midplane, continual hydrodynamic pressure was being exerted by each seed plume provided temporary pressure confinement. At a certain point, C_2 dimers appeared in the stagnation layer. This moment corresponded to the arrival of carbon neutrals in the stagnation layer, suggesting that C_2 was being produced via the dimerization of these species. These mechanics were observed and ascertained using fast imaging and optical emission spectroscopy in tandem with HEIGHTS computational modeling.

Molecular formation of C_2 in colliding carbon plasma was explored further with the addition of C_3 trimers in Chapter 4. The stagnation layer was studied over a longer period of 5 μs using laser-induced fluorescence (LIF) and optical time-of-flight (OTOF). By performing LIF on the molecular Swan and Swing bands of C_2 and C_3 respectively, the occurrence of each was tracked in the development of the stagnation layer. We determined that C_3 was being introduced into the colliding plasma regime prior to synthesis within the stagnation layer at later time ($\gtrapprox$ 500 ns) via the dissociation of larger carbon molecules liberated ab initio from the target surface during ablation. C_2 did not appear in this manner, a fact which we attributed to its higher dissociation energy. OTOF performed on the stagnation layer reinforced the notion of delayed synthesis of C_2 (especially upon comparison with OTOF space-time contours of atomic forms of carbon). LIF was performed on an individual seed plasma to provide a control comparison. The results reinforced our interpretation. HEIGHTS computational modeling provided further characterization of the developed stagnation layer, describing the plasma electron temperature as suitable for molecular formation of C_2.

In Chapter 5, colliding tin plasma was explored with interest in creating an efficient EUV source with high power output. Current exposure tools used in photolithography make use of ArF excimer laser deep ultraviolet (DUV) light sources (λ = 193 nm). While these tools have served the semiconductor industry well, next-generation nanolithography tools will require a shorter wavelength of light to achieve the smallest feature sizes. EUV sources should possess high spectral purity with high conversion efficiency of light into usable in-band EUV (13.5 nm ± 2%): laser-produced Sn plasmas have been chosen to fulfill this purpose. Presently, colliding Sn plasma was performed to construct a "pre-plasma" which may be optimally coupled with another laser pulse to efficiently produce EUV light. Experimentally, EUV emission measured using an AXUV photodiode (with a Mo/Si mirror and two Zr filters to ensure spectral purity). The empirical results corresponded well with HEIGHTS computational modeling. HEIGHTS was used additionally to predict the EUV output upon introducing a CO_2 laser to reheat the plasma for improved EUV power output and source conversion efficiency. 12 mJ of usable EUV (collect in π sr) was reported for each run. Assuming 100 kHz laser operation (and 60% mirror reflectivity), this could offer 700 W of usable, in-band EUV power.

Lastly, Chapter 6 investigated colliding plasmas which feature asymmetry along the collision midplane. Until now, the two seed plasmas used in the formation of the stagnation layer were identical, having the same laser intensity and consisting of the same elemental composition. Here, the collision of carbon and silicon laser-produced plasmas was studied via fast-gated plume imaging, optical emission spectroscopy, and optical time-of-flight. The asymmetry was immediately apparent in the laser ablation of each surface. We surmised that the well-developed laser plasma interaction is more quickly established in the case of Si target since its lower ionization threshold allows a free electron population to more quickly manifest. The

consequence was contrasting laser-plasma coupling for the two plasmas which led to creation of two plasmas with quite different plume hydrodynamics. The time-dependent imbalance of the imposed seed plume pressure on the stagnation layer led to the pronounced drift of the layer away from the collision midplane (towards the Si surface)

7.2 Recommendations

This body of work is extensive in its exploration of colliding plasmas with attention to how they pertain to such applications as chamber design for commercial fusion energy and EUV source development for next-generation photolithography. However, these topics are abundant with research opportunity and therefore may benefit from further academic contribution. In the following section, possible research ventures will be suggested which could be conducted using CMUXE's current facilities and capabilities.

7.2.1 Collection of Carbon Macromolecules

Investigation of colliding carbon plasma for inertial fusion energy chamber physics is primarily motivated by the question: will carbon macromolecules form? More precisely, our interest is whether large carbon molecules will occupy the IFE chamber in sufficient quantity such that shot performance is reduced during standard cyclical operation (i.e. due to reduced drive laser-hohlraum coupling). The work presented in this dissertation evaluated the formation of carbon precursors (C_2 and C_3) to larger carbon clusters whereas other literature has reported carbon nanotube production for a particular set of conditions and geometry [20]. However, these studies could feature greater fidelity to anticipated IFE chamber conditions. For an IFE chamber

with 6 m radius and 2 Torr Xe background, it is most likely that gas collisions would prevail before evaporated wall material fully converges at the chamber center (the mean free path is much shorter than the chamber radius). Colliding plasma regimes would exist closer to the wall, but such schemes would fail to adequately describe chamber-center conditions.

The progression pathway for large macromolecule formation of carbon entails the chaining of carbon precursors into carbon chains. The carbon chains then self-assemble into clusters which contaminate the chamber. Cluster formation can be confirmed with particle collection techniques by using a witness plate. Ex-situ methods of characterization such as scanning electron microscopy (SEM) and x-ray photoelectron spectroscopy (XPS) may be used to confirm production, provide cluster size estimation, and to discern elemental composition. Additionally, in-situ study of the cluster-forming plasma may be approached using laser-induced incandescence (LII).

7.2.2 Role of Laser Wavelength on Molecule Formation in Colliding Carbon Plasma

Inertial fusion energy designs typically employ third harmonic (3ω) Nd:YAG laser pulses ($\lambda = 355$ nm) to drive pellet implosion since the lower wavelength features better coupling with the target hohlraum or ablator. While the byproducts of each shot produce a tremendous yield of x-rays and ions, the majority of this energy would be absorbed by the proposed low pressure (~2 Torr) Xe ambient [83]. The majority of pulsed energy being deposited onto the first wall actually arrives as uncoupled 3ω laser light. The laser wavelength affects the laser interaction with the graphite material, producing a different inventory of ablated species (while also affecting plume hydrodynamics). For instance, it is expected that a higher percentage of evaporated material will exist in as neutral species due to lower laser-plasma interaction. C_2 and

C_3 formation in colliding plasma under these irradiation and pressure conditions should be studied.

A 3ω laser pulse from the Quantel Nd:YAG laser (housed within the Radiant HE 355 LD tunable laser) may be picked off prior to entering the optical parametric oscillator by inserting a mirror along the beam path. The diverted beam exits a side port of the tunable laser enclosure and may then be directed to the vacuum chamber. This is obviously prohibitive in that it discounts the possibility of using the tunable laser for LIF or for other spectroscopic analysis techniques. Alternatively, 2ω and 4ω outputs (using harmonic-generation crystals) from the Continuum Surelite III laser may be used which would then permit the tunable laser to be used for spectrochemical analysis and would permit a greater parameter range for the study.

7.2.3 Induced Plasma Collisionality: from Vacuum to Low-pressure Gas Ambient

In laser-produced plasmas formed in the presence of an ambient gas, the plume expands until the plume front encounters a pressure boundary which stalls continued expansion. The number of collisions increases, especially at the plume front. In colliding plasmas, collisionality is induced along the stagnation layer in the absence of an ambient gas. While colliding plasma regimes may present in vacuum environments (e.g. interstellar space), situations exist where induced collisionality may be partially caused both by contributions from interaction with the gas ambient and from the hard stagnation of colliding plasmas. Laser inertial fusion energy designs feature a low pressure of ambient Xe gas (~2 Torr) to lessen the radiation load delivered to the chamber wall [83]. At this pressure, both mechanisms of induced collisionality should be important. Studying colliding plasma at pressures where this transition takes place (roughly

between 0.1 and 10 Torr) would offer valuable insight into scenarios where both mechanisms should be simultaneously considered.

In addition to studying colliding plasma for a range of gas pressures, it would be informative to include study of different types of gas ambient. While fusion reactor designs call for the use of Xe, using Xe in lab is prohibitively expensive. He and Ar are reasonable alternatives for fundamental physics studies seeking to ascertain the importance of atomic mass of the gas species. Time-integrated, spatially-resolved electron temperature and density of the stagnation layer could be compared with values likewise obtained from individual laser-produced plasma. Fast-gated plume imaging and HEIGHTS computational modeling would provide complementary insight.

7.2.4 Parametric Study of Colliding Sn Plasma for a High-power EUV Source

The implementation of colliding Sn plasma to create an ideal preplasma while simultaneously optimizing the CO_2 laser coupling is inherently a multivariate endeavor. Different system parameters should be adjusted to realize the best source. For instance, reducing Nd:YAG laser intensity may reduce seed plasma interpenetration, leading to harder plume stagnation. Other parameters to consider chiefly pertain to CO_2 laser reheat. The focal spot can be positioned at various locations along the stagnation layer with varying spot size. The latter is particularly interesting due to the notable mass density gradient transverse to the stagnation layer plane. Lastly, the interpulse delay between the Nd:YAG laser and CO_2 laser can be changed with consideration for the spatiotemporal evolution of the stagnation layer. An important aspect of designing a EUV source is debris mitigation. Ion time-of-flight data should be studied to

evaluate the ion energy spectrum altered due to ion screening (similar to [38]). Cluster formation in the stagnation layer would also be studied to discern weather there is any notable increase.

REFERENCES

[1] U. S. Inan and M. Golkowski, *Principles of Plasma Physics for Engineers and Scientists*. Cambridge: Cambridge University Press, 2011.

[2] M. N. Saha, “LIII. Ionization in the solar chromosphere,” *London, Edinburgh, Dublin Philos. Mag. J. Sci.*, vol. 40, no. 238, pp. 472–488, 1920.

[3] C. S. Aké, R. S. De Castro, H. Sobral, and M. Villagrán-Muniz, “Plume dynamics of cross-beam pulsed-laser ablation of graphite,” *J. Appl. Phys.*, vol. 100, no. 5, 2006.

[4] J. Dardis and J. T. Costello, “Stagnation layers at the collision front between two laser-induced plasmas: A study using time-resolved imaging and spectroscopy,” *Spectrochim. Acta - Part B At. Spectrosc.*, vol. 65, no. 8, pp. 627–635, 2010.

[5] S. L. Gupta, P. K. Pandey, R. K. Thareja, S. L. Gupta, P. K. Pandey, and R. K. Thareja, “Dynamics of laser ablated colliding plumes,” vol. 013511, no. January, pp. 1–10, 2013.

[6] K. F. Al-Shboul *et al.*, “Interpenetration and stagnation in colliding laser plasmas,” *Phys. Plasmas*, vol. 21, no. 1, pp. 1–8, 2014.

[7] P. W. Rambo and J. Denavit, “Interpenetration and ion separation in colliding plasmas,” *Phys. Plasmas*, vol. 1, no. 12, pp. 4050–4060, 1994.

[8] E. Irissou, F. Vidal, T. Johnston, M. Chaker, D. Guay, and A. N. Ryabinin, “Influence of an inert background gas on bimetallic cross-beam pulsed laser deposition,” *J. Appl. Phys.*, vol. 99, no. 3, pp. 1–15, 2006.

[9] N. C. Woolsey *et al.*, “Collisionless shock and supernova remnant simulations on VULCAN,” *Cit. Phys. Plasmas*, vol. 8, 2001.

[10] D. Mascali *et al.*, “Colliding laser-produced plasmas: A new tool for nuclear astrophysics studies,” *Radiat. Eff. Defects Solids*, vol. 165, no. 6–10, pp. 730–736, 2010.

[11] S. L. Ivanovski, A. Bonanno, S. Tudisco, N. Gambino, and D. Mascali, “Plasma astrophysics and laser experiments: Hydrodynamical simulation of colliding plasmas,” *Radiat. Eff. Defects Solids*, vol. 165, no. 6–10, pp. 457–462, 2010.

[12] J. Ross *et al.*, “High-Density Carbon Ablator Experiments on the National Ignition Facility,” *Bull. Am. Phys. Soc.*, vol. 58, pp. 1–12, 2013.

[13] T. R. Dittrich *et al.*, “Review of indirect-drive ignition design options for the National Ignition Facility,” *Phys. Plasmas*, vol. 6, no. 5, p. 2164, 1999.

[14] R. W. Moir, “HYLIFE-II Inertial Confinement Fusion Power Plant Design,” *Part. Accel.*, vol. 37–38, pp. 467–480, 1992.

[15] W. R. Meier, “Osiris and SOMBRERO inertial fusion power plant designs - summary, conclusions, and recommendations,” *Fusion Eng. Des.*, vol. 25, pp. 145–157, 1994.

[16] T. J. Renk *et al.*, “IFE chamber dry wall materials response to pulsed X-rays and ions at power-plant level fluences,” *Fusion Eng. Des.*, vol. 65, pp. 399–406, 2003.

[17] R. W. Moir, “The logic behind thick, liquid-walled, fusion concepts,” *Fusion Eng. Des.*, vol. 29, no. C, pp. 34–42, 1995.

[18] “IFE chamber walls: requirements, design options, and synergy with MFE plasma facing components,” *J. Nucl. Mater.*, vol. 313–316, pp. 23–31, Mar. 2003.

[19] Y. Hirooka, T. Oishi, H. Sato, and K. A. Tanaka, “Aerosol formation and hydrogen co-deposition by colliding ablation plasma plumes of carbon,” *Fusion Sci. Technol.*, vol. 60, no. 2, pp. 804–808, 2011.

[20] Y. Hirooka, H. Sato, K. Ishihara, T. Yabuuchi, and K. a. Tanaka, “Formation of carbon allotrope aerosol by colliding plasmas in an inertial fusion reactor,” *Nucl. Fusion*, vol. 54, no. 2, p. 022003, 2014.

[21] N. Konjević, A. Lesage, J. R. Fuhr, and W. L. Wiese, “Experimental Stark Widths and Shifts for Spectral Lines of Neutral and Ionized Atoms (A Critical Review of Selected Data for the Period 1989 Through 2000),” *J. Phys. Chem. Ref. Data*, vol. 31, no. 819, pp. 819–927, 2002.

[22] H. Griem, *Principles of Plasma Spectroscopy*. Cambridge: Cambridge University Press, 1997.

[23] G. Bekefi, *Principles of laser plasmas*. New York: Wiley, 1976.

[24] J. G. Haub, R. M. Hentschel, M. J. Johnson, and B. J. Orr, “Controlling the performance of a pulsed optical parametric oscillator: a survey of techniques and spectroscopic applications,” *J. Opt. Soc. Am. B*, vol. 12, no. 11, p. 2128, 1995.

[25] V. Sizyuk, A. Hassanein, V. Morozov, V. Tolkach, T. Sizyuk, and B. Rice, “Numerical simulation of laser-produced plasma devices for EUV lithography using the heights integrated model,” *Numer. Heat Transf. Part A Appl.*, vol. 49, no. 3, pp. 215–236, 2006.

[26] V. Sizyuk, A. Hassanein, and T. Sizyuk, “Three-dimensional simulation of laser-produced plasma for extreme ultraviolet lithography applications,” *J. Appl. Phys.*, vol. 100, p. 103106, 2006.

[27] V. Tolkach, V. Morozov, and A. Hassanein, “Development of Comprehensive Models for Opacities and Radiation Transport for IFE Systems,” 2002.

[28] V. Sizyuk, A. Hassanein, V. Morozov, and T. Sizyuk, “Heights Integrated Model as Instrument for Simulation of Hydrodynamic , Radiation Transport , and Heat Conduction Phenomena of Laser-Produced Plasma in EUV Applications,” 2006.

[29] H. W. Kroto, J. R. Heath, S. C. O’Brien, R. F. Curl, and R. E. Smalley, “C_{60}: buckminsterfullerene,” *Nature*, vol. 318, pp. 162–163, 1985.

[30] A. W. Miziolek, V. Palleschi, and I. Schechter, Eds., *Laser-Induced Breakdown Spectroscopy (LIBS)*. Cambridge: Cambridge University Press, 2006.

[31] C. G. Morgan, “Laser-induced breakdown of gases,” *Reports Prog. Phys.*, vol. 38, no. 5, pp. 621–665, 1975.

[32] A. A. Bol’shakov, J. H. Yoo, C. Liu, J. R. Plumer, and R. E. Russo, “Laser-induced breakdown spectroscopy in industrial and security applications,” *Appl. Opt.*, vol. 49, no. 13, p. C132, 2010.

[33] A. A. Bol’shakov, X. Mao, J. J. González, and R. E. Russo, “Laser ablation molecular isotopic spectrometry (LAMIS): current state of the art,” *J. Anal. At. Spectrom.*, vol. 31, no. 1, pp. 119–134, 2016.

[34] K. F. Al-Shboul, S. M. Hassan, and S. S. Harilal, “Molecular formation in the stagnation region of colliding laser-produced plasmas,” *Plasma Sources Sci. Technol.*, vol. 25, 2016.

[35] S. S. Harilal, R. C. Issac, C. V. Bindhu, V. P. N. Nampoori, and C. P. G. Vallabhan, “Time resolved analysis of C2 emission from laser induced graphite plasma in helium atmosphere,” *Japanese J. Appl. Physics, Part 1 Regul. Pap. Short Notes Rev. Pap.*, vol. 36, no. 1 A, pp. 134–138, 1997.

[36] H. Luna, K. D. Kavanagh, and J. T. Costello, “Study of a colliding laser-produced plasma by analysis of time-and space-resolved image spectra,” *J. Appl. Phys. J. Appl. Phys. Phys. Plasmas Phys. Plasmas J. Appl. Phys.*, vol. 101, no. 101, pp. 33302–13502, 2007.

[37] D. D. Ryutov, N. L. Kugland, M. C. Levy, C. Plechaty, J. S. Ross, and H. S. Park, "Magnetic field advection in two interpenetrating plasma streams," *Phys. Plasmas*, vol. 20, no. 3, pp. 1–11, 2013.

[38] P. Hough *et al.*, "Ion emission in collisions between two laser-produced plasmas," *J. Phys. D. Appl. Phys.*, vol. 44, no. 35, p. 355203, 2011.

[39] R. P. Singh, S. L. Gupta, and R. K. Thareja, "Time resolved diagnostics of ions in colliding carbon plasmas," *J. Appl. Phys.*, vol. 116, 2014.

[40] M. E. Geusic, M. F. Jarrold, T. J. Mcilrath, R. R. Freeman, and W. L. Brown, "Photodissociation of carbon cluster cations," *J. Chem. Phys.*, vol. 86, no. 7, pp. 3862–3869, 1987.

[41] Z. Cao, M. Muhlhauser, M. Hanrath, and S. D. Peyerimhoff, "Study of possible photodissociation channels in linear carbon clusters C_n (n = 4-6)†," *Chem. Phys. Lett.*, vol. 351, pp. 327–334, 2002.

[42] K. Lykke and P. Wurz, "Direct Detection of Neutral Products from Photodissociated C_{60}," *J. Phys. Chem*, vol. 96, pp. 3191–3193, 1992.

[43] P. Wurz and K. R. Lykke, "Kinetics of multiphoton excitation and fragmentation of C_{60}," *The Journal of Chemical Physics*, vol. 184. pp. 335–346, 1994.

[44] S. Irle, G. Zheng, M. Elstner, and K. Morokuma, "From C_2 Molecules to Self-Assembled Fullerenes in Quantum Chemical Molecular Dynamics," *Nano Lett.*, vol. 3, no. 12, pp. 1657–1664, 2003.

[45] J. F. Latkowski *et al.*, "Chamber Design for the Laser Inertial Fusion Energy (LIFE) Engine," 2010.

[46] A. A. Puretzky, D. B. Geohegan, X. Fan, and S. J. Pennycook, "Dynamics of single-wall carbon nanotube synthesis by laser vaporization," *Appl. Phys. A Mater. Sci. Process.*, vol. 70, no. 2, pp. 153–160, 2000.

[47] S. Arepalli, P. Nikolaev, W. Holmes, and C. D. Scott, "Diagnostics of laser-produced plume under carbon nanotube growth conditions," *Appl. Phys. A Mater. Sci. Process.*, vol. 70, no. 2, pp. 125–133, 2000.

[48] G. E. Moore, "Progress in Dıgital Integrated," *Electron Devices Meet. 1975 Int.*, vol. 21, pp. 11–13, 1975.

[49] M. Rothschild *et al.*, “Recent trends in optical lithography,” *Lincoln Lab. J.*, vol. 14, no. 2, pp. 221–236, 2003.

[50] A. A. Schafgans *et al.*, “Performance optimization of MOPA pre-pulse LPP light source,” no. March 2015, p. 94220B, 2015.

[51] D. T. Elg, J. R. Sporre, G. A. Panici, S. N. Srivastava, and D. N. Ruzic, “*In situ* collector cleaning and extreme ultraviolet reflectivity restoration by hydrogen plasma for extreme ultraviolet sources,” *J. Vac. Sci. Technol. A Vacuum, Surfaces, Film.*, vol. 34, no. 2, p. 021305, 2016.

[52] D. G. Stearns, R. S. Rosen, and S. P. Vernon, “Multilayer mirror technology for soft-x-ray projection lithography,” *Appl. Opt.*, vol. 32, no. 34, pp. 6952–60, 1993.

[53] H. Komori, G. Soumagne, H. Hoshino, T. Abe, and T. Suganuma, “Ion damage analysis on EUV collector mirrors,” vol. 5374, no. May 2004, pp. 839–846, 2004.

[54] B. a M. Hansson *et al.*, “Status of the liquid-xenon-jet laser-plasma source for EUV lithography,” *Proc. SPIE - Int. Soc. Opt. Eng.*, vol. 4688, pp. 102–109, 2002.

[55] S. N. Srivastava *et al.*, “Lifetime measurements on collector optics from Xe and Sn extreme ultraviolet sources,” *J. Appl. Phys.*, vol. 102, no. 2, 2007.

[56] T. Tomie, “Tin laser-produced plasma as the light source for extreme ultraviolet lithography high-volume manufacturing: history, ideal plasma, present status, and prospects,” *J. Micro/Nanolithography, MEMS, MOEMS*, vol. 11, no. 2, pp. 021109-1, 2012.

[57] D. Campos, S. S. Harilal, and A. Hassanein, “The effect of laser wavelength on emission and particle dynamics of Sn plasma,” *J. Appl. Phys.*, vol. 108, no. 11, pp. 1–7, 2010.

[58] A. Roy, S. S. Harilal, M. P. Polek, S. M. Hassan, A. Endo, and A. Hassanein, “Influence of laser pulse duration on extreme ultraviolet and ion emission features from tin plasmas,” *Phys. Plasmas*, vol. 21, no. 3, pp. 1–7, 2014.

[59] H. Tanaka, A. Matsumoto, K. Akinaga, A. Takahashi, and T. Okada, “Comparative study on emission characteristics of extreme ultraviolet radiation from CO_2 and Nd:YAG laser-produced tin plasmas,” *Appl. Phys. Lett.*, vol. 87, no. 4, pp. 17–20, 2005.

[60] Y. Tao, S. S. Harilal, M. S. Tillack, K. L. Sequoia, B. O’Shay, and F. Najmabadi, “Effect of focal spot size on in-band 13.5 nm extreme ultraviolet emission from laser-produced Sn plasma.,” *Opt. Lett.*, vol. 31, no. 16, pp. 2492–2494, 2006.

[61] A. Hassanein, “Combined effects of prepulsing and target geometry on efficient extreme ultraviolet production from laser produced plasma experiments and modeling,” *J. Micro/Nanolithography, MEMS, MOEMS*, vol. 10, no. 3, p. 033002, 2011.

[62] T. Sizyuk and A. Hassanein, “Optimizing laser produced plasmas for efficient extreme ultraviolet and soft X-ray light sources,” *Phys. Plasmas*, vol. 21, no. 8, 2014.

[63] Y. Ueno, G. Soumagne, A. Sumitani, A. Endo, and T. Higashiguchi, “Enhancement of extreme ultraviolet emission from a CO_2 laser-produced Sn plasma using a cavity target,” *Appl. Phys. Lett.*, vol. 91, p. 231501, 2007.

[64] S. S. Harilal, T. Sizyuk, V. Sizyuk, and A. Hassanein, “Efficient laser-produced plasma extreme ultraviolet sources using grooved Sn targets,” *Appl. Phys. Lett.*, vol. 96, no. 11, pp. 1–3, 2010.

[65] D. Nakamura *et al.*, “Diagnostics of ablation dynamics of tin micro-droplet for EUV lithography light source,” *Pacific Rim Conf. Lasers Electro-Optics, CLEO - Tech. Dig.*, pp. 6–7, 2009.

[66] C.-S. Koay *et al.*, “High conversion efficiency microscopic tin-doped droplet target laser-plasma source for EUVL,” vol. 5751, pp. 279–292, 2005.

[67] S. Fujioka *et al.*, “Pure-tin microdroplets irradiated with double laser pulses for efficient and minimum- mass extreme-ultraviolet light source production,” *Appl. Phys. Lett. Appl. Phys. Lett.*, vol. 92, no. 107, pp. 241502–121103, 2008.

[68] J. R. Freeman, S. S. Harilal, A. Hassanein, and B. Rice, “Effect of prepulse laser wavelength on EUV emission from CO_2 reheated laser-produced Sn plasma,” *Appl. Phys. A Mater. Sci. Process.*, vol. 110, no. 4, pp. 853–856, 2013.

[69] B. Martínez and F. Blanco, “Experimental and theoretical Stark width and shift parameters of neutral and singly ionized tin lines,” *J. Phys. B At. Mol. Opt. Phys.*, vol. 32, pp. 241–247, 1999.

[70] V. Sizyuk, A. Hassanein, V. Morozov, V. Tolkach, T. Sizyuk, and B. Rice, “Numerical Simulation of Laser-Produced Plasma Devices for Euv Lithography using the Heights Integrated Model,” *Numer. Heat Transf. Part A*, vol. 49, pp. 215–236, 2006.

[71] T. Sizyuk, J. Oliver, and P. K. Diwakar, “Mechanisms of carbon dimer formation in colliding laser-produced carbon plasmas,” *J. Appl. Phys.*, vol. 122, p. 023303, 2017.

[72] V. Banine and R. Moors, “Plasma sources for EUV lithography exposure tools,” *J. Phys. D. Appl. Phys.*, vol. 37, no. 23, pp. 3207–3212, 2004.

[73] M. Purvis *et al.*, “Industrialization of a robust EUV source for high-volume manufacturing and power scaling beyond 250W,” *Proc. SPIE*, vol. 10583, p. 1058327, 2018.

[74] M. Shigeta and A. B. Murphy, “Thermal plasmas for nanofabrication,” *J. Phys. D. Appl. Phys.*, vol. 44, no. 17, 2011.

[75] E. T. Thostenson, Z. Ren, and T.-W. Chou, “Advances in the science and technology of carbon nanotubes and their composites: a review,” *Compos. Sci. Technol.*, vol. 61, no. 13, pp. 1899–1912, 2001.

[76] A. R. Raffray *et al.*, “Design and material issues for high performance SiCf/SiC-based fusion power cores,” *Fusion Eng. Des.*, vol. 55, no. 1, pp. 55–95, 2001.

[77] C. R. Eddy and D. K. Gaskill, “Silicon carbide as a platform for power electronics,” *Science (80-.).*, vol. 324, pp. 1398–1400, 2009.

[78] J. Fan, H. Li, J. Jiang, L. K. Y. So, Y. W. Lam, and P. K. Chu, “3C-SiC nanocrystals as fluorescent biological labels,” *Small*, vol. 4, no. 8, pp. 1058–1062, 2008.

[79] A. M. Rossi, T. E. Murphy, and V. Reipa, “Ultraviolet photoluminescence from 6H silicon carbide nanoparticles,” *Appl. Phys. Lett.*, vol. 92, no. 25, 2008.

[80] S. Askari *et al.*, “Ultra-small photoluminescent silicon-carbide nanocrystals by atmospheric-pressure plasmas,” *Nanoscale*, vol. 8, no. 39, pp. 17141–17149, 2016.

[81] Q. Lu, S. S. Mao, X. Mao, and R. E. Russo, “Theory analysis of wavelength dependence of laser-induced phase explosion of silicon,” *Cit. J. Appl. Phys.*, vol. 104, p. 83301, 2008.

[82] J. Hoffman et al., “The effect of laser wavelength on the ablation rate of carbon,” Appl. Phys. A Mater. Sci. Process., vol. 117, pp. 395–400, 2014.

[83] W. R. Meier, A. M. Dunne, K. J. Kramer, S. Reyes, and T. M. Anklam, “Fusion technology aspects of laser inertial fusion energy (LIFE),” *Fusion Eng. Des.*, vol. 89, pp. 2489–2492, 2014.

VITA

John P. Oliver
School of Nuclear Engineering, Purdue University

EDUCATION

Purdue University, West Lafayette, IN

Ph.D., Nuclear Engineering	December 2018	GPA: 3.73/4.00
M.S., Nuclear Engineering	May 2018	GPA: 3.73/4.00

Texas A&M University, College Station, TX

B.S., Nuclear Engineering	December 2014	GPA: 3.51/4.00

Minor:
Mathematics, History
Hollingsworth Leadership Development Program – Leadership Certificate

RESEARCH EXPERIENCE

Graduate Research Assistant
Center for Materials Under eXtreme Environment (CMUXE)
School of Nuclear Engineering, Purdue University

Undergraduate Researcher
Nuclear Science Center
Department of Nuclear Engineering, Texas A&M University

AWARDS

Purdue University School of Nuclear Engineering Ross Fellowship
August 2017 – July 2018

Texas A&M Dwight Look College of Engineering Distinguished Student Award
May 2013

SciX 2016 Conference Mienhard Poster Award
September 2016

LEARDERSHIP EXPERIENCE

Treasurer, Society for Applied Spectroscopy	January 2017 – May 2018
President, Alpha Nu Sigma	August 2012 – May 2014
Corps of Cadets, Texas A&M University	
Platoon Leader, Scholastic Officer	August 2013 – May 2014
Scholastic Sergeant	August 2012 – May 2013
Cadet Corporal	August 2011 – May 2012

PUBLICATIONS

Journal Articles (Peer Reviewed)

1. **J.P. Oliver** and T.S. Sizyuk, "Stagnation Layer Development from Two Colliding Sn Plasmas for an Efficient EUV Source." *Physics of Plasmas*, (under review).

2. **J.P. Oliver**, N. Bharadwaj, and T.S. Sizyuk, "Laser-induced fluorescence of C2 and C3 in colliding carbon plasma." *Journal of Applied Physics*, (under review).

3. T.S. Sizyuk, **J.P. Oliver**, and P.K. Diwakar, "Mechanisms of carbon dimer formation in colliding laser-produced carbon plasmas." Journal of Applied Physics 122, (2017) 023303.

Conference Proceedings (Peer-Reviewed)

1. T.S. Sizyuk, **J.P. Oliver**, and W. Yuan, "Effects of chamber conditions on EUV source efficiency and optical system performance during high-frequency operation." Proceedings of SPIE, 10583 (2018) 105831D.

Conference Presentations

1. **J.P. Oliver**, T.S. Sizyuk, and P.K. Diwakar, "Laser-induced fluorescence of carbonaceous species in the colliding plasma regime." *SciX 2017*, Reno, NV, October 2017.

2. **J.P. Oliver**, T.S. Sizyuk, P.K. Diwakar, and A. Hassanein, "Plume propagation and emission dynamics of colliding carbon plasma." *SciX 2016*, Minneapolis, MN September 2016.

3. **J.P. Oliver**, A. Mohanta, T.S. Sizyuk, M.P. Polek, P.K. Diwakar, and A. Hassanein, "EUV emission characteristics of Nd:YAG prepulse and CO2 laser reheat for nanolithography devices." *International Conference on Laser Ablation*, Cairns, Australia, September, 2015.